Scuola di Dottorato di Scienze
Corso di Dottorato di Ricerca in Fisica e Astronomia
XVIII Ciclo, A.A. 2002–2005
Università Degli Studi di Milano Bicocca

Paolo Gorla

A Thesis submitted for the degree of
Dottore di Ricerca in Fisica

Optimization of the CUORE detector performance

Advisor
(Dr. O. Cremonesi)

Coordinator
(Prof. C. Destri)

To Marta

Contents

List of Figures

List of Tables

Introduction

In the last few years very important results have been reached in the study of neutrino and of its proprieties. The discovery of oscillations and of the non zero neutrino mass show finally a reasonably complete picture of this elusive particle. Nevertheless, while precision measurements on the oscillation parameters are planned for the near future, there are still two important missing pieces in the neutrino puzzle: the understanding of its nature (Dirac or Majorana) and the measurement of the absolute mass scale.

Neutrinoless Double Beta Decay (0νDBD) is a unique tool to discriminate the neutrino nature and eventually to measure its absolute mass. Many different experiments have been proposed and realized in these years to measure the 0νDBD looking towards the Quasi Degenerate neutrino mass region. A second generation of detectors is now rising up with the claim to look inside the Inverted Hierarchy mass region. The bolometric TeO_2 detectors for the search of the 0νDBD of ^{130}Te , play a leading role in this new generation of detectors.

This Ph.D. work had been performed in the framework of the CUORE (Cryogenic Underground Observatory for Rare Events) experiment, a TeO_2 array of 988 bolometric detectors, which aims to reach a sensitivity on the neutrino mass better than 50 meV. My research regarded mainly the R&D activity on the detectors performance and on background reduction. This work was performed in collaboration with Universidad de Zaragoza (Spain), while the experimental tests were performed in Laboratoi Nazionali del Gran Sasso (LNGS) of INFN.

My activity was focused on three fundamental R&D topics: the increase of the absorber mass of the bolometer, the reduction of the background and the improvement of the performance (resolution and reproducibility). Most of the knowledge necessary to carry on this activity came from the experience gained with the CUORICINO experiment, a prototype of CUORE, built with 62 TeO_2 bolometers. CUORICINO is the most sensitive 0νDBD experiment presently running and is located in the LNGS underground site. All this three activities are mainly related to the possibility of increasing the sensitivity to the Majorana mass.

The challenge to increase the absorber mass is originated by the necessity of increasing the number of active nuclei under control and reducing as much as possible the number of detectors in order to reduce the technical problems of handling a big number of channels. This activity lead to a cold test with two detectors $6\times6\times6$ cm^3 of about 1.3 kg each. This detectors, the most massive bolometers ever built, showed a very good performance but came out to be too fragile for a large scale application.

The background reduction is the most important development in view of CUORE. Background is in fact the only parameter that can be tuned by orders of magnitude thus allowing a sizeable improvement of the experimental sensitivity. The CUORE background reduction program foresees a reduction from the present CUORICINO level of 0.18 counts/keV/kg/y to about 0.01 counts/keV/kg/y. The project and realization of two cold tests of 8 detectors each was an

important part of this work. The first test was devoted to a reduction of the surface radioactive contaminations of the detector main components: copper holder and TeO_2 crystals. This contaminations, due to the degraded alpha particle contributions, are believed to be at the origin of the continuous background in the 0νDBD region. The results of this test showed a reduction by a factor 4 for the crystal surface contribution, reaching the CUORE milestone for this material. Unfortunately only a less relevant improvement was obtained for the copper. The second test was performed to exclude radioactive contributions from sources different from copper and TeO_2 : PTFE, gold and Si. All these materials were excluded as possible background sources.

Finally I designed a new detector holder and setup to improve the detector resolution. This setup was tested with a 12 detector array showing a higher uniformity of resolution with respect to CUORICINO, reducing the deviation from the mean resolution from 40% to 14%.

Chapter 1

Neutrinoless double beta decay

In 1930 W.Pauli postulated the existence of the neutrino in order to reconcile the data on the radioactive decay of nuclei with energy conservation. Since in those years many experiments have been performed, big improvements have been made in the comprehension of neutrinos and their strange behavior. In 1934, E. Fermi published the first theory on beta decay; further progress was made in the '50s, thanks to Lee and Yang's hypothesis on the P–parity violation, experimentally proved in 1956 by Wu. In 1959 F. Reines and C. Cowan performed the first direct observation of the electron antineutrino corrfrom a nuclear reactor. In 1962 muon neutrinos were discovered by L. Lederman, M. Schwartz, J. Steinberger and colleagues at the Brookhaven National Laboratories and it was confirmed that they are different from electron neutrinos.

In the 60's the interest on neutrino was renewed by the possibility of using this particle to study astrophysical sources. In those years, neutrinos produced in the sun and in the atmosphere were observed. In 1987, neutrinos from a supernova in the Large Magellanic Cloud were also detected.

The unexpected behavior of the neutrinos from the sun (discrepancy between the measured flux and the expected one) turned again the interest of the Scientific Community at the fundamental proprieties of this particle. The mass of the neutrino has become a crucial topic in particle physic.

In the last years, Neutrinoless Double Beta Decay (0νDBD) came out to be a crucial phenomenon in understanding the nature of neutrino and for measuring the absolute mass scale of neutrinos.

In this chapter a brief introduction to neutrino mass theory, from the Standard Model (SM) to neutrino oscillation is reported. The importance of 0νDBD and the present experimental scenario are overviewed.

1.1 The role of neutrino mass in particle physics and cosmology

The Standard Model (SM) of electroweak interactions describes neutrinos as left-handed massless partners of the charged leptons. The experimental identification of the third generation of quarks and leptons completed the model, incorporating also a description of CP violation. The invisible width of the Z boson, caused by its decay into unobservable channels and measured in the e^+-e^- annihilation experiments, showed clearly that there are just three active neutrinos with masses of less than $M_Z/2$.

author	WMAP	CMB$_{hi-l}$	SDSS	2dF	other data	$\sum m_\nu$ [eV]
Bar'03	x	x	x	x	h(HST)	< 0.75
Teg'03	x	x	x		SNIa	< 1.7
ASB'03	x	x		x	XLF	$= 0.36 - 1.03$
WMAP	x	x		x	Lyα, h(HST)	< 0.7
Bla'03	x			x	$\Omega_m = 1$	$= 2.4$
Han'03	x	x		x	h(HST) , SNIa	< 1.01
Han'03	x	x		x		< 1.2
Han'03	x			x		< 2.12

Table 1.1: Cosmological determination of the neutrino mass according to different authors and on the basis of different data set and assumptions. The systematic spread in the limits/values is apparent.

Efforts to unify the strong and electroweak interactions led to the development of Grand Unified Theories (GUTs), which provide a natural framework for determining neutrino masses. In the context of GUTs it is possible to develop predictive models for the fermion masses in general and for the neutrino masses in particular. The smallness of the neutrino masses is explained by means of the seesaw mechanism, which is often incorporated in GUTs in various forms. In this context, neutrino is naturally a Majorana particle. Therefore, the experimental determinations of the neutrino mass scale, pattern and nature are crucial bench tests for predictive GUTs and for the improvement of our understanding of the basic theory of fundamental interactions.

In parallel, the understanding of Big-Bang Nucleosynthesis and the features of the Cosmic Microwave Background (CMB) illustrate the important role of neutrinos in the history of the early universe. Neutrino flavor oscillations and other bounds tell us that the heaviest neutrino mass is in the range 0.04 - 0.6 eV. Therefore, neutrinos are a component of dark matter, but their total mass, although it outweighs the stars, gives only a minor contribution to invisible matter density. Neutrinos are so light and they had streamed freely away from developing aggregations of matter until quite recently (in cosmological terms), when they eventually cooled and their speed has decreased to significantly less than the speed of light. What is then the neutrino role in shaping the universe? Do neutrinos allow to understand the matter-antimatter asymmetry of the universe, via leptogenesis? The answer to these questions requires the precise knowledge of the neutrino mass values.

It is clear, therefore, that the neutrino mass scale is crucial over two fronts: progress in the comprehension of elementary particles and solution of hot astroparticle problems. The studies of neutrinoless double beta (0ν-$\beta\beta$) decay are essential and unique in their potential to fix the neutrino masses and to answer key-questions beyond neutrino physics itself.

1.1.1 Dirac neutrinos and Majorana neutrinos

The distinction between particle and antiparticle is related to the presence of a conserved quantity (charge). This happens for all charged particles, were the antiparticles have opposite electric charge. But any other charge can distinguish particles from antiparticles in the same way (e.g., neutron or the Λ° differ from their antiparticles since they have opposite baryon number). The

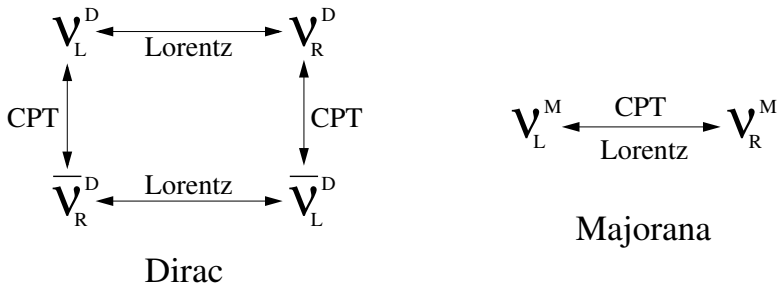

Figure 1.1: Transformations among neutrinos: Dirac neutrinos (left); Majorana neutrinos (right).

possibility that a particle do not differ from its antiparticle was first suggested by Majorana in 1937 [4]. The neutrinos came out to be the best candidate to be a Majorana particle.

In the framework of the Standard Model, massive Dirac neutrinos consist of four different states, assuming a neutrino with negative helicity (left handed) ν_L; if CPT theorem holds, then there will be the corresponding CPT-transformed state, i.e. an antineutrino with positive helicity (right handed), $\bar{\nu}_R$. If the neutrino has a mass then will exist a Lorentz boost that permits the helicity flip. Thus if the neutrino has a charge (lepton number) and a mass, it consists of four different states called a Dirac neutrino. If, on the contrary, the neutrino do not have a charge, only the two helicity states are defined; this is called a Majorana neutrino (see fig. 1.1). Due to the V–A structure of the Standard Model the right handed neutrinos are sterile. Thus only two neutrinos are able to interact, as in the Majorana case. The difference is that in the Standard Model their interaction follows from their charge conservation while in the Majorana case the interaction is governed by the helicity.

From a theoretical point of view, the possibility that neutrinos are Majorana particles is particularly appealing. The fact that the neutrinos and charged leptons, belonging to the same weak doublet, have an extremely different mass (at least a factor 10^5) cannot be explained in the Dirac theory. Such an "anomaly" can, on the contrary, be explained in a "natural" way (without adding any exotic symmetry or propriety) through the "see-saw" mechanism [5]: in the Majorana case, the mass of the neutrino naturally satisfies the relation

$$M_\nu \, M \approx \; M_{q,\ell}^2,$$

where $M_{q,\ell}$ represent the mass of a lepton or a quark, and M represents a mass scale.

Due to their tiny mass, the Dirac neutrinos are practically produced in nature, always left-handed, while anti-neutrinos are right handed. It is therefore impossible to discriminate whether they interact due to the lepton charge or due to their helicity. Different characteristics arise from the CPT transformation rules: it can be demonstrated [6] that if CPT is a conserved symmetry, then the Majorana neutrino cannot have an electric dipole or magnetic dipole moment. The magnetic moment of a Dirac neutrino can be evaluated [7] as $3.2 \cdot 10^{-19} \; m_\nu \; \mu_B$ (μ_B is the Bohr magneton and m_ν is expressed in eV). The present experimental limits are at least six orders of magnitude far away from the predicted value. There are other possibilities in order to search for lepton number non-conservation as in the case of pions and mesons decays [8]; the expected sensitivity, however, is very small compared to double beta decay. Thus the most favorable way

to discriminate between Dirac and Majorana neutrino turns out to be the neutrinoless double beta decay (0νDBD).

After the discovery of neutrino oscillation, implying neutrino masses, the introduction of a mixing matrix between flavor eigenstates and mass eigenstates is straightforward.

Neutrino oscillations can take place since the neutrinos of definite flavor (ν_e, ν_μ, ν_τ) are not necessarily states of a definite mass (ν_1, ν_2, ν_3). On the contrary, they are generally coherent superpositions of such states:

$$|\nu_l\rangle = \sum_i U_{li}|\nu_i\rangle \tag{1.1}$$

When the standard model is extended to include neutrino mass, the mixing matrix U is unitary. As a consequence the neutrino flavor is no longer a conserved quantity and for neutrinos propagating in vacuum the amplitude of the process $\nu_l \rightarrow \nu_{l'}$ is not vanishing.

The probability of the flavor change is the square of this amplitude. Due to the unitarity of U there is no flavor change if all masses vanish or are exactly degenerate. The idea of oscillations was discussed earlier on by Pontecorvo, and by Maki, Nakagawa and Sakata [9, 10, 11]. Hence, the mixing matrix U, analogous of the CKM matrix of the quark sector, is often associated with these names and the notation U_{PMNS} is used. The flavor eigenstates can then be written as $\nu_\alpha = \sum_i U_{\alpha i}\nu_i$. $U_{\alpha i}$ are the elements of the U_{PMNS} matrix, and are related to the observable mixing angles in the base where the charged lepton masses are diagonal. For Majorana neutrinos there is an additional matrix that takes into account the fact that in this case there are 2 more complex phases. Using the Chau and Keung [12] parameterization of the PMNS matrix, we have:

$$\begin{pmatrix} \nu_e \\ \nu_\mu \\ \nu_\tau \end{pmatrix} = UV \begin{pmatrix} \nu_1 \\ \nu_2 \\ \nu_3 \end{pmatrix} = \\ \begin{pmatrix} c_{12}c_{13} & s_{12}c_{13} & s_{13}e^{-i\delta} \\ -s_{12}c_{23} - c_{12}s_{23}s_{13}e^{i\delta} & c_{12}c_{23} - s_{12}s_{23}s_{13}e^{i\delta} & s_{23}c_{13} \\ s_{12}s_{23} - c_{12}c_{23}s_{13}e^{i\delta} & -c_{12}s_{23} - s_{12}c_{23}s_{13}e^{i\delta} & c_{23}c_{13} \end{pmatrix} \times \\ \times \begin{pmatrix} 1 & 0 & 0 \\ 0 & e^{i\phi_2/2} & 0 \\ 0 & 0 & e^{i(\phi_3/2+\delta)} \end{pmatrix} \begin{pmatrix} \nu_1 \\ \nu_2 \\ \nu_3 \end{pmatrix} \tag{1.2}$$

where $c_{ij} \equiv \cos\theta_{ij}$ and $s_{ij} \equiv \sin\theta_{ij}$; θ_{ij} are the mixing angles measured with the neutrino oscillations; δ is the Dirac CP phase. V is a diagonal matrix containing the Majorana CP phases (ϕ_2 end ϕ_3) that do not exist in the case of Dirac neutrinos and that, in any case, cancel in neutrino oscillations.

1.2 Double Beta Decay

The two-neutrino double beta decay mode (2νDBD) is expected to occur in the Standard Model as a second order effect of the well known beta decay Hamiltonian [13], and it imposes no special requirements on the properties of the neutrino. It will occur irrespective of whether the

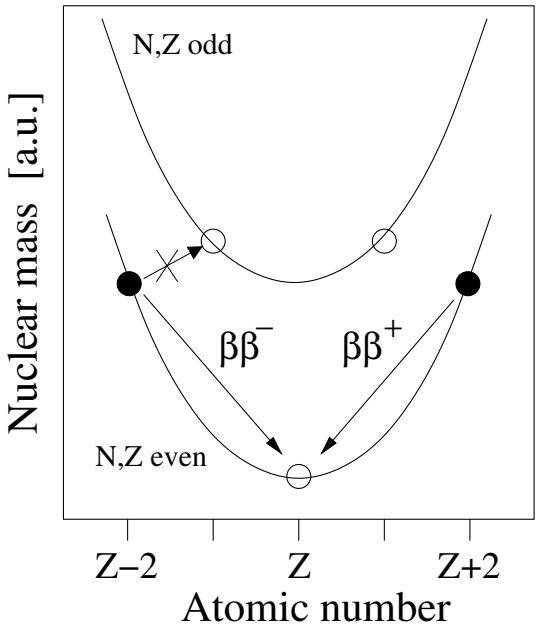

Figure 1.2: Schematic picture of the atomic mass as a function of Z for isobar multiplets with even A.

neutrino is a Majorana or a Dirac particle and irrespective of whether it has a mass or not. The possible 2ν decay modes are:

$$\begin{array}{ll} \text{(A, Z)}\rightarrow (A,\ Z+2) + 2e + 2\bar{\nu}_e & \beta\beta^- \\ \text{(A, Z)}\rightarrow (A,\ Z-2) + 2e^+ + 2\nu_e & \beta\beta^+ \\ \text{(A, Z)}+2e^- \rightarrow (A,\ Z-2) + 2\nu_e & ECEC \\ \text{(A, Z)}+e^- \rightarrow (A,\ Z-2) + e^+ + 2\nu_e & EC\beta^+ \end{array} \tag{1.3}$$

Nuclear transitions accompanied by positron emission or electron capture processes are, however, characterized by poorer experimental sensitivities and will not be discussed in the following. The first process of Eq. 1.3 represents the analogue of the single beta decay mediated by the weak current in which a *d* quark transforms into an *u* with the emission of an e^- and an $\bar{\nu}$; even if mediated by the same weak interaction, DBD is a second order transition, resulting in an extremely slow decay rate, namely the slowest process ever observed in nature. Using simple dimensional arguments it is straightforward to demonstrate that, as a first approximation, the 2νDBD is $\sim 10^{21}$ times slower with respect to the single beta decay, resulting in half lives of the order of 10^{18} – 10^{22} years. The experimental observation of 2νDBD is therefore possible only if the single beta decay is forbidden by energy conservation or, at least, strongly hindered by small transition energy and/or by large change of angular momentum.

This happens with several nuclei in nature and is due to the "pairing" interaction [14] (see fig. 1.2). The first "direct" observation of the 2νDBD was obtained in 1987 [15] and is now observed in more than ten nuclei [16, 17].

More interesting is the *neutrinoless* double beta decay (0νDBD), first proposed by Furry [18] in 1939. In this case there is the maximum lepton number violation (ΔL=2) and the decay is,

therefore, not allowed by the Standard Model. The 0νDBD can occur only if two requirements are satisfied:

- the neutrino has to be a Majorana particle,
- the neutrino has to have a mass and/or the neutral current has to have a right handed (V+A) component.

The second condition is needed because of the helicity of the neutrino. Due to the V-A nature of the weak interaction, the neutrino emitted in the first vertex (see fig. 1.3) is right handed, while in order to be absorbed in the second one, it needs to change its helicity. Thanks to the finite mass this is possible, with a probability $\propto m_\nu/E_\nu$; from here it turns out that the amplitude of the decay is proportional to m_ν. Disregarding more unconventional contributions (SUSY or left-right symmetric models), the 0νDBD rate is usually expressed as:

$$[T^{0\nu}_{1/2}]^{-1} = G^{0\nu}|M^{0\nu}|^2\frac{|\langle m_\nu\rangle|^2}{m_e^2} \tag{1.4}$$

where $G^{0\nu}$ is the (exactly calculable) phase space integral $\propto Q^5_{\beta\beta}$ ($Q_{\beta\beta}$ represents the Q-value of the decay), $|M^{0\nu}|^2$ is the specific nuclear matrix element of the nucleus undergoing the decay and $|\langle m_\nu\rangle|$ (effective electron neutrino mass, often called $|m_{ee}|$) is the neutrino relevant parameter measured in 0νDBD. In this situation, one possibility is to consider the spread of the theoretical values of the nuclear matrix elements as a measure of their uncertainty. In tab. 1.2.1 a list of values of $F_N = G^{0\nu}\left|M^{0\nu}\right|^2$ calculated in the framework of different nuclear models are summarized. By using Eq. (1.2) we have:

$$|\langle m_\nu\rangle| \equiv |\ |U_{11}|^2 m_1 + |U_{12}|^2 m_2 e^{i\phi_2} + |U_{13}|^2 m_3 e^{i\phi_3}\ | \tag{1.5}$$

where $e^{i\phi_2}$ and $e^{i\phi_3}$ are the Majorana CP phases (=$\pm$1 in case of CP conservation), $m_{1,2,3}$ the mass eigenvalues and U_{1j} the matrix elements of the PMNS matrix. The presence of the ϕ_k phases implies that cancellations are, unfortunately, possible. Such cancellations are complete for a Dirac neutrino, since it is equivalent to two degenerate Majorana neutrinos with opposite CP phases. This stresses once more the fact that 0νDBD can occur only through the exchange of Majorana neutrinos.

From a Particle Physics point of view, 0νDBD represents a unique tool in order to measure the neutrino Majorana phases and to assess the absolute scale of the neutrino masses. As in evidence from Eq. (1.4), the derivation of the crucial parameter $\langle m_\nu\rangle$ from the experimental results on 0νDBD lifetime requires a precise knowledge of the Nuclear Matrix Elements (NME) of the transition. Unfortunately, this is not an easy job, and a definite knowledge of NME values and uncertainties is still lacking in spite of the large attention attracted by this area of research. Many, often conflicting, evaluations are available in the literature and it is unfortunately not easy to judge their correctness or accuracy. Outstanding progress has been achieved over the last few years mainly due to the application of the QRPA method and its extensions. Renewed interest in Shell Model calculations has been boosted, on the other hand, by the fast development of computer technologies. Comparison with experimental 2νDBD rates has often been suggested as a possible way out (direct test of the calculation method). The evaluation methods for the two decay modes show, however, relevant differences (e.g. the neutrino propagator), and

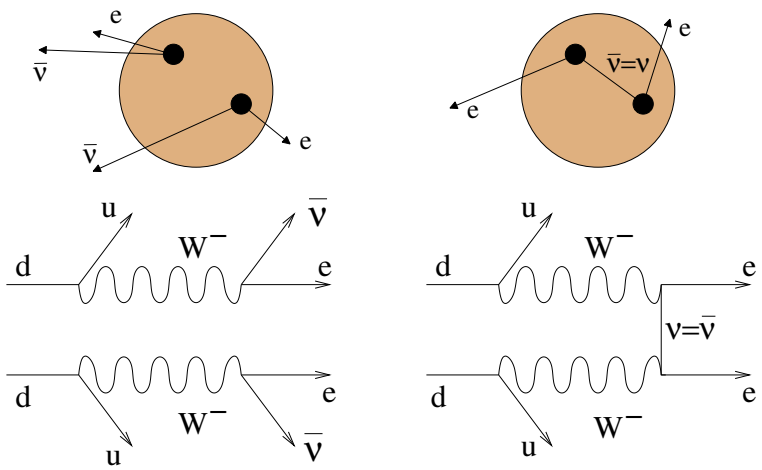

Figure 1.3: Elementary scheme for 2νDBD (left) and 0νDBD (right).

the effectiveness of such a comparison is still controversial [2, 19, 20]. A popular but doubtful attitude consists in considering the spread of the different evaluations as an estimate of their uncertainties. In such a way one obtains a spread of about one order of magnitude in the expected half-lives (Table 1.2), corresponding to a factor of ~ 3 in $\langle m_\nu \rangle$. It is clear that a big improvement in the calculation of NME or, at least, in the estimate of their uncertainties would be welcomed. New calculation methods should be pursued while insisting on the comparison with dedicated measurements coming from various areas of Nuclear Physics [21]. On the other hand, an experimental effort to investigate as many $\beta\beta$ emitters as possible should be addressed.

Isotope	[22]	[23]	[24]	[2]	[25]	[26]
^{48}Ca	8.83	-	-	-	2.5	-
^{76}Ge	17.7	14.0	2.33	6.0	3.6	3.7
^{82}Se	2.4	5.6	0.6	1.8	1.5	0.81
^{100}Mo	-	1.0	1.28	3.5	3.9	0.65
^{116}Cd	-	-	0.48	2.4	4.7	0.39
^{130}Te	5.8	0.7	0.5	3.0	0.85	0.52
^{136}Xe	12.1	3.3	2.2	7.3	1.8	0.27
^{150}Nd	-	-	0.025	> 0.3	-	-

Table 1.2: Theoretically evaluated 0νDBD half-lives (units of 10^{28} years) for $|\langle m_\nu \rangle|$ = 10 meV. Only a few references are shown. The results of [2] are still considered by the authors as preliminary.

1.2.1 Prediction on the Majorana mass

The input parameters in order to figure out the possible mass pattern of the Majorana neutrinos are given by the neutrino oscillations. The most updated values [27, 28, 29, 30, 31, 32] are given

in Table 1.3.

Oscillation parameter	central value	99% CL range
Solar mass splitting	Δm^2_{12} = (8.0± 0.3) $10^{-5} eV^2$	(7.2–8.9) $10^{-5} eV^2$
Atmospheric mass splitting	$\lvert\Delta m^2_{23}\rvert$ = (2.5± 0.3) $10^{-3}\mathrm{eV}^2$	(1.7–3.3) $10^{-3}\mathrm{eV}^2$
Solar mixing angle	$\tan^2\theta_{12}$ = 0.45± 0.05	$30^\circ < \theta_{12} < 38^\circ$
atmospheric mixing angle	$\sin^2 2\theta_{23}$ = 1.02± 0.04	$36^\circ < \theta_{23} < 54^\circ$
'CHOOZ' mixing angle	$\sin^2 2\theta_{13}$ = 0±0.05	$\theta_{13} < 10^\circ$

Table 1.3: Summary of the present information on neutrino masses and mixings from oscillation data. For a recent review see [1].

Given the two Δm^2 measured with the oscillations, and given the assumption of three neutrinos, the absolute mass scale is still missing. Nevertheless, three scenarios are possible, as shown in fig. 1.4. The previously quoted values can be accommodated in the framework of three neutrinos mixing, which describes the three flavour neutrinos (ν_e, ν_μ and ν_τ) as unitary linear combinations of the three massive neutrinos (ν_1, ν_2 and ν_3) having masses m_1, m_2, and m_3, respectively. The experimental measurements are compatible with three mass schemes:

1. Normal hierarchy: $m_1 < m_2 < m_3$, i.e. $\Delta m^2_{23} > 0$

$$\Delta m^2_{12} \simeq \Delta m^2_{\mathrm{sun}} \simeq m_2^2 \quad \Delta m^2_{23} \simeq |\Delta m^2_{\mathrm{atm}}| \simeq m_3^2 \tag{1.6}$$

2. Inverted hierarchy: $m_3 < m_1 < m_2$, i.e. $\Delta m^2_{23} < 0$

$$\Delta m^2_{12} \simeq \Delta m^2_{\mathrm{sun}} \quad \Delta m^2_{23} \simeq -|\Delta m^2_{\mathrm{atm}}| \simeq -\, m_1^2 \tag{1.7}$$

3. Degenerate case: the values of $\Delta\, m^2_{ij}$ are small when compared to each mass values. In this case the hierarchies are undistinguishable:

$$|\Delta m^2_{ij}| \ll m_1^2 \simeq m_2^2 \simeq m_3^2 \tag{1.8}$$

In order to extract the correct prediction, however, one has to use Eq. (1.5); the steps are:

- use the matrix elements given by Eq. (1.2) with the evaluated neutrino parameter from Table 1.3,
- parameterize $m_2 = \sqrt{m_1^2 + \Delta m^2_{sun}}$ and $m_3 = \sqrt{m_2^2 + |\Delta m^2_{atm}|}$ for normal hierarchy,
- parametrize $m_1 = \sqrt{m_3^2 + |\Delta m^2_{atm}|}$ and $m_2 = \sqrt{m_1^2 + \Delta m^2_{sun}}$ for inverted hierarchy.

With this procedure the effective Majorana mass can be written as a function of the lightest neutrino mass ($\mathrm{m}_{light} \equiv m_1$ for normal hierarchy, $\mathrm{m}_{light} \equiv m_3$ for inverted hierarchy):

$$|\langle m_\nu \rangle| \equiv |m_{ee}| = f(m_{light}, \phi_1, \phi_2, observables) \tag{1.9}$$

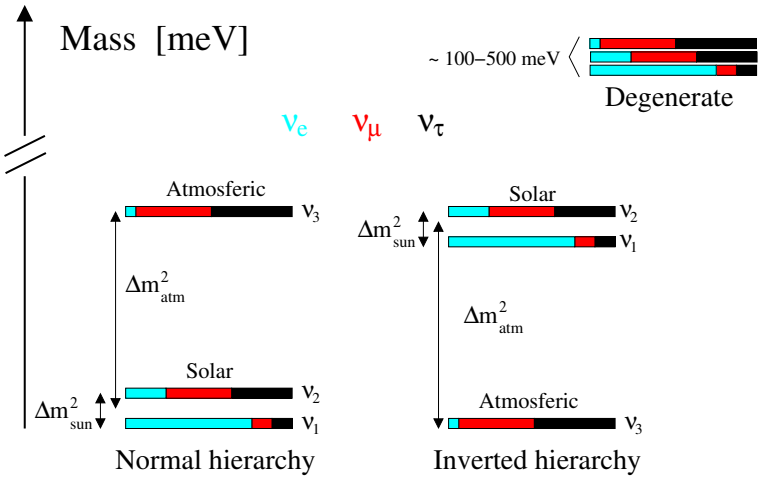

Figure 1.4: Neutrino mass pattern based on the experimental relation $\Delta m^2_{\rm sun} \ll \Delta m^2_{\rm atm}$.

where *observables* are all the experimental data from neutrino oscillations. The plot of $|\langle m_\nu \rangle| \equiv |m_{ee}|$ is shown in fig. 1.5. The two disfavoured regions are given by the present limits on DBD experiments (see Table 1.5) and by cosmological (Large Scale Structures and anisotropies in the Cosmic Microwave Background) bounds [33, 34, 35].

The DBD-Experiments developed up to now, often called *First Generation Experiments*, were designed to explore only the degenerate mass scenario. The proposed *Second Generation Experiments* are designed to explore the inverted hierarchy scenario, with an expected sensitivity on $|m_{ee}|$ of the order of 10–50 meV.

1.3 Experimental Techniques

The experimental signatures of the nuclear double beta decays are in principle very clear: in the case of the 0νDBD, one should expect a peak (at the $Q_{\beta\beta}$ value) in the two-electrons summed energy spectrum, whereas a continuous spectrum (with a well-defined shape) will feature the 2νDBD.

In spite of such characteristic imprints, the rarity of the processes under consideration makes their identification very difficult. Such remotely probable signals have to be disentangled from a background due to natural radioactive decay chains, cosmogenic-induced activity, and man-made radioactivity, which deposit energy in the same region as the DBD, but at a faster rate. Consequently, the *main task* in 0νDBD searches is to diminish the background by using the state-of-the-art ultra-low background techniques and, hopefully, identifying the signal. There are many experiments searching for DBD. They can be subdivided into three categories:

- geochemical determination of the total decay time through the measurement of the daughter nuclei $(A, Z+2)$ produced by the parent nuclei (A, Z) in a sample of "old" geological rocks.

- Radiochemical measurement of the total decay time by the extraction of the radioactive

	Authors/Ref.	Method	$T_{1/2}(^{130}Te)$ (10^{23} y)	$F_N(^{130}Te)$ (10^{-13} y^{-1})
QRPA	Staudt et al., 1992 [36]	pairing (Paris)	0.77-0.88	29-34
		pairing (Bonn)	0.9-1.1	24-29
	Pantis et al., 1996 [37]	no p-n pairing	8.64	3.0
		p-n pairing	21.1	1.24
	Vogel, 1986 [38]		6.6	3.96
	Civitarese, 1987 [39]		5.2	5.0
	Tomoda, 1991 [40]		5.2	5.03
	Barbero et al., 1999 [41]		3.36	7.77
	Simkovic, 1999 [42]	pn-RQRPA	14.5	1.79
	Suhonen et al., 1992 [43]		8.34	3.13
	Muto et al., 1989 [44]		4.89	5.34
	Stoica et al., 2001 [45]	large basis	10.7	2.44
		short basis	9.83	2.66
	Faessler et al., 1998 [46]		9.4	2.78
	Engel et al., 1989 [47]	generalized seniority	2.4	10.9
	Aunola et al., 1998 [48]	WS	4.56	5.72
		AWS	5.16	5.06
	Rodin et al., 2003 [49]		27.5	0.95
SM	Haxton et al., 1984 [50]	weak coupling	1.6	16.3
	Caurier et al., 1996 [51]	large basis	58	0.45
OEM	Hirsh et al., 1995 [52]		7.3	3.6

Table 1.4: 0νDBD nuclear factors of merit F_N for ^{130}Te according to different evaluation methods (QRPA: Quasi Random Phase Approximation, SM: Shell Model and OEM: Operator Expansion Method) and authors. The foreseen 0νDBD half-lifetime for ^{130}Te ($\mid m_\nu \mid$=1 eV) is also reported.

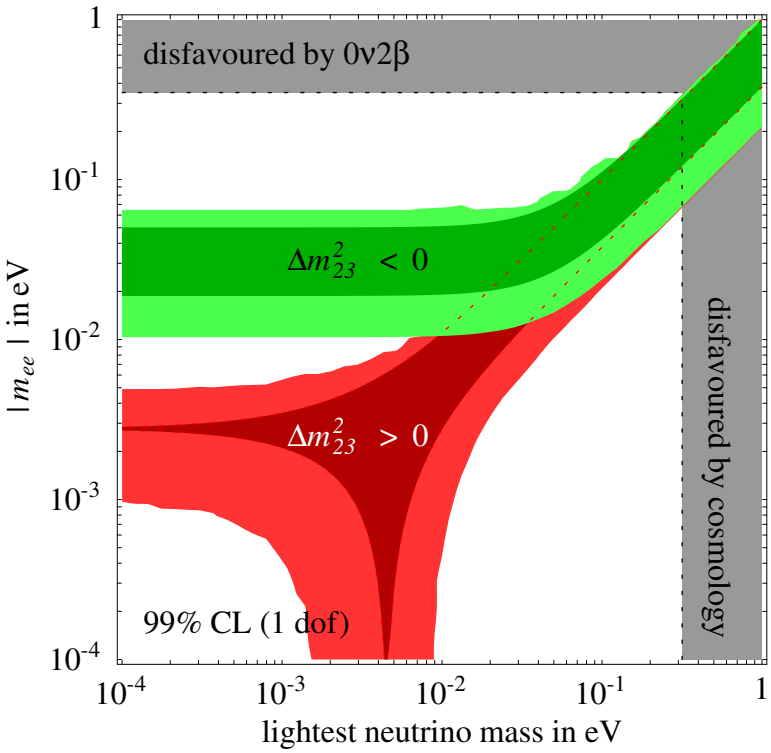

Figure 1.5: 99 % CL range for m_{ee} as function of the lightest neutrino mass. The darker regions show how the m_{ee} range would shrink if the the best-fit values of oscillation parameters were confirmed with negligible errors (in this case the spread is due only to the Majorana CP phases). Picture given by courtesy of the authors of [1].

daughter nuclei from the parent nuclei.

- Direct detection of the two electrons emitted in the transition.

The experiments belonging to the first two classes do not allow to distinguish among the two decay channels. They are, however, extremely sensitive to inclusive effects, since the so-called "accumulation times" for the daughter isotope are very long. They gave, however, the first *indirect* proof [53, 54] of the existence of the 2νDBD, but are no longer pursued nowadays. Direct experiments are the more interesting because they allow to distinguish the various modes of the double beta decay. It is therefore possible to search for the decay without neutrinos, which represents the most interesting process. The nuclear detector capable of revealing the two electrons emitted by the DBD-Emitter should have some basic properties:

- *high energy resolution*, since a peak must be identified over a background.
- *Low background*, which requires the use of extremely radiopure materials: natural radioactivity (mainly ^{232}Th and ^{238}U chains) exhibits decay times of the order of 10^9 years, extremely short if compared with the expected 0νDBD that should have a decay time

larger than 10^{25} years. Furthermore it is absolutely necessary to operate the detector in underground laboratories in order to shield cosmic rays.

- *Large source* of DBD nuclei in order to have sensitivity to the decay time up to 10^{25}–10^{28} years.
- *Event reconstruction methods*, since the 0νDBD has a very characteristic decay with the two electrons that share the $Q_{\beta\beta}$ energy. Electron tracking can therefore help in rejecting background.

Unfortunately there are up to now no detectors that can fulfill these four requirements at the same time. Two are, substantially, the experimental approaches:

- homogenous detectors (or active source detectors), whose mean feature is to have the active $\beta\beta$ source inside the detector material,
- non-homogeneous detectors (or passive source detectors), in which the source and the detector are distinct.

Various conventional counters have been used so far in DBD direct searches: solid state devices (Germanium spectrometers and Silicon detector stacks), gas counters (time projection chambers, ionization and multiwire drift chambers) and scintillators (crystal scintillators and stacks of plastic scintillators). Techniques based on the use of low temperature calorimeters have been, on the other hand, proposed and developed in order to improve the experimental sensitivity and enlarge the choice of suitable candidates for DBD searches, with an *active source* approach.

A common feature of all DBD experiments has been the constant work against backgrounds caused mainly by environmental radioactivity, cosmic radiation and residual radioactive contaminations of the detector setup elements. Further suppression of such backgrounds will be the *actual challenge* for future projects whose main goal will be to maximize the 0νDBD rate while minimizing background contributions.

In order to compare different experiments and in order to point out the advantages and the disadvantages of the two different detecting techniques, it is convenient to introduce a very important parameter, called "sensitivity", denoted by S. It is defined as the process' half-life corresponding to the maximum number of signals (n) that could be hidden by the background fluctuations, at a given statistical C.L. (see Chapter 6). Let t be the measurement time, $N_{\beta\beta}$ be the number of atom candidates for $\beta\beta$ decay present in the source, B (expressed in number of counts per unit energy per unit time) the background counting rate in the energy region where the decay peak is expected and ΔE the FWHM energy resolution. The expected number of background counts in an energy interval equal to the FWHM energy resolution centered at the transition energy can then be written as $N_B = B\Delta E t$. The sensitivity factor S at 1σ level ($n = \sqrt{N_B}$) is defined as:

$$S \equiv T_{1/2} = \frac{cost\ N_{\beta\beta}\ t}{n} = cost\ N_{\beta\beta}\sqrt{\frac{t}{B\Delta E}} \tag{1.10}$$

If the background (measured as counts per unit energy per unit mass per unit time) is proportional to the detector mass the above formula can be rewritten as

$$S = cost\frac{i.a.\epsilon x}{A}N_A\sqrt{\frac{Mt}{B\Delta E}} \quad (68\%\ C.L.) \tag{1.11}$$

where A is the compound molecular mass , x the number of $\beta\beta$ atoms per molecule, $i.a.$ their isotopic abundance, M the source mass, N_A the Avogadro's number and ϵ the efficiency of the detector. In addition to its simplicity, Eq. (1.11) has the advantage of emphasizing the role of the essential experimental parameters: mass, measuring time, isotopic abundance, background level, energy resolution and detection efficiency.

As far as the active source experiments are concerned, they can have detection efficiencies of the order of $\sim 90\%$, and energy resolution of the order of $\sim 0.2\%$ FWHM (for Ge diodes and bolometers), while the background (mainly arising from the surrounding setup) cannot be easily rejected. As far as the passive source experiments are concerned, they are mostly performed with gas detectors (TPC, DC) in which the source is introduced into the volume of the detector as very thin sheets (of about $50\mu m$), to reduce the energy loss of the electrons emitted in the decay. The detection efficiency associated with this kind of measure is of the order of 30%. The great advantage of these experiments lies in the reduction of the background: the clear trace, which is peculiar in a drift chamber, for a 2 electrons event, guarantees a very good capability of background discrimination. The energy resolution, on the other hand, cannot be as good as $\sim$ 7–10 % FWHM. As will be shown in Sec.(1.4) the energy resolution plays an extremely crucial role in the second generation experiments due to the fact that the 2νDBD close to the endpoint will result in an unavoidable/unrejectable source of background for the 0νDBD mode.

1.3.1 First Generation Experiments

Impressive progress has been obtained during the last years in improving 0νDBD half-life limits for several isotopes and in systematically updating the 2νDBD rates (Table 1.5). Although 2νDBD results are in some cases inconsistent, the effort to cover as many $\beta\beta$ nuclei as possible thus allowing a direct check for 2νDBD NME is evident. Optimal 0νDBD sensitivities have been reached in a series of experiments based on the active source approach. In particular, the best limit on 0νDBD comes from the Heidelberg-Moscow (HM) experiment [55] on ^{76}Ge even if similar results have been obtained also by the IGEX experiment [56] (Table 1.5).

In both cases a large mass (several kg) of isotopically enriched (86 %) Germanium diodes, is installed deep underground under heavy shields for gamma and neutron environmental radiation. Extremely low background levels are then achieved thanks to a careful selection of the setup materials and further improved by the use of pulse shape discrimination (PSD) techniques. Both experiments quote similar background levels in the 0νDBD region of ≈ 0.2 (c/keV $\cdot$ kg $\cdot$ y) and ≈ 0.06 (c/keV$\cdot$ kg$\cdot$ y) before and after PSD. Taking into account the uncertainties in the NME calculations, such experiments indicate a limit of 0.3 - 1 eV for $\langle m_\nu \rangle$.

As will be discussed later, new ideas to improve such a successful technique characterize many of the proposed future projects. However, given the NME calculation problem, more $\beta\beta$ emitters than allowed by the use of conventional detectors (e.g. ^{76}Ge, ^{136}Xe, ^{116}Cd) should be investigated using the calorimetric approach. A solution to this problem, suggested [66] and developed [67] by the Milano group, is based on the use of low temperature calorimeters (*bolometers*). Besides providing very good energy resolutions they can in fact practically eliminate any constraint in the choice of the $\beta\beta$ emitter. Due to their very simple concept (a massive absorber in thermal contact with a suitable thermometer measuring the temperature increase following an energy deposition), they are in fact constrained only by the requirement of finding a compound allowing the growth of a diamagnetic and dielectric crystal. Extremely massive [68] detectors can then be built, by assembling large crystal arrays.

Isotope	$Q_{\beta\beta}$ [keV]	i.a. [%]	$T^{2\nu}_{1/2}$ [y]
^{48}Ca	4271	0.187	$(4.2 \pm 1.2) \times 10^{19}$
^{76}Ge	2039	7.8	$(1.3 \pm 0.1) \times 10^{21}$
^{82}Se ‡	2995	9	$(9.6 \pm 1.0) \times 10^{19}$
^{100}Mo ‡	3034	9.6	$(7.11 \pm 0.54) \times 10^{18}$
^{116}Cd	2806	7.5	$(2.9 \pm 0.4) \times 10^{19}$
^{130}Te ‡	2528	33.9	$(6.1 \pm 1.4) \times 10^{20}$
^{136}Xe	2479	8.9	$> 1.6 \times 10^{22}$
^{150}Nd	3367	5.6	$7.0^{+11.8}_{-0.3} \times 10^{18}$

Isotope	$T^{0\nu}_{1/2}$ [y]	$\langle m_\nu \rangle$ [eV]	$\langle m^\dagger_\nu \rangle$ [eV]
^{48}Ca	$> 9.5 \times 10^{21}(76\%)$ [57]	< 8.3	< 30
^{76}Ge	$> 1.9 \times 10^{25}$ [55, 58]	< 0.35	$< 0.35 - 0.96$
	$> 1.6 \times 10^{25}$ [59, 56]	$< 0.38 - 1.05$	$< 0.38 - 1.05$
^{82}Se ‡	$> 1.0 \times 10^{23}$ [60]	$< 1.7 - 4.9$	$< 2.2 - 6.9$
^{100}Mo ‡	$> 4.6 \times 10^{23}$ [60]	$< 0.7 - 2.8$	$< 1.36 - 3.3$
^{116}Cd	$> 1.7 \times 10^{23}$ [61]	< 1.7	$< 1.5 - 5.3$
^{130}Te ‡	$> 1.8 \times 10^{24}$ [62, 63]	$< 0.2 - 1.1$	$< 0.5 - 1.8$
^{136}Xe	$> 1.2 \times 10^{24}$ [64]	$< 1.1 - 2.9$	$< 0.5 - 3.2$
^{150}Nd	$> 1.2 \times 10^{21}$ [65]	< 3	$< 4.6 - 6.5$

Table 1.5: Best reported results on 0νDBD processes. Limits are at 90% C.L. except when noted. The effective neutrino mass limits and ranges are those deduced by the authors ($\langle m_\nu \rangle$) or according to Table 1.2 ($\langle m^\dagger_\nu \rangle$). Only ‡ nuclei are presently investigated by high sensitivity experiments.

Thermal detectors have been pioneered by the Milano group for ^{130}Te (chosen, because of its favorable nuclear factor-of-merit and large natural isotopic abundance, from a large number of other successfully tested $\beta\beta$ emitters) are the argument of this Ph.D. work and will be described in detail later on. The present TeO_2 detector, CUORICINO is characterized by a good energy resolution (7–8 keV on the average at the 0νDBD transition energy, 2528 keV) and a background level of ~ 0.18 (c/keV$\cdot$ kg$\cdot$ y). The quoted limit of 2×10^{24} y on the ^{130}Te 0νDBD half-life, corresponding to a limit of 0.2-0.9 eV on $\langle m_\nu \rangle$, represents the best limit after those reached by Ge diodes experiments (see Table 1.5).

Half-way with next generation experiments, NEMO III [69] is a passive source detector located in the Frejus underground laboratory at a depth of $\sim$ 4800 m.w.e. It consists of a tracking (wire chambers filled with an ethyl-alcohol mixture, operated in the Geiger mode) and a calorimetric (1940 plastic scintillators) system operated in a 30 gauss magnetic field. A well designed source system allows the simultaneous analysis of up to 10 kg of different 0νDBD active isotopes. Despite a relatively modest energy resolution (11% FWHM at 3 MeV), implying a non negligible background contribution from 2νDBD, they achieved very good results on the study

of the 2νDBD spectra of several $\beta\beta$ emitters (^{82}Se, ^{96}Zr, ^{116}Cd, ^{150}Nd). However, regarding the 0νDBD a good result was obtained with ^{100}Mo (see Table 1.5).

In January 2002, a few members of the HM collaboration claimed evidence for ^{76}Ge 0νDBD [70] with $T^{0\nu}_{1/2} = 0.8-18.3\times10^{25}$ y (best value $T^{0\nu}_{1/2} = 1.5\times10^{25}$ y) corresponding to a $\langle m_\nu \rangle$ range of 0.11 – 0.56 eV (best value 0.39 eV). This claim is based on the identification of tiny peaks close to the 0νDBD region of ^{76}Ge, one of them at the energy of the Q-value of the DBD. However this announcement raised immediate scepticism [71]. Several re-analyzes of the data were published by the claim's authors [72, 73, 74, 75], while other authors [76, 77, 78] still criticize the claim. Probably a definite answer to the correctness of the claim will be given only by the very sensitive next generation 0νDBD projects.

1.4 Towards Second Generation Experiments

We have seen that the field of 0νDBD searches is very active. The goal of the future experiments is to reach sensitivities capable of probing the inverted mass hierarchy, i.e. sensitivities in the decay time of the order of $\sim 10^{26}$–10^{27} years. There are several possibilities in order to improve the sensitivities of the experiments. It is up to the experimentalist to choose the philosophy of the experiment and, consequently, to select the detector characteristics, privileging some properties with respect to others, having clearly in mind the final sensitivity of the set-up to half-life and, consequently, to $\langle m_\nu \rangle$. The question is: how to improve the experiments? Most of the criteria that need to be considered when optimizing the design of a new 0νDBD experiment follow directly from Eq. (1.11) combined with Eq. (1.4); the sensitivity at 68% CL on the neutrino mass, $F_{0\nu}$, can be written as

$$S^{0\nu} = \frac{m_e}{\sqrt{cost \cdot N_A}} \frac{1}{\sqrt{G^{0\nu}|M^{0\nu}|^2}} \sqrt{\frac{A}{i.a.\epsilon x}} \sqrt[4]{\frac{B\Delta E}{Mt}} \tag{1.12}$$

1.4.1 Exposure time

The first consideration is that an "improvement" could be simply reached with the present experiments just by measuring for longer time; from Eq. (1.12) we have

$$< m_\nu > |_{t\to\infty} = < m_\nu >_{\Delta T} \left(\frac{\Delta T}{\Delta T + t \to \infty} \right)^{1/4} \tag{1.13}$$

where ΔT is the measurement live time that has allowed the present limit on $<m_\nu>_{\Delta T}$. Now, almost all the experiments (except the CUORICINO and NEMO III experiments, that have, respectively, a live time of $\Delta T \sim 4$ months and of $\Delta T \sim 13$ months) have $\sim\Delta T \geq 2$ y. This implies that to have an improvement of only a factor 2 in the neutrino mass one has to measure ~ 30 years! From this consideration it is also clear that, generally, DBD experiments have a, somewhat, "short" life.

1.4.2 Mass

The mass is one of the "parameters" with which one needs to deal. Regarding this point one has to consider also other variables, i.e. the isotopic abundance. From Table 1.5 we see that all the

interesting $\beta\beta$ emitters (except ^{130}Te) have isotopic abundances of the order of 5–10 %. Let's consider, for example, two experiments with the same environmental natural background and with the same mass; let's suppose that one has the $\beta\beta$ emitter with natural i.a. (for example 5%) while the second has a 90% enrichment; then, from Eq. (1.12), it turns out that the sensitivity of the enriched experiment is a factor $\sqrt{90/5}$=4.2 better with respect to the other. This result can be seen also from another point of view: the time needed for the non enriched experiment to reach the sensitivity of the enriched one will be $(90/5)^2$= 324 times larger. This point is crucial and, in fact, all very sensitive experiments carried out in the past (except the ones based on ^{130}Te) used enriched materials. This holds (see next section) also for the next planned experiments. It is also clear that enrichment is extremely expensive and raises tremendously the cost of an experiment.

Another crucial point comes directly from Eq. (1.10). From Table 1.2 it turns out that the decay time in order to reach a sensitivity on neutrino mass of the order of 10 meV (the goal of the most ambitious next generation experiments) is of the order of 10^{28} y. Thus, assuming a measurement of three years, supposing to have *zero background* (it is clear that this is practically impossible) and considering at least three events for the 0νDBD discovery, then we need to have at least $N^*_{\beta\beta}$=10^{28}/ln2 $\beta\beta$ nuclei, or $\approx 24 \cdot 10^3$ moles. It is therefore clear that the mass scale for the second generation experiments is of the order of a ton. It is also clear that if no signal is detected with the next experiments it will be necessary to cover the normal hierarchy region, i.e. a few meV. Using the same argument it turns out that such *third generation experiments* (if any) should be be able to reach decay times of the order of $\sim 10^{30}$ y with a mass of $\sim$100 ton.

1.4.3 Background

The background is a very delicate point and represent the main task of DBD experiments. There are several background sources that need to be taken into account. Cosmic ray induced background can, in principle, be made negligible operating deep underground and using active shielding to discard events correlated with the passage of a nearby muon. Neutron induced background (mainly (n,γ) reactions) can also be lowered to a negligible contribution by shielding the experimental setup with suitable moderators/neutron-catchers. It turns out, therefore, that the main source of background is the one arising from the natural radioactivity (mainly ^{232}Th and ^{238}U) traces overall present in all kind of materials. Therefore the main concern in order to build an experiment is the screening of materials used for the setup. The present techniques are based on High Purity Ge diodes, neutron activation analysis (for solid and liquid samples), and High Resolution Inductively Coupled Plasma Mass Spectrometry (HR-ICPMS) for liquid samples. The best limits that can be obtained with the first two techniques are around 10^{-11}–10^{-12} g/g (grams of contaminant/grams of sample) while 10^{-13} g/g can be reached on liquid samples. Both techniques are extremely delicate and, moreover, extremely long: for Ge measurement the time needed in order to reach such limits is of the order of several months.

Having screened all the *samples* of materials to be used for the experiment, one has to assemble the setup. *Assuming* that all the batches (also the ones that underwent mechanical machining) are as clean as the screened samples, extreme care has to be used in order to avoid possible re-contamination. Clean room operation is absolutely necessary and operation in "synthetic" air (without Radon) or under clean atmosphere (pure nitrogen) is necessary. The background levels that need to be reached for the next experiments (see Sec. (1.5)) require reduction of the order of 10–100 (this means 10–1 c/(keV $\cdot$ ton $\cdot$ y)) with respect to the previous "pilot" experi-

ments. These levels of radiopurity cannot be *directly* tested with the standard techniques [79], so that the only way to measure them will be the experiment itself. Many physicists consider this somehow as "a bet".

Strictly connected with the background is also the choice of the $\beta\beta$ emitter. Apart some *extremely rare* high energy γ's from the ^{238}U chain, the highest natural γ line arising from natural radioactivity is the 2615 keV line of ^{208}Tl (from ^{232}Th chain). It would be, therefore, extremely useful to choose a $\beta\beta$ emitter with a $Q_{\beta\beta}$ value above this energy.

1.4.4 Energy resolution

Energy resolution will be the key point for some future experiments. Apart from the obvious role played in Eq. (1.12), there is another fundamental aspect that has to be addressed. Assuming also the ability to reduce all the background sources, there is an intrinsic, unavoidable, undistinguishable "background": the 2νDBD. This source of background didn't play a reasonable role in the present and past experiments due to the "low" sensitivity reached. As pointed out in [80] the fraction F of 2νDBD events that are contained in the ΔE^{FWHM} energy window centered at the $Q_{\beta\beta}$ value is given by

$$F \approx 7\frac{Q_{\beta\beta}\delta^6}{m_e} \quad , \quad \delta = \frac{\Delta E^{FWHM}}{Q_{\beta\beta}} \tag{1.14}$$

An expression for the 0νDBD signal (S) to the 2νDBD background (B) ratio can be written

$$\frac{S}{B} \approx \frac{m_e}{7Q_{\beta\beta}\delta^6}\frac{T^{2\nu}_{1/2}}{T^{0\nu}_{1/2}} \tag{1.15}$$

For example, looking at Table 1.5, taking $T^{2\nu}_{1/2} \approx 10^{20}$ y and $Q_{\beta\beta} \approx 3$ MeV, in order to reach a sensitivity on $T^{0\nu}_{1/2}$ of the order of $10^{27}(10^{28})$ y with S/B=1 the energy resolution should be less than 3.7 (2.5) % FWHM at the $Q_{\beta\beta}$ value. This energy resolution is extremely challenging for all detectors except Ge diodes and bolometers that have, normally, energy resolutions of the order of 0.2–0.4 % FWHM. For the sake of completeness it has to be noted that the S/B ratio can be slightly enhanced by choosing an asymmetric analysis window defined as $Q_{\beta\beta} < E < Q_{\beta\beta} + \Delta E^{FWHM}$.

1.5 Future Experiments

So far, the best results have been obtained by exploiting the calorimetric approach (active source detectors) which characterizes therefore most of the future proposed projects. Actually, a series of new proposals has been boosted by the recent renewed interest in 0νDBD following neutrino oscillation results. It is not so easy to classify them:

1. High energy resolution calorimetric experiments based on already consolidated techniques with improvements in background suppression/rejection (e.g CUORE, GERDA, MAJORANA).

2. Calorimetric experiments based on consolidated techniques of scintillation light detection (CANDLES, CAMEO).

3. Calorimetric experiments with or without background identification techniques based on *non standard* techniques that require further R&D (EXO, XMASS).

4. "Passive" experiments based on standard techniques that requires R&D (SUPERNEMO, MOON, DCBA).

Expected sensitivities on $T^{0\nu}_{1/2}$ of the proposed projects are compared in Table 1.6. The sensitivities on $\langle m_\nu \rangle$ are evaluated using Table 1.2. In many cases technical feasibility tests are requested, but the crucial issue will be the capability of each project to pursue the expected background suppression.

Table 1.6: Expected sensitivities of future projects. Last column evaluated from Table 1.2.

Experiment	Isotope	kMoles ($\beta\beta$)	$T^{0\nu}_{1/2}$ (10^{26} y)	$\langle m_\nu \rangle$ (meV)
CUORE [81]	^{130}Te	1.6	7	(46-91)
EXO [82]	^{136}Xe	48	130	(5-30)
GERDA [83]	^{76}Ge	0.5	2	(105-300)
MAJORANA [84]	^{76}Ge	5.6	40	(24-66)
MOON III [85]	^{100}Mo	8.5	30	(15-36)
XMASS [86]	^{136}Xe	6.1	30	(9-63)
DCBA [87]	^{150}Nd	2.7	1	(16-55)
SUPERNEMO [88]	^{82}Se	1.1	2	(55-170)
CAMEO III [89]	^{116}Cd	2.7	10	(20-68)
CANDLES IV [90]	^{48}Ca	0.6	30	(55)

Many proposals have been recently suggested. However most of them are not officially approved or require further R&D to actually prove the feasibility. A complete report can be found in [91, 92].

GERDA [83] (*GERmanium Detector Array*) is the only completely approved and funded experiment. It will be carried on in the INFN Gran Sasso National Laboratories. It is based on the technique already suggested by the HM collaboration [93]: "naked" Ge diodes will be suspended in the centre of a very large liquid nitrogen container, which will act as a very effective shield. The experiment will consists of two phases: in the first one the *same* detectors of the HM collaboration and the IGEX collaboration will be "naked", removing all the components that are not needed for operating them in liquid nitrogen. The total mass will be ~ 17 kg of % 86 enriched ^{76}Ge. The collaboration will probe the HM claim within the first 1-2 years. They plan to reach *zero* background in the 0νDBD region. Therefore, if the result of the HM collaboration is true they will expect to confirm it at 5σ C.L. within the first year of operation. The second phase will consist of the addition of new enriched detectors for a total mass of 60 kg (0.7 Kmol).

For the second phase they will use background discrimination techniques and they, again, quote *zero background*. The first phase should start data taking in 2007.

CUORE [81] (*Cryogenic Underground Observatory for Rare Events*), the extension of CUORICINO, will be described in detail in Chapter 5. Among all the proposed experiments it is the only one that needs a background suppression of "only" a factor 10 with respect to the "pilot" CUORICINO experiment. A factor of two was already achieved in 2004. The expected sensitivity will be $7 \cdot 10^{26}$ y. The experiment should start in 2009.

MAJORANA [84], which involves many of the IGEX collaborators, will consist of an array of 210 isotopically enriched Ge diodes for a total mass of 0.5 tons. As opposed to the GERDA design, the use of a very low activity conventional cryostat (extremely radiopure electroformed Cu) able to host simultaneously a large number of diodes is proposed. The driving principle behind the project is a strong reduction of the background by the application of very effective pulse-shape discrimination and the development of special segmented detectors. Despite the very promising R&D developed in the last years, the project is not yet funded.

Chapter 2

Bolometric Technique

The expression "bolometer" is normally used to indicate a Low Temperature Detector (LTD) in which the energy of particle interactions is converted into phonons and measured via temperature variation.

In this chapter the basic operation principles are briefly presented and the different detector components are described. Typical behaviors are compared with the ones of conventional detectors, highlighting the advantages and disadvantages.

2.1 Low temperature detectors

Conventional techniques for energy deposition measurements are based on the detection of the energy released in the form of ionization and excitation of the detector's atoms. Unfortunately, the amount of energy lost in channels different from the detected ones is quite large. Most of the energy is converted in phonon excitations inside the detector. This energy loss, together with the comparatively high energy value necessary for an atom excitation or ionization (the elementary detected event), increases the statistical fluctuations of the number of elementary excitations, thus making the intrinsic energy resolution of such detecting techniques worse.

Thermal detectors measure the portion of the deposited energy converted in phonons by the means of the the corresponding temperature rise. As it will be shown later this guarantees a better intrinsic energy resolution.

The use of temperature detectors to study nuclear phenomena was first suggested by Simon [94] about 60 years ago. In 1949 Andrews detected for the first time the alpha particles using superconductive bolometers [95]. The possibility to use thermal detector for many topics of research (solar neutrino spectroscopy, X ray spectroscopy, material contamination analysis, dark matter detection and rare processes search) was a strong motivation for the development of this technique. The use of large bolometric detectors is quite recent for rare events physics, and was first suggested by Fiorini and Niinikoski in 1983 [66]. Nevertheless, this technique revealed to be very powerful in many different applications and generate great developments.

2.2 Operation Principles of bolometric detectors

A LTD consists normally of two main components: the *energy absorber*, where the particles deposit their energy, and the *sensor*, which converts the excitations produced by the particle

interaction into a signal. Bolometers are LTDs sensitive to phonons. These devices are therefore

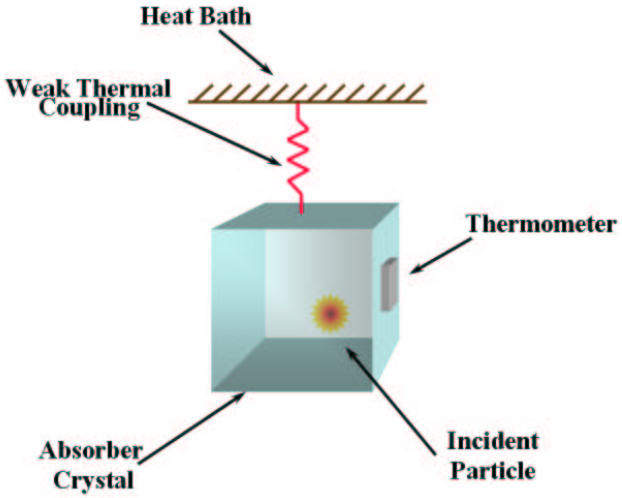

Figure 2.1: Scheme of a bolometric detector.

named Phonon Mediated particle Detectors (PMDs) and their sensitive element is, consequently, a *phonon sensor*. A simple scheme of a bolometric detector is shown in fig. 2.1.

A PMD can be roughly schematized as heat capacity C connected to a heat sink at constant temperature (T_0) via a thermal conductance G (see Fig. 2.2). The heat capacity C contains all the contribution of the elements that compose the detector: lattice heat capacity of the absorber and electronic and lattice heat capacity of the sensor. The conductance G represents the thermal connection between the detector and the heat sink and its heat capacity is considered negligible. We assume that, for a given absorber temperature $T(t)$, $\Delta T = |T(t) - T_0| \ll T_0 \ \ \forall t$ so that we can treat C and G as constants.

When a particle interaction occurs in the energy absorber, the phonons produced are out of equilibrium (athermal phonons). The athermal phonons, trough different interactions, degrade their energy and relax onto a new equilibrium distribution (see section 2.3.1). This new distribution is measured by mean of the sensor as a temperature variation:

$$\Delta T(t) = \frac{\Delta E}{C} \exp\left(-\frac{t}{\tau}\right) \qquad \text{where} \quad \tau = \frac{C}{G} \tag{2.1}$$

where τ is decay time of the thermal signal. The heat capacity at the temperature T is given by $C(T) = c(T) \cdot n$ where $c(T)$ is the specific heat at a temperature T and n is the number of moles in the absorber. Since $T_{Max} \propto \frac{\Delta E}{C}$, the smaller the C is the higher is the signal amplitude. The only possibility to have very small heat capacities is to work at very low temperatures. In fact a 1 MeV particle impinging on a absorber crystal of 1 mole at room temperature generates a variation ΔT of $10^{-18} - 10^{-15}$ K which is impossible to measure. Typical operating temperatures for bolometers are in the range between 10 and 100 mK.

According to which type of phonon sensor is used, the PMDs are classified as fast or slow bolometric detectors. In the first case they have a response time of the order of microseconds

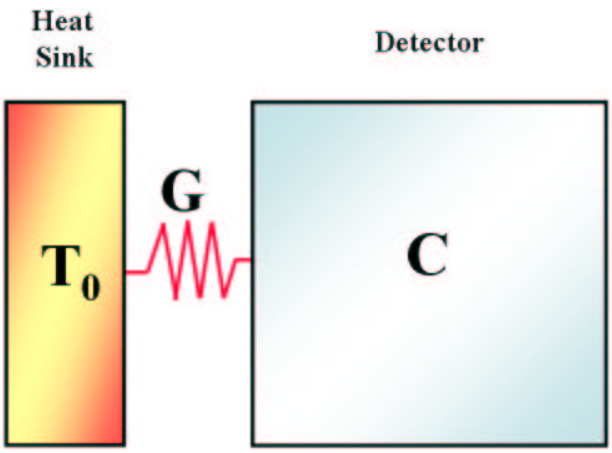

Figure 2.2: Monolithic thermal model. Here the detector is modeled as a unique system weakly coupled to the heat sink.

and can be sensitive to athermal phonons. If the phonon sensor response time is bigger than the thermalization time of the non-equilibrium phonons produced by the particle interaction (hundreds of msec.), it will be sensitive mainly to thermal phonons. In the latter case, the sensor measures the temperature of the detector and thus it is a thermometer. The PMD works then as a perfect calorimeter. In many experimental situations, it is difficult to distinguish between these two extreme cases, and the nature of the detection mechanism is still poorly known.

2.3 The energy absorber

The main results that can be derived from the simple model described above are the height of the PMD thermal signal and the time constant of the signal. If we assume that the detector operates as a perfect calorimeter, the hight of the signal corresponds to the ratio between the energy E deposited by the particle and the heat capacity C of the detector, E/C. The time constant is equal to the ratio between the heat capacity and the thermal conductance G to the bath, C/G. The most important parameter of the detector is then the heat capacity that has to be small to achieve big and fast signals. This condition is not very difficult to achive and therefore there is a wide choice for the energy absorber materials.

At low temperatures the specific heat of a crystal can be expressed as:

$$c(T) = c_r(T) + c_e(T) \tag{2.2}$$

where c_r represents the lattice contribution to the specific heat and c_e the electron one. Dielectric diamagnetic materials are preferred as energy absorbers, as only the lattice contribution is present. Furthermore, it is proportional to the cube of the temperature over the Debye temperature (Debye law) at low temperatures:

$$c_r(T) = \frac{12}{5}\pi^4 k_B N_A \left(\frac{T}{\Theta_D}\right)^3 \tag{2.3}$$

where k_B, N_A and Θ_D are the Boltzmann constant, the Avogadro number and the Debye temperature respectively. This contribution can be written in terms of heat capacity as

$$C(T) = \beta \frac{m}{M} \left(\frac{T}{\Theta_D} \right)^3 \tag{2.4}$$

where β=1944 J K^{-1}mole^{-1}, m is the absorber mass, and M is the molecular weight. In metals, the specific heat is dominated by the electron contribution

$$c_e(T) = \frac{\pi^2}{\Theta_D} ZR \frac{T}{\Theta_F} \tag{2.5}$$

where Z, R and Θ_F are the conduction electron number for each atom, the gas constant and the Fermi temperature respectively. However, if the metal is in superconductive state, then the electron contribution to the specific heat at T « T$_c$ is

$$c_e(T) = K_s e^{-2(\frac{T_c}{T})} \tag{2.6}$$

where K_s is a constant depending on the material characteristics.

Finally the best choice for absorbers are dielectric and diamagnetic materials (for which the heat capacity is described by eq. 2.4) with high Debye temperature. A good choice are superconductive materials with the T_c well above the working temperature. The absorber dimensions usually depend on the type of the LTD applications. The dimensions range from micrograms, in case of X-ray spectroscopy [96], to kilograms in case of Gamma-ray spectroscopy, DBD and Dark Matter searches [97].

2.3.1 Thermalization processes of the deposited energy

In this section the processes that allow the conversion of the deposited particle energy into thermal phonons will be presented, in order to better understand the detector operation. The main thermalization processes occur through the nuclear and electronic channels [98].
Nuclear channel: the particle interactions with the crystal lattice produce vibrational excitations thanks to the nuclear scattering, but could also produce structural damages of the lattice, where the energy can be stored. If this energy is not converted into phonons, the statistical fluctuation of the number of the produced defects can worsen energy resolution. The fraction of lost energy depends on the incident particle: for electrons and photons it is negligible, whereas for α particles having some MeV of energy it can cause a FWHM resolution of hundreds of eV.
Electronic channel: let's take into consideration the kinetic energy transfer from a charged particle produced by a nuclear process to a semiconductor crystal. The particle is slowed down in few μm (heavy particles) or mm (electrons) from its interaction point and normally stops in the crystal. Along its track it produces many electron–hole pairs having at the beginning very high spatial density and energy. These charge carriers interact first with each other and spread very quickly inside the crystal. As a quasi–equilibrium situation is reached, they undergo their final degradation via direct interaction with the lattice site: these interactions produce phonons.

During this step undesirable processes can take place, indeed a fraction of the pair energy can leave the crystal or can be stored in stable or metastable states instead of going into the crystal lattice. It is possible to have: *radiative recombinations* of e–h couples with the escape of

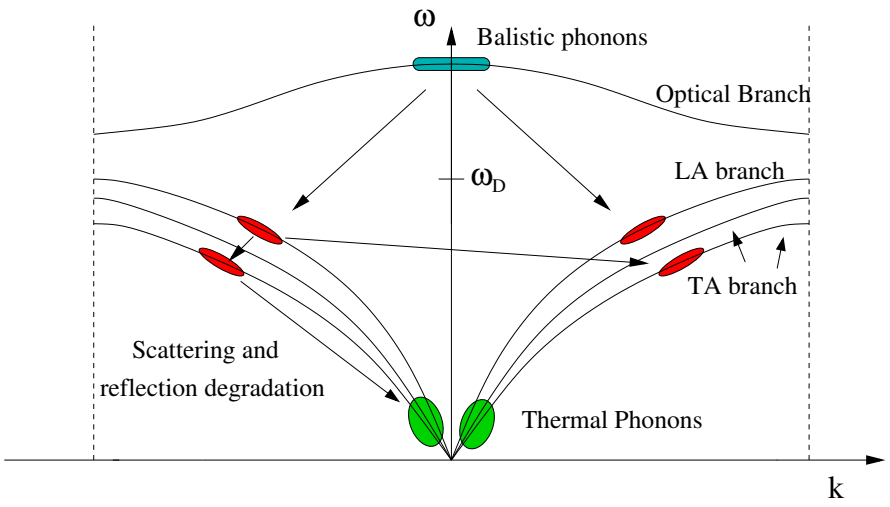

Figure 2.3: Athermal phonon thermalization model

the emitted photon, *non-radiative recombinations* that take too much time compared to signal development, *trapping* of electrons and holes in the impurity sites or lattice defects. A large fraction of the initial energy is transferred to the lattice as vibrational excitations (phonons), through different mechanisms depending on the e–h pair density and on their energy.

Let's consider now the phonon thermalization processes. To explain what happens, it is useful to use the mono-dimensional representation of the phonon dispersion curves. The e–h pair recombination process across conduction and valence bands, produces high energy and low momentum phonons on the optical branch. Then these primary phonons depart from the particle interaction region. The optical phonons decay in the *longitudinal acoustic* (LA) branch in a very short time ($10 - 100$ ps). Obviously, the decay obeys the energy and momentum conservation laws, and it produces mainly two phonons each having half of the energy of the initial particle (of the order of the Debye energy) and opposite momentum. Also the e–h recombinations that happen on impurity levels contribute to this phonon population. Therefore the final result is a phonon system, mainly belonging to the LA branch, and having the energy of the order of $\hbar\omega_D$ (where $\omega_D = 2\pi\nu_D$, and where ν_D is the Debye cut–off frequency of the crystal). This energy is much higher than the average energy of thermal phonons at the bolometer working temperature (for example, at T= 10 mK, the average energy is $\sim\mu$eV). At this point new phenomena of phonon energy degradation can occur, so that phonons become thermal phonons. These processes can be classified in three channels: phonon–phonon interaction, scattering on impurities and reflection on crystal surfaces. The first channel is possible thanks to the an-harmonicity of the lattice potential. However, this an-harmonicity is less important when the crystal temperature and the phonon energy decrease. Moreover, while the LA phonon decay is allowed and it is responsible for the *transverse acoustic* (TA) phonon production, the decay of the TA phonons is forbidden by the momentum conservation law. From these two considerations it is easy to understand that other energy degradation mechanisms must exist to permit, in a reasonable time, the thermalization of the energy trapped in the athermal phonons. These mechanisms are able to degrade phonon energy and also to induce the conversion of the TA phonons, otherwise stable,

into LA phonons so that they can be thermalized. The conversion towards low energies is a very slow process, but it is difficult to make a quantitative estimation due to the complication of the involved mechanisms.

Let's go back to the decay process. After a certain number of the decays, the mean free path becomes larger than crystal dimensions. At this point in pure crystals, there is a ballistic propagation of phonons until they reach the crystal surfaces [99]. Using several fast sensors (able to detect athermal phonons) it is possible in principle to determine the particle interaction point using the phonon signal relative time [100]. Phonons that are not absorbed by a sensor will be reflected by surfaces and therefore they can suffer decay processes. At the end they interact with the background thermal phonons and they thermalize.

For superconductor materials, the thermalization processes can be longer. This happens in particular when the Debye temperature θ_D for the material is large and the critical temperature T_c is low. In fact, in this case, phonons that are generated by particle interactions easily break the Cooper pairs and cause an energy storage in the quasi–particle system. For this reason, even in the case when superconductive materials present lower heat capacity at the same temperature, the diamagnetic dielectric materials are to be preferred.

2.3.2 Intrinsic energy resolution

By thermodynamic considerations that will be explained in sec. 2.5.2 it is possible to express the intrinsic energy resolution ΔE for a bolometric detector sensitive to thermal phonons as

$$\Delta E = \sqrt{k_B C(T) T^2} \tag{2.7}$$

where k_B and C are the Boltzmann constant and the energy absorber heat capacity respectively. To give an idea of the potentiality of these devices we can calculate that for 1 kg of TeO_2 working at 10 mK the intrinsic energy resolution is about 10 eV. Once again we see that a crucial parameter of the energy absorber is its Debye temperature, θ_D, which has to be as high as possible in order to reduce the specific heat. For this reason, light materials with a small mass number are better energy absorbers in terms of heat capacity. Even superconductors are in principle suitable, since the electronic contribution to the specific heat vanishes exponentially below the critical temperature, but the *caveats* exposed in the previous section have to be taken into account.

It should be stressed that, according to eq. 2.7, ΔE is independent of E. However, even in the case of athermal phonons, it is possible to see the advantage of PMDs over conventional devices for radiation spectroscopy as the energy resolution is concerned. In fact the energy interaction generates a number of elementary excitations, N, equal to

$$N = \frac{E}{\epsilon}$$

where ϵ is the energy to produce an elementary excitation. The intrinsic energy resolution is limited by the statistic fluctuation of the produced elementary excitation number. So the theoretic energy resolution ΔE is

$$\frac{\Delta E}{E} = 2.35 \cdot \frac{\Delta N}{N} \tag{2.8}$$

that is proportional to the $\sqrt{\epsilon}$. In a scintillator detector ϵ is about 100 eV, whereas in a gas detector and in a solid state detector ϵ is about 30 eV and around 3 eV respectively. As already said, in a PMD the energy of an elementary excitation is less than 0.01 eV even in the case of athermal phonons, so, at least in principle, energy resolutions more than an order of magnitude better than the ones of conventional devices are possible.

2.4 The phonon sensor

The phonon sensor is a device that collects the phonons produced in the absorber and generates an electrical signal, proportional to the energy contained in the collected phonons. A simple realization of this device can be accomplished through the use of a thermistor whose resistance, as a function of the temperature, has a steep slope. In practical devices, there are two main classes of thermistors which give the best results: semiconductor thermistors (STs) and transition edge sensors (TESs). Thermistors are usually characterized by their "logarithmic sensitivity" A, defined as

$$A = \left| \frac{d \log R(T)}{d \log T} \right| \tag{2.9}$$

The value of the sensitivity is usually in the range 1–10 for STs and in the range 10^2–10^3 for TESs.

Here the two approaches are introduced, but in the next part of the chapter the attention will be focused on STs.

2.4.1 Transition Edge Sensors

The TESs are superconductive films kept around the critical temperature (T_C). They are intrinsically fast, and so they can detect athermal phonons. Their working point lies in a narrow range of temperature. A typical example of a resistance-temperature curve for a TES is shown in fig. 2.4. The superconductive film is deposited on the absorber crystal, with typical thickness of a few hundred nanometers [101]. This technique can take advantage of the SQUID technology as read-out. TESs are made normally only by a single superconductor, but it is possible also to use a bilayer film formed by a normal metal and a superconductor. In the latter case, because of the proximity effect, the normal metal is driven superconductive and the resulting T_C can be much lower than that of the pure superconductor. In this way it is possible to tune the T_C by adjusting the thickness of the layer.

2.4.2 Semiconductor Thermistors

As the STs are intrinsically slow, they are probably sensitive mainly to thermal phonons in a PMD (typically they cannot follow signal rates larger than few Hz). In this context, they give information about systems in thermal equilibrium, and could be thought as temperature sensors. However, it must be remarked that there are clear indications that also athermal phonons can be detected by STs; in this case the collected pulses contain also non thermal components. STs consist normally of Ge or Si small crystals with a doped region. A very useful technique to uniformly dope large volumes is the Neutron Transmutation Doping (NTD). In this approach

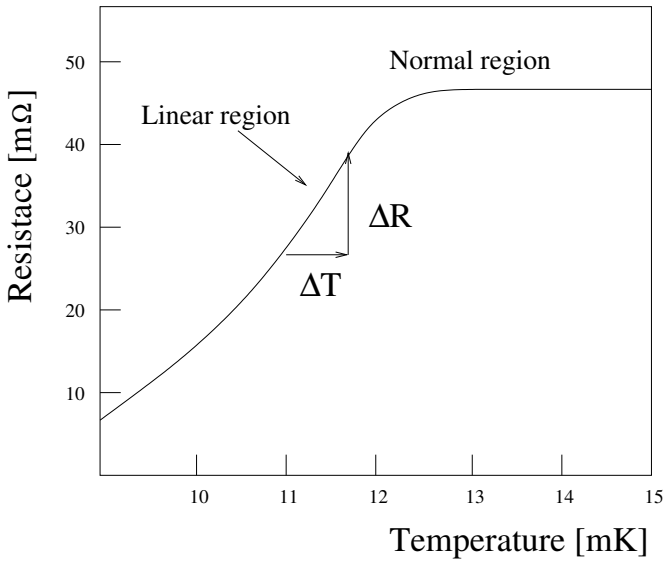

Figure 2.4: Resistance of a W TES thermistor as a function of the temperature.

the semiconductor sample is bombarded by neutrons, which induce nuclear reactions on the various target isotopes leading to the formation of n- and p-dopants. On the other hand, small low-heat-capacity thermistors can be obtained by ion implantation in Si, according to the procedures of the standard planar Si technology.

Conduction processes

For both the previously described approaches, the result is a strong dependence of the sensor resistance on the temperature as follows:

$$\rho \simeq \rho_0 \cdot \exp\left(\frac{\epsilon(T)}{k_B T}\right)^{1/2} \tag{2.10}$$

where k_B is the Boltzmann constant, $\epsilon(T)$ is the activation energy and ρ_0 is a parameter depending on the doping conditions.

Semiconductors are covalent solids that may be regarded as insulators because the valence band is completely full and the conduction band is completely empty at the absolute zero. They present an energy gap between the valence and conduction bands of no more than 2 eV. For silicon the energy gap is 1.14 eV and for germanium the gap is 0.67 eV. So, for intrinsic semiconductors, i.e. for a semiconductor without impurities, the conduction can happen only with an activation energy equal or larger than the energy gap. This mechanism is possible if the working temperature is T » T_{amb}, since $kT \simeq 0.025$ eV at room temperature.
If impurities are present in the semiconductor lattice (extrinsic or doped semiconductors) then it is also possible to have electronic conduction also at lower temperatures. In this case in fact, the impurities introduce discrete levels slightly above the top of the valence band or under the bottom of the conduction band, depending on the type of atoms inserted in the semiconductor.

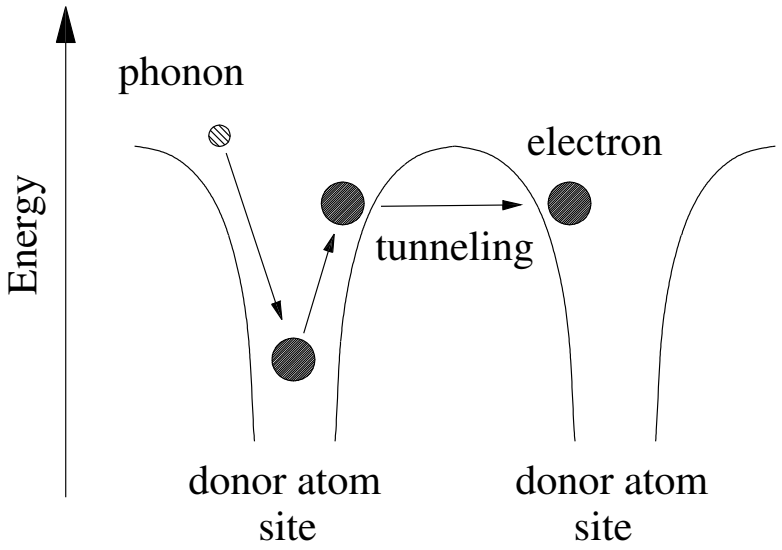

Figure 2.5: Schematic representation of hopping conduction mechanism.

For low impurity concentrations, the localized energy levels of dopant atoms are not broadened into bands because these atoms are many lattice spacings apart and they interact with each other very weakly. The energy difference $\Delta\epsilon$, between the donor impurity energy levels and the conduction band, is small, as well as between the acceptor impurity energy levels and the valence band. Moreover if a small amount of arsenic impurities is introduced in a germanium crystal, a energy activation equal to $\Delta\epsilon$ = 0.0127 eV is obtained. The conduction mechanism due to dopant sites dominates the conduction at room and lower temperatures. Depending on the number of dopant atoms, the semiconductor, also near the zero temperature, can behave as an insulator or a metal. So, there exists a critical concentration N_c that characterizes the transition from the insulator to the metallic behavior of the semiconductor. The region near this concentration is named metal-insulator transition region (MIT) [102].

At temperatures lower than 10 K, the conduction is due to the migration of charge carriers from an impurity site to another. When the donor concentration is increased, the wave function of the external electron of the donor atom overlaps with the external electron wave function of the neighboring atoms. In this situation the electrons are not localized and the conduction happens when electrons jump from a donor site to another (*hopping mechanism*) without using the conduction band. This migration is due to quantum-mechanical tunneling through the potential barrier which separates the two dopant sites. The conduction is activated by phonon mediation as schematically described in fig. 2.5, in which the tunnelling process is also shown.

If T $\ll$ 10 K and if the net doping atom concentration is slightly lower than N_c, then the resistivity is strongly dependent on the temperature. For this reason, usually, it is chosen to operate semiconductor thermistors slightly below the MIT region. The dominant conduction mechanism in these conditions of temperature and dopant level is named "Variable Range Hopping" (VRH [103]) and the carriers can migrate also on far sites if their energy levels are located in a narrow range around the Fermi energy. As the state density near the Fermi energy in the semiconductor is determined by compensation level K, it plays a fundamental role in the VRH

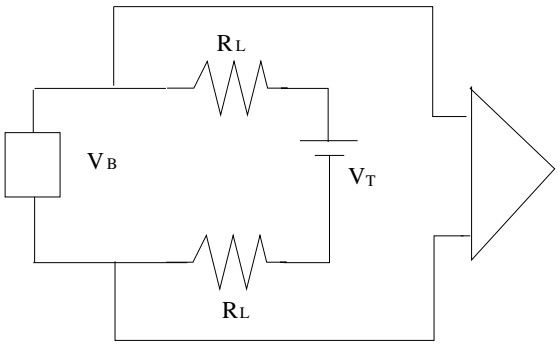

Figure 2.6: Electric scheme of the bias current circuit used for the read-out of a bolometer. R_L is the load resistance

process. Let's recall that K is equal to the ratio between the acceptor concentration N_A and the donor concentration N_D.

For VRH, the resistivity depends on the temperature in the following way:

$$\rho = \rho_0 \cdot \exp\left(\frac{T_0}{T}\right)^{\gamma} \tag{2.11}$$

where ρ_0 and T_0 are parameters depending on the doping and compensation levels. The exponent γ is equal to $\frac{1}{4}$ in the Mott model, for a three-dimensional system and for low compensation levels. For larger values of K, the Coulomb repulsion among the electrons leads to the formation of a gap (Coulomb gap) in the electron state density near the Fermi energy. The value of γ in this case becomes $\frac{1}{2}$.

In the following sections, attention will be focused on the case of bolometers using STs as sensors.

2.5 Detector operation

From the considerations in the previous section, it is clear that the sensor converts thermal pulses into electrical signals. To obtain a voltage signal a steady current (bias current) I is sent trough the thermistor by means of the bias circuit shown in fig. 2.6, where R_L is the load resistance, R(T) is the sensor resistance and V_B is a constant voltage generator. In these conditions a voltage V(T) = I · R(T) appears across the sensor. This produces a power dissipation P which increases the temperature and acts back on the resistance $R(T)$, until an equilibrium is reached. In static conditions the absorber's temperature T_b is

$$T_b = T_0 + \frac{P}{G} \tag{2.12}$$

where T_0 is the heat sink temperature and G the conductance to the bath. This phenomenon makes the V-I relation deviate from linearity and leads to a non-ohmic behavior. This characteristic behavior of bolometers is often referred to as "electrothermal feedback". The static

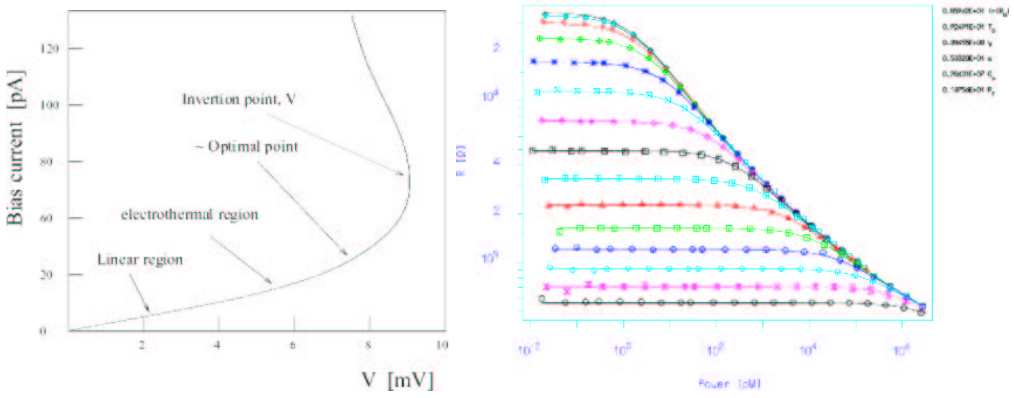

Figure 2.7: Typical load curve, current–voltage characteristic(left) and typical P-R characteristics of a semiconductor thermistor.

resistance is simply the ratio V/I while the dynamic resistance is the tangent at the V-I curve. By further increasing the bias current the dynamic resistance crosses the so called inversion point (where it vanishes) and becomes negative. For semiconductor thermistors, a typical V-I curve, usually referred to as load curve, is represented in fig. 2.7(left). In static conditions the thermistor electric and thermal parameters are described by a point on the load curve. The intersection of the straight line of equation V = V_b - I R_L and the load curve I = I(V) determines the working point of the sensor, as described in fig. 2.7(right). Usually the working point is chosen in such a way that the signal amplitude or the signal-to-noise ratio is maximum (optimal working point). By a combined fit to a set of load curves at different base temperatures, all the thermistor parameters (R_0, T_0, γ) are evaluated as it can be seen in fig. 2.7 where R-P load curves for the same Si-ST at different base temperatures are shown with their corresponding fits.

2.5.1 Detector signal amplitude

In the first approximation the thermal pulse produced by an energy release in the absorber is characterized by a very fast rise time, that in monolithic approximation is instantaneous if the thermalization time is assumed negligible, and by an exponential decay time depending on the physical characteristics of the individual detector (equal to the ratio between the heat capacity and the conductance to the bath in case of the monolithic model assumption). Such a thermal pulse is then converted into an electrical one by means of the thermistor bias circuit and the detector optimization is achieved by finding the best configuration for a maximum pulse amplitude. Considering the basic circuit shown in fig. 2.6, it is straightforward to obtain the relationship between the maximum voltage signal (ΔV), the thermistor parameters and the deposited energy E:

$$\Delta V = \frac{R_L}{R_L + R} \cdot V \cdot A \cdot \frac{\Delta T_b}{T_b} \sim \frac{E}{C \cdot T_b} \cdot A \cdot \sqrt{P \cdot R} \tag{2.13}$$

where T_b is the static detector temperature, ΔT_b is the increase of detector temperature, A is the sensor's logarithmic sensitivity of eq. 2.9, P is the power dissipated in the thermistor by Joule effect and R is the sensor resistance. This expression vanishes both in the limit P $\rightarrow$ 0 and

P $\rightarrow \infty$. To increase the signal amplitude, a higher V operation point could be chosen, but normally without surpassing the inversion point V_i on the load curve. Usually the best working point does not correspond to the V_i voltage, as the increase of the applied voltages determines higher temperatures and so lower ΔT/T ratios. For each detector, it is necessary to determine the optimal working point experimentally.

2.5.2 Detector noise

In this section the principal noise sources of a bolometric detector using a ST sensor will be presented. These sources can be classified as generating intrinsic and extrinsic noise.

- It is not possible to totally eliminate intrinsic noise sources that determines the energy resolution limit of detector. As these sources depend on detector parameters, they have to be carefully analyzed to achieve the optimal experimental configuration.
- The extrinsic noise sources is the totality of noise sources not generated inside the detector, such as cryogenic apparatus, electronics and read-out set-ups. In the bolometers described in this thesis they dominate the intrinsic noise, so that they determine the real limits of the energy resolution. There are also other sources of noise that can be included in this category, such as a electric microphonic noise, electromagnetic interferences, and mechanical microphonic noise. These can not be classified as intrinsic noise of the detectors or as consequence of the electronic read-out of bolometers but they can seriously affect detector performance.

The extrinsic noise sources are characteristic of the experimental set-ups, and will be analyzed in detail in the next chapters for given experiments. Here the description of the two main intrinsic noise sources follows:

Johnson Noise: Every resistance R working at a temperature T_b generates a white noise having a power spectrum given by:

$$e_R = \sqrt{4k_B R T_b} \tag{2.14}$$

If the monolithic model is used it is possible to demonstrate that the Johnson noise at low frequency is reduced by the electrothermal effect. The scheme in fig. 2.6 shows that the sensor is biased using a R_L load resistance that is, in general, at a temperature T_L different from T_b. (For instance, at room temperature, as in most of the devices described in the following chapters.) Therefore the Johnson noise of the load resistance R_L has to be taken into account, but it is possible to demonstrate that this can be made negligible when compared to the detector noise; in fact the load resistance contribution to the detector noise, e_{det}, is

$$e_{det} = e_{R_L} \left(\frac{R}{R_L + R} \right)^2 \tag{2.15}$$

This contribution can therefore be reduced *ad libitum* by choosing a large enough value for R_L.

$$\frac{e_{det}}{e_R} = \frac{e_R}{e_{R_L}} \left(\frac{R}{R_L} \right)^2 = \frac{R}{R_L} \cdot \frac{T_L}{T} \tag{2.16}$$

Thermodynamic Noise: As already anticipated in sec. 2.3.1, in the case of complete energy thermalization, the intrinsic energy resolution is limited by the thermodynamic fluctuations of the number of thermal phonons exchanged with the heat bath through the conductance G. This produces energy fluctuations and therefore temperature fluctuations in the absorber, i.e. an intrinsic detector noise. An estimate of this noise can be obtained by the following simplified argument. The number of phonons contained in the absorber at thermal equilibrium can be estimated as

$$N = \frac{E}{\epsilon_a} = \frac{C(T) \cdot T}{k_B \cdot T} = \frac{C(T)}{k_B} \tag{2.17}$$

where the mean phonon energy ϵ_a is expressed as equal to $k_B \cdot T$ and E is the internal energy of the absorber [104]. If Poisson statistics is assumed then it is possible to estimate the fluctuations of the internal energy of the absorber in the following way:

$$\Delta E = \Delta N \cdot k_B T = \sqrt{N} \cdot k_B T = \sqrt{\frac{C(T)}{k_B}} \cdot k_B T = \sqrt{k_B C(T) T^2} \tag{2.18}$$

that is the expression already presented in sec. 2.3.1. In the monolithic bolometer model case, a detailed calculation of noise due to intrinsic sources shows that a dimensionless factor ξ has to be introduced as a multiplier for eq. 2.18. The ξ value depends on the details of the temperature sensor, of the thermal conductance and of the heat capacity temperature dependences, and can be made of the order of unity with a proper optimization work.

2.6 Detection of rare events

Finally it should be clear why bolometric detectors found one of their best applications in rare events physics, particularly in DBD and dark matter searches and in neutrino physics (a wide overview is provided by the proceedings of the specific low temperature detector conferences [105]).

First of all, bolometers are intrinsic rare events detectors. Typical time evolutions of the pulses do not allow high radiation rates on the detector (sec. 2.4).

On the other hand, near this time limitation we have many advantages. The most important of them is the energy resolution which is better than that of most of the other particle detectors [67]. The second important feature offered by bolometers is the wide choice of different materials that can be used as absorbers (sec. 2.3). This can be very important in DBD search to be able to confirm on different isotopes a possible evidence and in DM search to span different mass regions.

Chapter 3

TeO_2 bolometric experiments for 0νDBD search

In the late '80s the Milano group, leaded by professor E. Fiorini, published for the first time papers on massive bolometric detectors used to search for rare events [106, 107, 108, 109]. Since the beginning this detectors were developed following the line of action of searching for neutrinoless double beta decay. For this reason most of the experimental activity was carried out in the underground location of Laboratori Nazionali del Gran Sasso (LNGS) of INFN where the mountain provides a 3500 m.w.e. shield against cosmic rays.

The preliminary experiment was performed with 73 g and 334 g single module TeO_2 crystals, reaching a limit for $T^{0\nu}_{1/2}$ of ^{130}Te of 2.1×10^{22} years (90% CL). The second step was an array of 4 detectors, 340 g each, to study the feasibility of a large massive experiment made by identical bolometers. The cumulative limit obtained for $T^{0\nu}_{1}/2$ of ^{130}Te was 2.39×10^{22} years (90% CL) [110].

After these successful results obtained with this first experiments and with a much better understanding of the detectors, a tower–like array of 20 TeO_2 340 g crystals, was projected and proposed to be built. At the end of September 1997 the so–called MiDBD experiment started to operate in the LNGS [111, 112]. A second phase of the experiment, MiDBD II, with the same crystals but with some technical improvements, was started in January 2001. The new achieved limit on $T^{0\nu}_{1/2}$ of ^{130}Te was 2.1×10^{23} years (90% CL) [113], thus obtaining the second best neutrino mass bound (after the ^{76}Ge result).

The knowledge acquired in terms of detector performance, optimization and background reduction was used in the design and realization of a second large mass bolometric experiment, CUORICINO, a 62 TeO_2 array with a total mass of 41.7 kg, that will be described in the next chapter. CUORICINO is a self-consistent experiment but, at the same time, it is a test intended to verify the technical feasibility of CUORE (Cryogenic Underground Observatory for Rare Events). The R&D on CUORE's detectors is the framework on which my PhD work was developed.

In this chapter the TeO_2 bolometric detectors developed by the Milano DBD-group (and by other several groups that joined this activity during the past 20 years) will be presented and described.

3.1 The choice of an absorber for a bolometric experiment

As explained in sec. 2.6 the use of bolometric detectors is related to the search for 0νDBD; in fact, the calorimetric approach provides good energy resolution and thus an increase of the signal–to–background ratio.

The Milano group developed large mass bolometers using TeO_2 crystals. In this section the reasons that lead to the choice of these crystals as energy absorbers will be presented.

3.1.1 The choice of the 0νDBD source: why ^{130}Te ?

The bolometric technique offers a wide choice of DBD candidates (as ^{48}Ca, ^{76}Ge, ^{100}Mo, ^{116}Cd and ^{130}Te), the only requirements being that the candidate nucleus be part of a compound which can be grown in the form of a crystal with good thermal and mechanical properties (see Chapter 2).

The choice of ^{130}Te arises from the necessity of testing 0νDBD in an isotope different from ^{76}Ge but with a competitive sensitivity to obtain crosschecked information. ^{130}Te came out to be a very good compromise between the different features that characterize a DBD experiment. In the following the different features that can be taken into account to choose the best nuclide are described and commented:

- **Isotopic Abundance:** this parameter plays an important role in determining the sensitivity of a DBD experiment (see sec. 6.2), being the sensitivity proportional to the number of nuclei under control. This is much more relevant in experiments (this is the case of bolometers) where the experimental technique does not allow one to increase easily the detector's mass of some orders of magnitude. For this reason, a few per cent of natural isotopic abundance is an unacceptable value. Tab. 3.1 shows a comparison of the natural isotopic abundance for the various candidates to be used as 0νDBD sources. A possible solution to the sensitivity problem for isotopes with very low natural abundance is the isotopic enrichment. Unfortunately, this technique is not always practically feasible and it is often very expensive. From this point of view the isotope ^{130}Te is an optimum choice since its isotopic content in natural tellurium is 33.87% [114].

- **Phase space:** the element of phase space of the transition $G^{0\nu}$, that represents the contribution of pure kinematic of the process of decay, is proportional to Q^5, where Q is the transition energy of the decay. This means that the higher is Q, the bigger is the probability for the decay to occur. The DBD Q-value for ^{130}Te is 2528.8 $\pm$ 1.3 keV and it is reasonably high. In Tab. 3.1 a comparison of the transition energy for the various DBD candidates is reported.

- **Transition energy Q:** the Q-value is also important because its relation with the natural radioactivity background. The Q-value of ^{130}Te (2528 keV) happens to be situated between the peak and the Compton edge of the 2615 keV line of ^{208}Tl , which leaves a clean window to look for the signal. Furthermore, the 2615 keV gamma line is the highest line coming from natural radioactivity; thus no other contributions from gammas of higher energies are to be expected.

- **Nuclear dynamics:** as it was illustrated in Chapter 1 (see eq. 1.5), the lifetime for DBD0ν is inversely proportional with the factor of merit $F_N \equiv G^{0\nu} \mid M_F^{0\nu} \mid^2$. The matrix

Decay			Q(keV)		Ab.(%)
^{48}Ca	$\rightarrow$	^{48}Ti	4271	$\pm$ 4	0.187
^{76}Ge	$\rightarrow$	^{76}Se	2040	$\pm$ .9	7.8
^{82}Se	$\rightarrow$	^{82}Kr	2995	$\pm$ 6	9
^{94}Zr	$\rightarrow$	^{94}Mo	1145	$\pm$ 2.5	17.4
^{96}Zr	$\rightarrow$	^{96}Mo	3350	$\pm$ 3	2.8
^{100}Mo	$\rightarrow$	^{100}Ru	3034	$\pm$ 6	9.6
^{110}Pd	$\rightarrow$	^{110}Cd	2013	$\pm$ 19	11.7
^{116}Cd	$\rightarrow$	^{116}Sn	2802	$\pm$ 4	7.5
^{124}Sn	$\rightarrow$	^{124}Te	2288	$\pm$ 1.6	5.8
^{130}Te	$\rightarrow$	^{130}Xe	2528	$\pm$ 1	33.9
^{136}Xe	$\rightarrow$	^{136}Ba	2479	$\pm$ 8	8.9
^{150}Nd	$\rightarrow$	^{150}Sm	3367	$\pm$ 2.2	5.6

Table 3.1: Some high Q-values DBD candidates with corresponding isotopic abundances. [3]

elements $\mid M_F^{0\nu} \mid^2$ are dominated by the nuclear dynamics and differ from one nuclide to another. As it can be seen from Tab. (1.2.1) it is apparent that in most of the nuclear model used to compute the neutrinoless DBD matrix elements, the nuclear factor of merit of ^{130}Te are a factor is more favorable than that of ^{76}Ge (the emitter for which the best DBD0ν half-life limits had been achieved so far). This consideration is not conclusive since no experimental check of this calculation has been performed so far. Nevertheless if the calculations are correct ^{130}Te is favored.

Taking into account the previous considerations we can conclude that ^{130}Te is an excellent candidate for DBD0ν research with a bolometric technique.

3.1.2 The choice of the energy absorber: why TeO_2 ?

Once it was decided to use ^{130}Te as a 0νDBD source, the Milano groupstarted to use TeO_2 crystals as energy absorbers. The choice of using TeO_2 crystals instead of pure Te crystals was determined by the useful properties of the first ones:

- **Debye temperature:** the Θ_D of TeO_2 is higher than that of pure Te and so, at the same temperature, the TeO_2 crystals have a lower specific heat and thus higher pulses can be achieved [115]. Furthermore, TeO_2 being a dielectric and diamagnetic material has smaller contributions to heat capacity.

- **Mechanical properties:** pure Te has poor mechanical properties and they break after a few thermal cycles. On the contrary, using TeO_2, large single crystals with excellent mechanical properties can be grown.

- **Compound quality and mass:** Te dominates the TeO_2 with respect to the mass (about 80%) permitting to work with large quantity of tellurium. The radiopurity of the obtained crystals is high ($<$ 1 pg/g in ^{232}Th and ^{238}U). Fig. 3.1 shows an example of a TeO_2 crystal of 5x5x5 cm^3 in size.

The Milano group has tested other compounds with different isotopic elements. This is the case of $^{48}CaF_2$, an excellent candidate due to the large transition energy of ^{48}Ca and good thermal properties of calcium fluoride crystals. Because of very low natural abundance of ^{48}Ca makes, on the other hand, this choice very expensive since it requires a strong enrichment. Other tested compounds are $^{100}MoPbO_4$, $^{116}CdWO_4$ and $^{150}NdF_2$. The first, despite the good thermal response, has the problem of an excessive counting rate due to the presence of ^{210}Pb. $^{116}CdWO_4$ is an excellent scintillator (this providing an additional tool for background suppression), but presents the same problem of low natural isotopic abundance as $^{48}CaF_2$. Recent tests on $^{150}NdF_2$ crystals showed a considerable difficulty to cool down to low temperatures these crystals.

Taking into account all these considerations we see that the isotope ^{130}Te in the form of TeO_2 crystals for DBD0ν research is the best presently available choice with moderate costs and good features for rare event research.

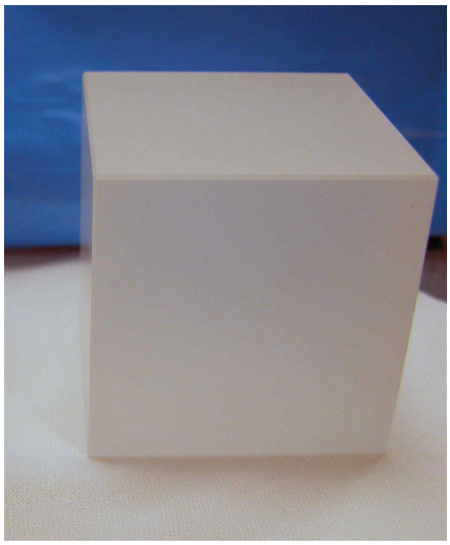

Figure 3.1: Example of 5x5x5 cm^3 TeO_2 crystal. The crystals are produced by Shanghai Institute of Ceramics (China).

3.2 The sensor

The Milano group decided to use as sensor NTD–Ge thermistors, working in the Variable Range Hopping (VRH) conduction regime with Coulomb gap as sensors. As described in section 2.4.2, this kind of thermistor can work as a perfect thermometer. It converts the thermal pulse into an electrical signal thanks to the temperature dependence of its resistivity. The resistance behavior follows the relation

$$R = R_0 \exp(T_0/T)^{\gamma} \tag{3.1}$$

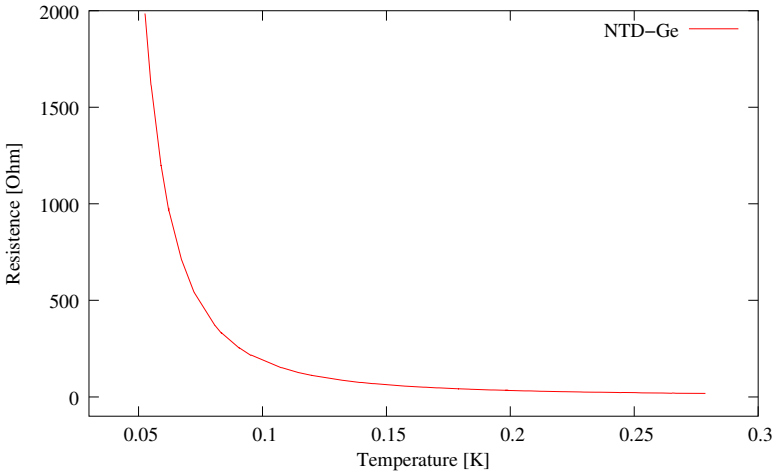

Figure 3.2: Resistance of a NTD-Ge thermistor of the Milano-Como group as a function of temperature.

where $\gamma = 0.5$ in the MIT region and at a working temperature lower than 1 K, and where the parameter R_0 depends on the sensor geometry as

$$R_0 = \frac{l}{S} \cdot \rho_0 \tag{3.2}$$

where l indicates the distance between the electrical contacts, S is the area of the pad where the contacts are made and ρ_0 is the electric resistivity that is described by eq. 3.1.

In sec. 2.4.2 the logarithmic sensitivity A was introduced. It depends on the neutron irradiation dose. For this reason each thermistor must be characterized at the operating temperatures, as described for Si thermistors by Alessandrello *et al.* [116]. For the NTD thermistors used by the Milano group (belonging to series #31 according to the Berkeley group classification), the T_0 value is around 3 K and thus the logarithmic sensitivity ranges between 7 and 10. A typical resistance vs. temperature curve, for these detectors, is reported in fig. 3.2.

These sensors are realized by neutron transmutation doping of ultra–pure Ge in a nuclear reactor to obtain the proper characteristics of both the resistance and variation of resistance with temperature.

Melt–doped Ge crystals cannot achieve the necessary uniformity due to a variety of dopant segregation effects. The only technique available for producing such uniform doping is NTD. In typical applications, the neutron absorption probability for a 3 mm thick wafer of Ge is small, on the order of 3 %, leading to a very homogeneous, uniform absorption process. The most important aspect is that ^{70}Ge transmutes into Ga, an acceptor, and that ^{74}Ge transmutes into As, a donor, the primary active dopant in NTD Ge. In this process, one places the Ge in a nuclear reactor where the following reactions take place:

$$\begin{aligned} {}^{70}Ge\ (21\%) + n &\rightarrow {}^{71}Ge\ (\sigma_T = 3.43 \pm 0.17b,\ \sigma_R = 1.5b) \\ {}^{71}Ge &\rightarrow {}^{71}Ga\ (t_{1/2} = 11.4day) \qquad Acceptor \end{aligned} \tag{3.3}$$

$$\begin{aligned} {}^{74}Ge\ (36\%) + n &\rightarrow {}^{75}Ge\ (\sigma_T = 0.51 \pm 0.08b,\ \sigma_R = 1.0 \pm 0.2b) \\ {}^{75}Ge &\rightarrow {}^{75}As\ (t_{1/2} = 83min) \qquad Donor \end{aligned} \tag{3.4}$$

$$\begin{aligned} {}^{76}Ge\ (7.4\%) + n &\rightarrow {}^{77}Ge\ (\sigma_T = 0.16 \pm 0.014b,\ \sigma_R = 2.0 \pm 0.35b) \\ {}^{77}Ge &\rightarrow {}^{77}Se\ (t_{1/2} = 38.8hr) \qquad DoubleDonor \end{aligned} \tag{3.5}$$

where σ_T and σ_R refer to the thermal and resonance neutron capture cross sections, respectively.

Since the doping level of the Ge needs to be on the order of 1×10^{17} atoms/cm^3, a very high flux reactor, such as that at the University of Missouri or the Massachusetts Institute of Technology, is necessary to do the doping in a reasonable time. Even more important characteristic is the stability in the flux and the stability in the neutron energy distribution as measured by the Cd ratio.

The significant quantity involved in thermistor performance is the net dopant concentration which is equal to the concentration of Ga atoms minus the concentration of As atoms minus twice the concentration of Se atoms. Unfortunately, to measure the thermal performance of the thermistor, one needs to wait for the decay of the activation product ^{71}Ge (11.4 day), approximately one year. Previous measurements carried out in the Gran Sasso Laboratory [117] have shown that the residual activity of the NTD thermistors become fully tolerable in an experiment with thermal detectors already a few months after irradiation. Following the radioactive decay period, the NTD germanium is first heat treated to repair the crystal structure then cut into $3\times3\times1$ mm^3 strips.

The values of R_0, T_0 and γ must be experimentally measured for each thermistor (characterization process). The measure of the characteristic R(T) for each thermistor is performed by thermally coupling the sensor to a low temperature heat sink using a high conductivity epoxy. The temperature T_B (base temperature) of the heat sink is then varied (15–50 mK) while a steady current I (bias current) flows trough the thermistors and a voltage drop $V = IR$ appears across them. This produces a power dissipation which raises the temperature and acts back on the resistance, until an equilibrium is reached. This phenomenon makes the $V - I$ relation deviate from linearity. This characteristic behavior of bolometers is often referred to as "electrothermal feedback". The static resistance is simply the ratio V/I while the dynamic resistance is the tangent at the $V - I$ curve. By further increasing the bias current the dynamic resistance crosses the so called *inversion point* (where it vanishes) and becomes then negative. For semiconductor thermistors, a typical $V - I$ curve, usually referred to as *load curve*, is represented in Fig.3.3 (a). By a combined fit to a set of load curves at different base temperatures, all the thermistor parameters are evaluated (see Fig.3.3 (b)).

3.3 The single module

The Single Module (SM) is the elementary unit of arrays of TeO_2 detectors and its behavior is independent from the one of the other detectors. The understending and control of the different parts of the SM and of the way they are assembled together is a fundamental task in successfully operating arrays of macro–bolometers. The fundamental components of the SM are: the absorber crystal of TeO_2 , the NTD thermistor, the heater, the PTFE supports and the copper structure (see Fig. 3.4).

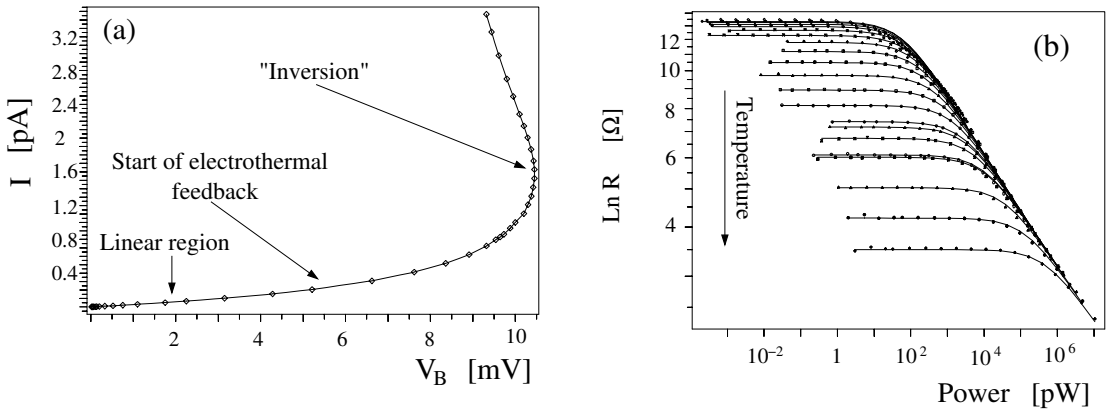

Figure 3.3: Typical load curve for a thermistor at T= 8 mK) (a) and resistance-power curves for a thermistor at different base temperatures (b).

The NTD germanium thermistors are glued to the TeO_2 crystal by 9 spots of Araldit rapid epoxy, of 0.4 to 0.7 mm deposited on the crystal surface by means of an array of pins. The height of each glue spot is 50 μm. This procedure was found to be reasonably reliable and reproducible in the MiDBD experiment [118, 62]. The heat conductance of the epoxy spots was measured in Milano and the phenomenological relation for its temperature dependence was found to be $\sim 2.6 \times 10^{-4}$ (T[K])^3 watts per degree kelvin per spot.

The materials used for the holding structure of the crystals are copper and PTFE; they can both be obtained with very low levels of radioactivity.

The crystal is held by means of PTFE supports that are connected to a copper frame. The copper frame is connected to the Mixing Chamber (MC) of a dilution refrigerator that provides the base low temperature ($\sim$10 mK) to operate the bolometers. Copper has a thermal conductivity and specific heat high enough to be an ideal heat bath, and it has excellent mechanical properties. On the other hand, the PTFE supports, having low heat conductance and low heat "leak" [119], guarantee a thermal conductance to the heat sink (copper frame) low enough to delay the re-cooling of the crystal, following a heat pulse, so that the pulse decay time (re-cooling time) is longer than the rise time structure, without big losses in the signal detection.

The crystals must be rigidly secured to the frame to prevent power dissipation by friction caused by unavoidable vibrations. These can prevent the crystal from reaching the required temperature and can produce low frequency noise. To prevent this effect the combined behavior of copper and PTFE is used: Copper guarantees a rigid structure without frictions between the different elements while PTFE provides an elastic but tight holding of the crystal, preventing the differential thermal contractions to break the crystals or to leave them too loose.

Heavily doped silicon chips with a resistance between 50 to 100 kΩ are also glued on to each crystal. They are used as Joule heaters to inject a uniform energy in the crystal in order to monitor the thermal gain and correct its variations off-line to stabilize the response of the bolometers. This topic will be discussed in more details later on (see sec. 4.1). The signal is read by means of two 50 μm diameter gold wires, ball bonded to metalized surfaces of the thermistor and thermally coupled to the crystals copper frames. This copper structure constitutes the heat sink, being in thermal contact with the coldest point of the dilution refrigerator (the mixing

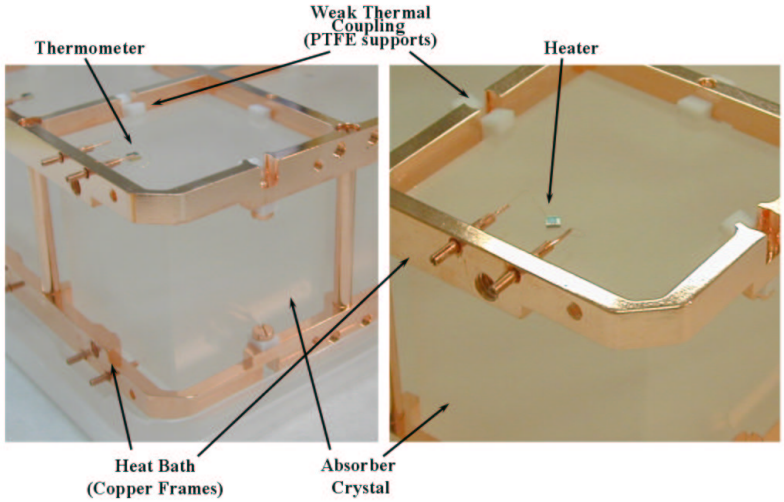

Figure 3.4: The single module used in the Cuoricino experiment: top view with a thermistor (left) and bottom view with an heater (right).

chamber).

3.4 Detector structure

The single detector module is inserted in a modular structure. The different structures used in the MiDBD and CUORICINO experiment, highlighting the contributions of the structures to detectors behavior.

3.4.1 MiDBD

The MiDBD experiment built up in 1997, consisted of a of 20 crystals of TeO_2 of $3\times3\times6$ cm^3 each (340 g), for a total mass of 6.8 kg. It was operated in the Hall A dilution refrigerator until December 2001. Sixteen MiDBD crystals were made of natural TeO_2. Of the remaining four, two were isotopically enriched at 82.3 % in ^{128}Te and the other two at 75.0 % in ^{130}Te.

The elementary module was the single module detector shown in Fig. (3.6) left. The PTFE supports were special masks that hold the upper and lower surface of each crystal. All the 20 single modules were arranged in a 5 planes tower-like structure, completely enclosed in a copper box. The detector tower was mounted inside the inner vacuum chamber (IVC) of the dilution refrigerator and thermally liked through a cold finger to the coldest point of the dilution refrigerator, at a temperature of about 10 mK.

The tower was shielded with an internal Roman lead layer of 1 cm minimum thickness (a special lead with 210Pb activity < 4 mBq/kg [111]). Additional layers of 10 cm Roman lead were placed above and below the tower, in order to shield the detectors against the unavoidable radioactive contaminations due to some fundamental components of the cryogenic system. A scheme of the MiDBD setup is shown in Fig. (3.5)a.

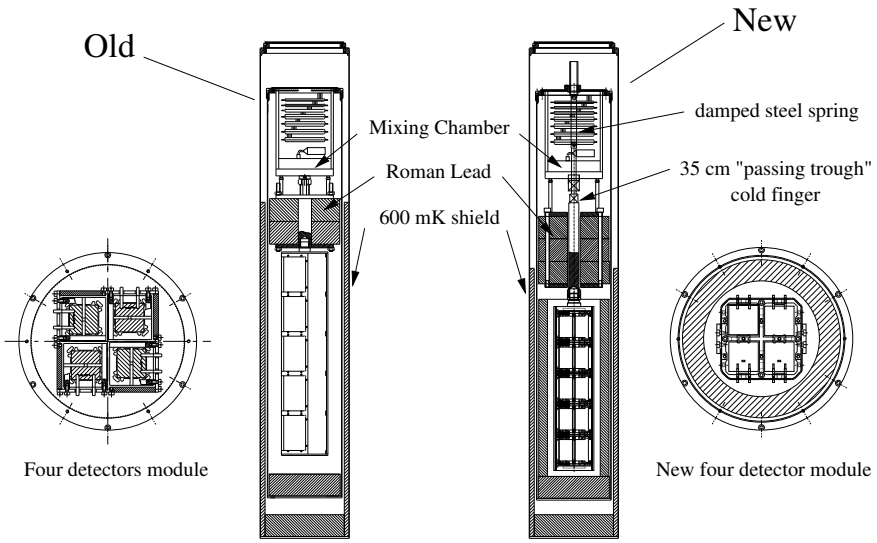

Figure 3.5: Scheme of the MiDBD detectors: first run (a), second run (b).

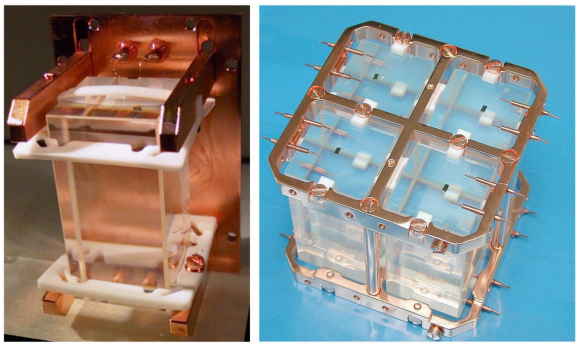

Figure 3.6: One detector module of MiDBD-I (left) and 4 detectors module of MiDBD-II (right).

The R&D effort devoted to improve both identification and reduction of the background sources and the performance of the new detector mounting system proposed for CUORICINO and CUORE, led in 2001 to a second run (MiDBD-II) in which the copper structure elements were subject to extra etching processes aiming the reduction of radioactive contaminants. As can be seen in Fig. (3.6) (right) each PTFE mask was substituted by 4 small pieces keeping the crystal in the right position. The amount of teflon used in every single detector module was reduced and a new more compact 4 crystal module assembling of the crystals had been adopted. This allowed the addition of an internal Roman lead shield of 2 cm minimum thickness and of a layer of 5 cm above the tower. The MiDBD-II tower was hanged to a spring suspension system to reduce mechanical vibrations. A scheme of the detector setup is shown in Fig. (3.5) left.

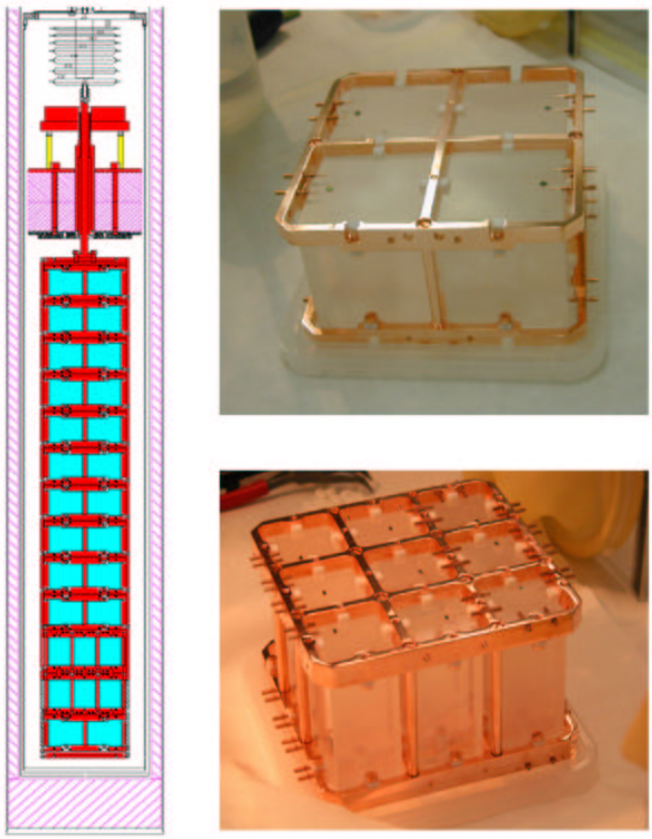

Figure 3.7: The CUORICINO detector: scheme of the tower and internal roman lead shields (left), the 4 crystal module (top right) and the 9 crystal module (bottom right).

3.4.2 CUORICINO

The CUORICINO detector is a tower-like structure made of eleven planes of 4-crystal modules (5x5x5 cm^3 crystals) and two additional planes of 9-crystal modules (3x3x6 cm^3 crystals)(see Fig. 3.7). The 18 small crystals were taken from the MiDBD experiment. CUORICINO contains therefore 44 TeO_2 crystals of 790 g mass and 18 TeO_2 crystals of 330 g mass. The total TeO_2 mass in CUORICINO is 40.7 kg. All the crystals, except the 4 isotopically enriched crystals previously used in MiDBD, are made of natural tellurium.

The structure of the 4 detectors module was designed scaling the MiDBD–II design to the dimensions of the ne crystals. Nevertheless the design of the PTFE pieces came out to be a source of irreproducibility of the MiDBD–II. The thermal contractions of PTFE work in opposite directions of their elastic contractions. For this reason detectors could be more sensitive to the vibrational noise, since crystals could get loose at low temperatures. A new design of the PTFE pieces has been developed. In fig. 3.8 pictures of new and old PTFE pieces are reported. The important change is the modification of the PTFE supports so that their thermal contractions increase the pressure on the crystal with decreasing temperature. As can be seen in Fig. 3.9 in the CUORICINO design the bigger contraction of the PTFE is in the vertical di-

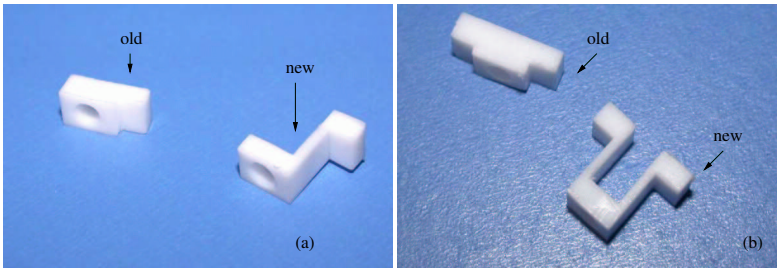

Figure 3.8: Comparison of new and old PTFE pieces that hold TeO_2 crystals.

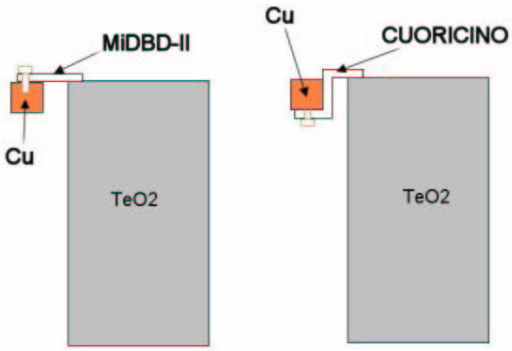

Figure 3.9: Comparison between the holding method of old (a) and new (B) PTFE pieces.

rection. This crystal holding method was tested in Hall A after the dismounting of the MiDBD experiment.This test was performed forcing the contribution of vibrations (i.e. without the anti–vibrating method) in order to test if this new method permits a lower mutual influence among crystals in the same CUORICINO module. Two CUORICINO modules were tested, one with old PTFE supports and the second one with new supports. The module containing new type PTFE pieces was cooler by several mK than the other one. This effect was due to the fact that the new PTFE design did not allow the crystal to vibrate independently from the holder. This free vibrations generates heat dissipations via scratching. Therefore it was decided to use the new PTFE supports in the CUORICINO array.

3.5 Cryogenic setups

Bolometric detectors, as described in chapter 2, require a low working temperature. For this reason all the performed TeO_2 experiments and the R&D activities needed a cryogenic setup, able to reach temperatures around 10 mK.

Two cryogenic setups were installed in the '80 at the Gran Sasso National Laboratory (LNGS) by the Milano group. The first, used in the past for the MiDBD experiment (Hall A) is now hosting the CUORICINO detector. The second (Hall C) has been dedicated to the research and development activities for CUORICINO and CUORE.

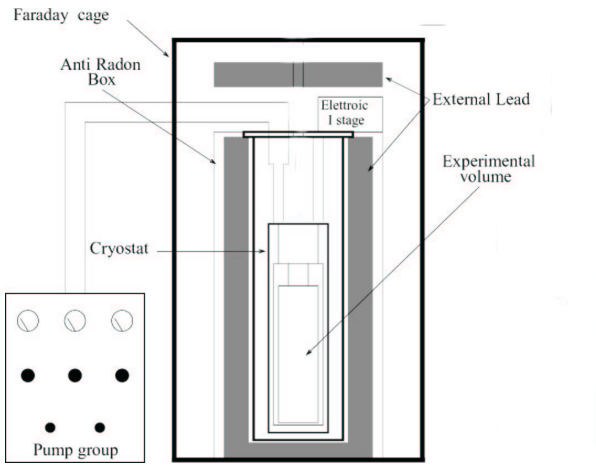

Figure 3.10: Scheme of the cryogenic setup.

The two existing cryogenic setups consist of dilution refrigerators having powers of 1000 μW (hall A cryostat) and 200 μW at 100 mK (hall C cryostat). They are both housed inside Faraday cages to suppress electromagnetic interference (see Fig. (3.10)). The experimental volume at base temperature is available in the Hall A cryogenic setup is about 16 cubic decimeters while in the Hall C setup is less than a third.

All the materials used for construction of MiDBD and CUORICINO were analyzed to determine their radioactive contamination levels. These measurements were carried out by means of two large Ge detectors installed in the Gran Sasso underground Low Radioactivity Laboratory. The level of the radon contamination in the air of the Laboratory is continuously monitored. Both dilution refrigerators are equipped with heavy shields against environmental radioactivity. In particular, the Hall A dilution refrigerator is shielded with two layers of lead of 10 cm minimum thickness each. The outer layer is made of commercial low radioactivity lead, while the internal one is made with special lead with a ^{210}Pb contamination of 16 $\pm$ 4 Bq/kg. The external lead shields are surrounded by an air-tight box flushed with fresh nitrogen from a dedicated evaporator to avoid radon contamination of the gas close to the cryostat. In order to shield the detectors against the unavoidable radioactive contamination from some fundamental components of the dilution refrigerator thick layers of Roman lead are placed inside the cryostat just around the detectors. A borated polyethylene neutron shield (10 cm) was added in 2001 to the hall A cryostat.

3.6 Electronics and DAQ

The electrical read-out configuration of a bolometric system is shown in Fig. (3.11). The main stages of the system are:

- **Detector biasing:** the thermistor is symmetrically polarized by means of 2 load resistors R_L. In this way a differential signal is read, thus avoiding common noise. The value of R_L must be greater than the thermistor impedance at the working temperature in order to have constant current bias and high signals. At $T \simeq 10\,mK$ the thermistors behave like a

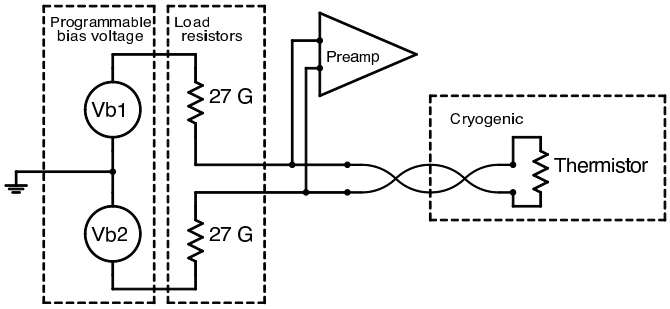

Figure 3.11: Scheme of the electronic setup.

resistance of the order of $1 \div 100$ MΩ; the load resistors are then chosen with values of the order of GΩ. The Johnson noise for these high resistance values is no longer negligible and has an rms value of about 300 eV for load resistors working at 300 K.

- **First differential stage:** it consists of a first differential preamplifier with gain G = 218 (which contributes to the reduction of the common noise), an antialising Bessel filter (that cuts frequencies above 12 Hz) and a programmable gain stage. This first stage can operate at room temperature, as in Fig.((3.11)), or cooled down to 120 K. The cold electronics has the purpose of reducing the series and parallel preamplifier noise, which in fact decreases with temperature, and on the other hand, to reduce microphonic noise, a noise source quite important for low energy signals, as for instance for Dark Matter searches.
- **Second stage:** an additional amplifier stage is set before the signal is transmitted to the ADC.

After the second stage the signal is sent simultaneously to the Analog to Digital Converter (ADC) and to the trigger that commands the ADC. If the pulse amplitude is higher than the trigger threshold (that is independently set for each detector) the signal is digitalized and transmitted to a PC-VXI that works as a memory of the system and makes a pre-analysis, thus permitting to check in real time the measure state. The ADC parameters depend on the pulse characteristic, but usually a voltage range of 0 - 10 V and 16 bits are used, thus meaning a resolution in the amplitude sampling of 0.15 mV. In Mi-DBD the sample time was 2 ms with a total number of pulses of 1024, while for CUORICINO the signal is sampled every 8 sec for a 512 total samplings.

3.6.1 Extrinsic noise

The electronic read-out, as it has been just described, introduces sources of extrinsic noise:

- **Johnson noise:** As previously said, for GΩ load resistors this noise source has a value around 300 eV, not negligible for experimental resolutions in the range $1 \div 8$ keV FWHM. This source of noise can be reduced by working with load resistors at low temperature, since the noise power spectrum is proportional to the temperature.
- **Preamplifier noise:** The noise associated to the preamplifier stage is of three types: *series* due to the JFET resistance having a value around 9 eV, *series 1/f* that amounts to 15 eV,

and the *parallel shot noise*, that for a room working temperature is around 130 eV rms. The usual experimental resolutions for energies close to the DBD0ν signal energy are of $\sim$7keV FWHM, thus meaning that these noise sources do not affect so much the actual value. At low energies, where the resolution is of the order of 1 keV FWHM they are no longer negligible.

- **Microphonic noise:** It is due to the variation of the static electric charge of the read-out wires and it can be reduced if working with a low temperature first differential stage, which allows shorter wires. It contributes with high frequency components and can worsen the low energy threshold.

Other source of extrinsic noise is the electromagnetic radiation, leading to spike signals and fast variations of the detector working point.

The most dangerous sources of noise appear because of thermodinamic fluctuations of the system and heat power arising from mechanical vibrations. These sources have low frequencies that can be partially corrected via a hardware stabilization system (introduced in the second run of CUORICINO) and/or an off-line stabilization procedure.

3.7 Off-line analysis

The main goal of the off-line analysis is the extraction of the relevant physics informations from the large amount of raw data recorded by the DAQ system. This analysis consists of two levels.The first one is the raw detector pulse analysis (e.g. amplitude evaluation, noise rejection, gain instability and linearity correction) aiming the production of reliable n^{th}-plas (a proper number of parameters fully describing each bolometric pulse). and energy spectra. The second-level is a multi-dimensional analysis aiming at obtain the sought physics results (e.g. $\beta\beta(0\nu)$ or DM interactions). The identification of the various background sources is also an important goal of the second-level analysis, and is the main topic of this PHD thesis work. This chapter will be devoted to the first level analysis, leaving for chapter 5 a detailed description of the second level analysis.

3.7.1 First-level analysis

As described in a previous section, when the output voltage of a given detector exceeds the trigger threshold, the acquisition system records a number of converted signal samples. The acquired time window ($\sim$few sec) must contain the entire pulse development in order to allow an accurate description of its waveform. The existence of a pre-trigger interval just prior to the production of the pulse ("baseline") guarantees that a small fraction of the number of acquired samples can be used to measure the DC level of the detector (which is directly connected with the detector temperature).

The fact that for each triggered pulse an entire waveform is sampled and recorded gives us a lot of information, as it will be shown in this section.

The following are the important goals for the (first-level or *pulse*) analysis (FLA):

1. maximization of the signal to noise ratio for the best estimate of the pulse amplitude. This is accomplished by means of the optimum filter (OF) technique [120];

2. correction of the effects of system instabilities that can change the response function of the detectors (gain "stabilization");

3. rejection of the spurious triggered pulses by means of pulse shape analysis;

4. identification and rejection of radioactive background pulses by means of coincidence analysis.

The Optimum filter

The OF technique is frequently used with bolometers to evaluate the amplitude of a signal with a superimposed stochastic noise. This algorithm has proven to provide the best estimate of the pulse amplitude under general conditions. Relative to a simple *maximum–minimum* algorithm, this technique allows the evaluation of the signal amplitude with much higher efficiency resulting in an effective improvement of the detector energy resolution. The following information is needed to implement the OF technique: the detector response function (i.e. the shape of the expected signal in the condition of zero noise) $S(\omega)$ and the noise power spectrum $N(\omega)$. Once these are known, the OF transfer function is easily obtained and used as a digital filter for the acquired pulses. The role of the OF transfer function is to weight the frequency components of the signal in order to suppress those frequencies that are highly influenced by noise and has the expression:

$$H(\omega) \; = \; K\frac{S^*(\omega)}{N(\omega)}e^{-i\omega t_M} \tag{3.6}$$

where K is an arbitrary constant and t_M the time at which the filtered signal is maximum. The amplitude of the pulse is then evaluated by integrating eq. (3.6) or evaluating the amplitude of optimally filtered pulses in the time domain. filtered pulses.

The noise power spectrum $N(\omega)$ is usually obtained from a hundred of baseline signals randomly acquired before every measurement by averaging the square of the module of their discrete Fourier transforms. The shape of of the detector response function is evaluated by averaging over a large number of acquired pulses, accurately selected so than to reject spurious signals.

The nuple construction

In processing the data off-line, the following parameters are evaluated and recorded to disk for each digitized pulse (*n-ple*):

1. the *channel number* i.e., the number of ADC channel that exceeded the trigger threshold;

2. the *absolute time* at which the pulse occurred with a precision of 0.1 msec;

3. the *OF amplitude* i.e. the amplitude of the optimally filtered signals

4. the *baseline*, obtained by averaging a proper number of samples from the pre-trigger interval. Since the detectors are DC coupled, it provides a direct measurement of the detector temperature at the creation of the signal;

5. the signal *rise* and *decay times*;

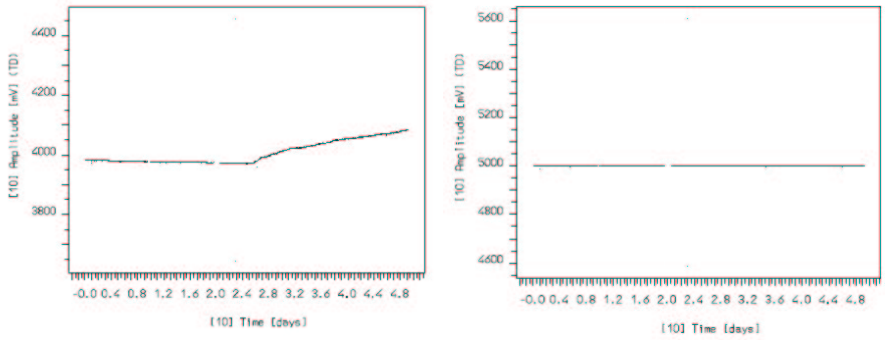

Figure 3.12: Heater amplitude vs baseline before (a) and after (b) the stabilization procedure.

6. the *pulse shape parameters*, obtained by comparing the acquired pulse with the expected response function of the bolometer after OF or adaptive filters. A further powerful technique is based on the use of artificial neural networks (ANN);

7. the *pile-up fraction*. The Wiener-filter algorithm is implemented [121] in order to recognize and successively reject double events. When two signals are found to occur in the same acquisition temporal window their amplitudes and their temporal distance are evaluated. These two parameters are very important in order to study the coincidence events due to radioactive cascades.

Instability correction

The next First Level Analysis step is the gain instability correction. The OF amplitudes are corrected to reduce or cancel the effects of system instabilities responsible for the variation of the ratio between the energy E deposited into a given crystal and the amplitude Δ V of the corresponding electrical pulse. These variations induce a worsening of the detector energy resolutions since signals referring to the same energy released in the crystal lead to different detector responses, thus broadening the correspondent peak in the energy spectrum.

According to our very naive detector model there are three instabilities that can modify the ratio Δ V/E (where V=V_b*G is the output voltage given by the product of the bolometer voltage V_b and the electronics gain G):

- a variation in the electronic gain G;
- a variation in the bias V_{Tot};
- a variation in the temperature T_b of the crystal.

The electronic system is designed to guarantee a stability of G and V_{Tot} within 0.1% . It is however, much more difficult to maintain stability within 0.1% of the detector temperature on long time scales. At a temperature of 10 mK this would require maintaining the temperature of all the crystals to an accuracy of 2 μ K for a period of several days. Usually thermal instabilities are correlated with intrinsic instabilities of the cryogenic set-up, mainly due to variations of liquid bath levels that determine small changes in the flow rate of the $^3He - ^4He$ mixture

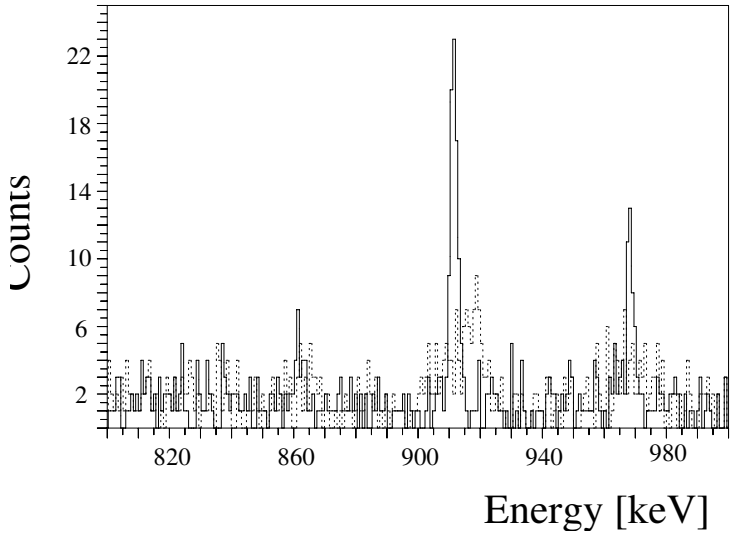

Figure 3.13: Comparison between a calibration spectrum before (dashed line) and after (continuous line) the stabilizzation procedure.

in the refrigerator. The problem can be minimized by directly stabilizing the main cryogenic parameters as much as possible, but often this is a difficult task and not completely solving the problem.

To overcome this problem, and as already mentioned in previous sections, a silicon resistor glued to each crystal is used as a heater to produce a reference pulse in the detector. It is connected to a high precision programmable pulser that produces a fast voltage pulse every few minutes dissipating the same amount of energy (E_{ref}) into the crystal each time. These voltage pulses mimic pulses produced in the crystal by particle interactions and are used to measure the value of the ratio Δ V/E. Any variation of the amplitude of the reference pulse is due to variations of the ΔV/E ratio. The OF amplitude of the reference pulse is therefore used to measure, every few minutes, the actual value of Δ V/E while the baseline of the reference pulse provides the contemporary measurement of the value of T. A fit is then used to obtain the values of Δ V/E as a function of temperature. Therefore, in this step of the off-line analysis, the OF amplitude of each pulse is corrected according to the given value of Δ V/E(T[t]) for the detector temperature at which the pulse has been generated. The effectiveness of this technique has been proven in the MiDBD experiment, where a typical temperature fluctuation over a day ranged from a few tenths to $\sim$100 μK . After correction, these fluctuations were reduced to less than 1 μ K [122] (see Fig. 3.12 and Fig. 3.13).

Noise rejection

Pulse shape analysis is very useful in rejecting spurious signals produced by microphonics and electronic noise. A confidence level is determined for each pulse shape parameter and for the rise and decay time of each pulse. Signals falling within these intervals are defined as “true” (or physical) pulses, while signals having one or more of their parameters outside of the relevant interval are rejected as noise. While the efficiency in the identification of true pulses is equal to

one, not all the spurious pulses are rejected by the use of one pulse shape parameter. The use of more than one pulse shape parameter results in better reliability of the rejection technique.

Linearization

The linearization of the detector response is critically important for energy calibration. The final step in data processing is the conversion of the OF amplitudes into energy values. The naive bolometer model previously used assumes linearity; however, several parameters depend on the crystal temperature, rendering the corresponding equation non-linear. Accordingly, the relation between Δ V and E is periodically obtained by the use of radioactive calibration sources (two simmetric point-like sources of ^{238}U and ^{232}Th in MiDBD and two wire sources of ^{232}Th in CUORICINO). Couples of points $(\Delta V, E)$ are than measured for several gamma lines. The obtained data must then be fit, by means of a minimization procedure, to the thermal model previously described, but taking into consideration the fact that the bolometer resistance and the crystal heat capacity are temperature dependent. This will provide the calibration function of E as a function of ΔV, that will then be used to convert the OF amplitudes into energy values. An alternative fit procedure is based on a polynomial or a power law fit. The latter was found to give the best results in CUORICINO.

A problem we are always facing in linearizing the detector response concerns the alpha region calibration. The use of ^{238}U and ^{232}Th sources in fact limits the calibration points to values lower than 2615 keV line of ^{208}Tl . The extrapolation to higher energies doesn't give optimal linearization for the alpha lines observed in the background measurements. This implies further manipulation of the collected background spectra in order to calibrate the alpha region by means of the alpha lines due to natural radioactivity.

In the second RUN of CUORICINO a new ^{56}Co calibration source was introduced, in order to have gamma lines up to 3.4 MeV.

Multiple events analysis

The analysis of the multiplicity of the events permits both to reject events that left energy in more than one single crystal (they should be very unlikely DBD0ν events) and to study the background sources.

Events depositing their energy in more than one crystal can be usually ascribed to high energy gamma rays, whose probability of escaping to the rest of the array after the first interaction is small. These high energy photons can derive from environmental radioactivity or from contaminations within the structure of the array. Also high and intermediate energy neutrons have a significant probability of depositing energy in more than one crystal. Another source of multiple events can be surface contaminations of the crystals and of the materials directly facing the detectors. Alpha particles emitted near the material surfaces have in fact a not negligible probability of escaping and they can consequently hint a nearby detector.

In the final stage of off-line analysis these coincidence events can be identified by analyzing the various registered pulse parameters, as detector number, signal time, pulse energy, and pile-up parameters. Signals occurring almost at the same time in two or more faced detectors are in fact evaluated as coincident. By analyzing the energy released in the detectors and the number and position of the hinted crystals is possible to try to find out the source that originated such events.

While in MiDBD and CUORICINO only a little fraction of the detector surfaces are faced to other crystals, thus limiting the efficiency of the anticoincidence cut, the tightly closed structure of CUORE will guarantee a stronger reduction of the background.

Chapter 4

The CUORICINO experiment

In this chapter I will briefly present the CUORICINO experiment, describing the experimental setup and the operating techniques. Then I will present the most recent results on neutrinoless double beta decay (0νDBD). Finally, I will report what we have learned from CUORICINO about background and detectors behavior. This information, together with the detector modelling described in the previous chapters, is the starting point of my PhD work.

4.1 Experimental setup

As reported in sec. 3.4.2 CUORICINO (Fig. 3.7) is an array of 62 crystals of TeO_2 with a total active mass of 40.7 kg. These crystals are arranged in a tower-like structure made by eleven 4-crystal module planes (5x5x5 cm^3 crystals) and two additional 9-crystal module planes of (3x3x6 cm^3 crystals). The tower is located, as the MiDBD tower, inside the cryostat situated in the Hall A of LNGS.

4.1.1 The CUORICINO tower

The CUORICINO array was built during the second half of the year 2002. This experiment represents the first step of the bolometric technique to a large scale experiment (hundreds of kg in mass). The start of the CUORICINO experiment had a big echo in the Low Temperature Detector Conference in 2002 [105].

CUORICINO's 62 crystals are arranged in a tower made by 13 planes, 11 of them are filled with 4 cubes of 5 cm side while the other two with 9 crystals $3\times3\times6$ cm^3 each (see Fig 3.7). These latter 18 crystals came from the MiDBD detector. All crystals are made with natural tellurite, the four $3\times3\times6$ cm^3 crystals coming from MiDBD are enriched, two of which in ^{128}Te 82.3 % isotopic abundance and the other two in ^{130}Te with isotopic abundance of 75 %, respectively. The total mass of CUORICINO is 40.7 kg, that corresponds to a mass of ^{130}Te of $\sim$ 11 kg.

Particular care was devoted to the selection and cleaning of the materials used for the construction of the CUORICINO array. The crystals were grown from pre-tested low radioactivity materials by the Shangay Instituts of Ceramics in China and shipped to Italy where they were surface treated with specially selected low contamination powders. The mechanical structure of the array was made exclusively in OFHC copper and in teflon, both previously measured to

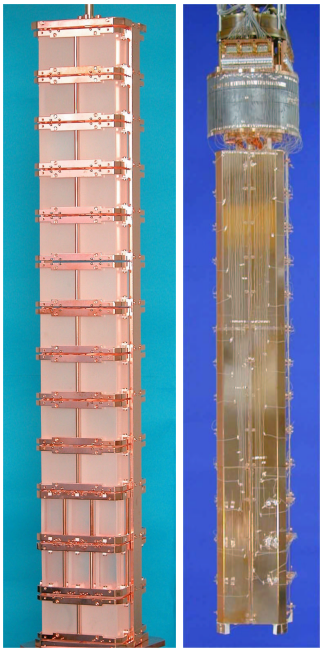

Figure 4.1: Spectrum of the sum of the two electron energies in the region of neutrinoless DBD

verify the extremely low radioactive content. All the copper and teflon parts of the mounting structure were separately treated with acids to remove any possible surface contamination. The array was assembled in an underground clean room in a N_2 atmosphere to avoid Rn contamination [123].

The tower is covered with copper plates and mounted in the same 1000 μW helium liquifier used for the MiDBD experiment. Due to the larger dimensions of the CUORICINO tower with respect to MiDBD, two of the cryostat thermal shields had to be replaced. To avoid external vibrations to reach the detectors the tower is mechanically decoupled from the cryostat through a steel spring.

In order to shield against the radioactive contaminants from the materials of the refrigerator, a 10 cm layer of Roman lead with ^{210}Pb activity of <4 mBq/kg [122] is inserted inside the cryostat, immediately above the CUORICINO tower. A 1.2 cm lateral layer of the same type of lead is framed around the array to reduce the activity of the thermal shields. The cryostat is externally shielded by means of two layers of lead of 10 cm minimal thickness each. While the outer is made by common lead, the inner one has a ^{210}Pb activity of 16 $\pm$ 4 Bq/kg. An additional layer of 2 cm of electrolytic copper is provided by the cryostat thermal shields. The background due to environmental neutrons is reduced by a layer of Borated Polyethylene of 10 cm minimum thickness. The refrigerator operates inside a Plexiglass anti-radon box flushed with clean N_2 and inside a Faraday cage to reduce electromagnetic interferences.

Thermal pulses are recorded by neutron transmutation doped Ge thermistors thermally coupled to each crystal. Stabilization is performed with voltage pulses across the usual heater resistors attached to each bolometer. The voltage pulses are generated with high stability pulse generators, designed and developed for this purpose [124]. These stabilizing signals are tagged

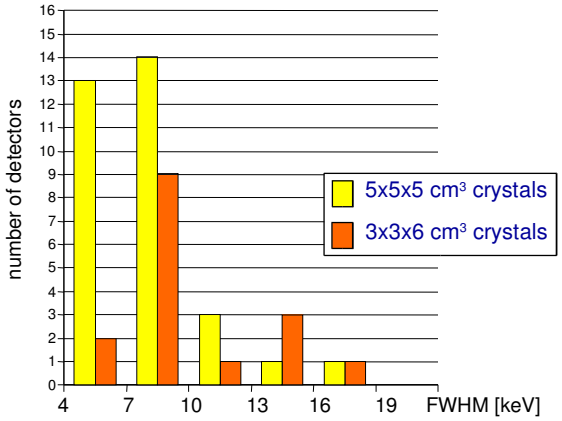

Figure 4.2: Distribution of energy resolutions (FWHM)for the single CUORICINO detectors at the ^{208}Tl 2615 keV line.

by the acquisition system. The detector's baseline is stabilized with a dedicated circuit with a precision better than 0.5 keV/day (on the average [125] between the successive refilling of liquid helium of the main reservoir).

CUORICINO is operated at a temperature of $\sim$8 mK with a spread of $\sim$1 mK. A routine energy calibration is performed before and after each subset of runs, which lasts about two weeks, by exposing the array to two thoriated tungsten wires inserted in immediate vicinity of the refrigerator. All runs for which the average difference between the peak position in the initial and final calibration is larger than the experimental error were discarded.

Data is processed off-line evaluating pulse amplitude (on the basis of an Optimum Filter (OF) algorithm), pulse offset (baseline = detector DC voltage = detector temperature), pulse shape parameters and other correlated information (rise and decay time, delay, second peak amplitude in the case of a pileup...). On the basis of the reference pulse (Si heater), OF evaluated amplitudes are corrected to account for detector response variation. Portions of measurement where this correction was not satisfactory were rejected. in the same way, portions of measurements where noise is too high (either when the energy resolution of the detector shows a sizable worsening and/or when a large fraction of the triggered signals are noise signals) are also rejected.

The calibration and energy linearization of the detectors is obtained by source calibration. Two different functions are used to fit the calibration data (i.e., peaks voltage positions vs gamma line energy): a cubic law and a power law. The first one is being used mainly for the gamma region, yielding very good results. The second one is used to extrapolate the calibration to the region above the 2615 keV peak (the highest peak observed in a source calibration) with results by far better than those obtained with the polynomial calibration. Finally, spurious noise triggered is rejected on the basis of the shape parameters evaluated for each triggered signal. Often happens that the pulse shape parameters are becoming ineffective in distinguishing particle pulses from noise signals below a certain energy. In this case a software threshold is applied to the analyzed channel to remove all the signals for which the energy is lower than this threshold.

4.1.2 Run I

Cuoricino was first cooled down at the beginning of 2003. During the first cool down, 12 of the 5×5×5 cm^3 and one of the 3×3×6 cm^3 crystals were "lost", due to disconnection at the level of thermalization stages (which allows the transmission of the electric signals from the detectors to room temperature [123]). We decided to go on with the measurement to test the performances of the detectors. Since the active mass was of ∼30 kg, and the energy resolution was excellent, data collection was continued for a few months before warming up the array. The total collected statistics was about 1.01 [kg of ^{130}Te]·y divided in 5 data sets (data taking periods between two calibrations). The first set was very noisy and was used mainly to optimize the detector (elimination of external noise sources, fixing of the electrical grounding problems, damping of vibration sources). Unfortunately, due to cryogenic problems the duty cycle of this run was very low, about 28%. At the end of 2003 we decided to warm up the cryostat to fix the problem of the 13 missing channels.

4.1.3 Run II

At the beginning of 2004 the cryostat was open and we made the needed reparations. The problems were almost fully solved and only for the 2 of the 13 detectors a reparation was impossible without dismounting a large part of the detector. The detector started again the data taking in May 2004. The collected statistic up to July 30 2005 is [4.86 kg of ^{130}Te]·y on 10 data sets. The, so called, Run II is still going on and no complete warming up is planned for the near future. In Run II most of the cryogenic problems were fixed and the duty cycle became ∼74%, which probably is the intrinsic upper limit for the present apparatus.

4.2 Results

The results presented here correspond to an effective exposure of 5.87 kg of ^{130}Te · year. The energy resolution for the complete data set was computed from the FWHM of the 2615 keV background gamma ray line from the ^{232}Th chain. The results are 7.5 ± 2.9 keV for the 5×5×5 cm^3 crystals, and 9.6 ± 2.5 keV for the 3×3×6 cm^3 crystals. The sum of the spectra of the 5×5×5 cm^3 and 3×3×6 cm^3 crystals in the region of the neutrinoless DBD is shown in Fig. 4.3. One can clearly see the peaks at 2447 and 2615 keV from the decays of ^{214}Bi and ^{208}Tl, and a small peak at 2505 keV due to the sum of the two γ lines of ^{60}Co (1332 + 1173 keV). The background at the energy of neutrinoless DBD (i.e. 2475-2580 keV) is of 0.18 ± 0.02 counts/kg/keV/y. This result is obtained assuming a flat background and adding the fit of the 2505 keV peak. We use as response function a sum of n gaussian each with the characteristic FWHM resolution at 2615 keV of the n^{th} detector. No evidence is found at the energy expected for neutrinoless DBD of ^{130}Te . By applying a maximum likelihood procedure [126, 127] we obtain a 90% C.L. lower limit of 2.0 $\times 10^{24}$ years on the half-lifetime for 0νDBD of this nucleus. The unified approach of G.I.Feldam and R.D.Cousins [128, 129] leads to a similar result. Presently, the best fit yields a negative effect for the 0νDBD peak. There is 5% variation of the limit when changing the energy region, the background shape (linear or flat) and when including or excluding the 2615 keV peak in the fit.

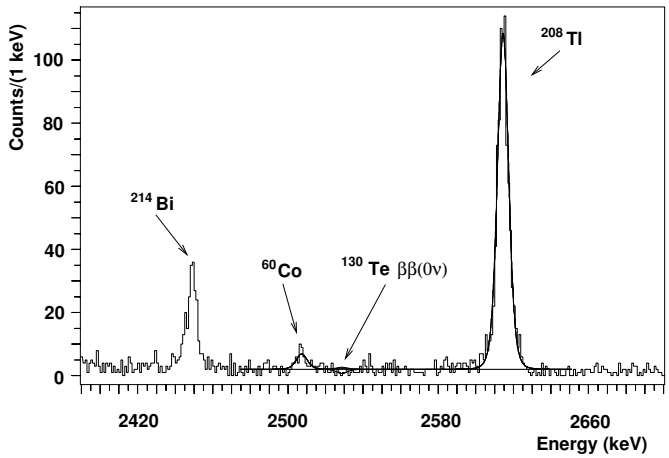

Figure 4.3: Spectrum of the sum of the two electron energies in the region of neutrinoless DBD

4.2.1 Limits on Majorana mass

The upper bounds on the effective neutrino mass that can be extracted from our result depend strongly on the values adopted for the nuclear matrix elements, as reported in sec. 1.2. In Tab. 1.2.1 different values for F_N are reported the limits, obtained with the different nuclear matrix calculations (apart from those based on the shell model which are not considered as valid for heavy nuclei [46]). We have also not considered at the moment the calculation by Rodin et al. [49] since, in the case of ^{130}Te , they are based on the not yet established value for the two neutrino DBD lifetime. In particular, the adopted value of 2.7 $\times 10^{21}$ years [130] is the largest among all geochemical ones [16, 80, 92]. The evaluation based on single beta decay, which could be preferable [92, 131] is not available for ^{130}Te. The rates for two neutrino DBD of this nucleus based on geochemical experiments are however uncertain [16, 92]. We have therefore adopted those based on a direct experiment [62]. Taking into account the above mentioned uncertainties, our lower limit leads to a constraint on the effective neutrino mass ranging from 0.26 to 1.4 eV which partially covers the mass span of 0.1 to 0.9 eV indicated by H.V. Klapdor-Kleingrothaus et.al. [132].

4.2.2 CUORICINO Sensitivity

The expected three years of sensitivity for CUORICINO (present configuration) is $1 \cdot 10^{25}$ years, corresponding to a sensitivity for the Majorana mass between 0.1 and 0.45 eV.

4.3 CUORICINO Background Analysis

This is one of the most important topic in the view of CUORE. The most important R&D activity of the CUORE collaboration is the background reduction program that was also a part of my PhD work. The motivation and strategies of this activity will be described in the next two chapters. It is clear anyway that to perform this background reduction activity one must know which are the sources of background and how relevant they are.

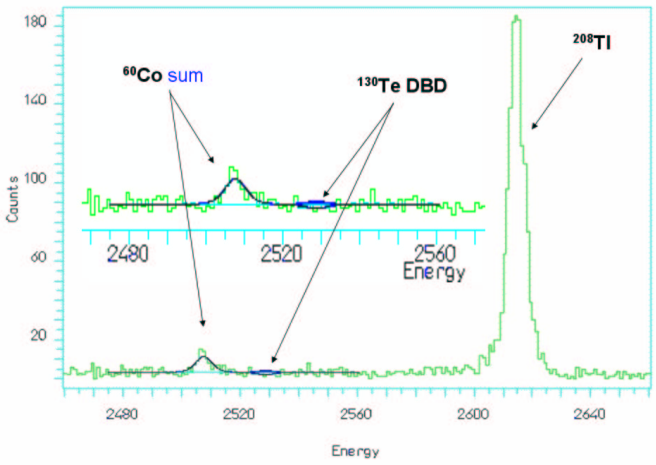

Figure 4.4: Spectrum of the sum of the two electron energies in the region of neutrinoless DBD

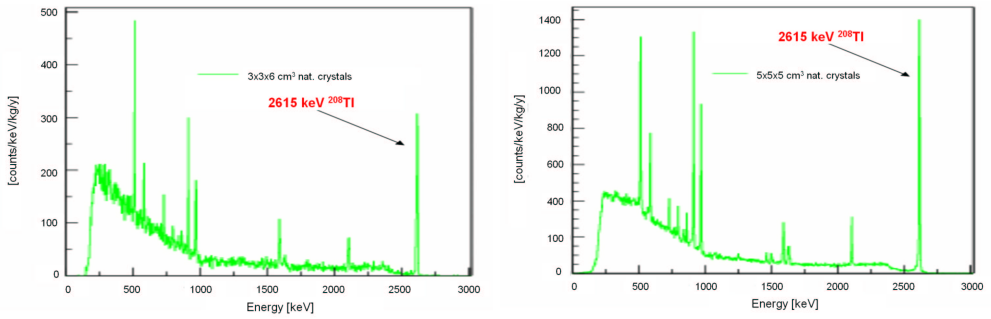

Figure 4.5: Summed calibration spectrum (^{232}Th source just outside the crysotat) from all the operating $5\times5\times5$ cm^3 and $3\times3\times6$ cm^3 crystals.

4.3.1 Background Measurements

In Fig. 4.6 the background spectra for the $5\times5\times5$ cm^3 and $3\times3\times6$ cm^3 crystals are shown. The gamma lines due to ^{60}Co, ^{40}K and of the ^{238}U and ^{232}Th chains are clearly visible.

These lines, due to contamination of the experimental apparatus and setup, are not visible in the spectrum of single detectors since there the statistic is too low. They appear after summing the different detectors, and are a good check of the calibration and stability of the detectors during the background measurement. In the spectrum one can recognize also the gamma lines due to Te activation (^{121}Te, ^{121m}Te, ^{123m}Te, ^{125m}Te and ^{127m}Te) and those due to Cu activation (^{57}Co, ^{58}Co, ^{60}Co and ^{54}Mn) by cosmic ray neutrons while above ground.

The FWHM resolution of $5\times5\times5$ cm^3 detectors at low energy, as evaluated on the 122 keV gamma line of ^{57}Co, is $\sim$2.8 keV. The ^{208}Tl gamma line at 2615 keV - clearly visible in the background sum spectrum - is used to evaluate the energy resolution in the region of double beta decay; the FWHM is 7 keV.

The $3\times3\times6$ cm^3 and $5\times5\times5$ cm^3 crystal background spectra (sum of all the anticoincidence

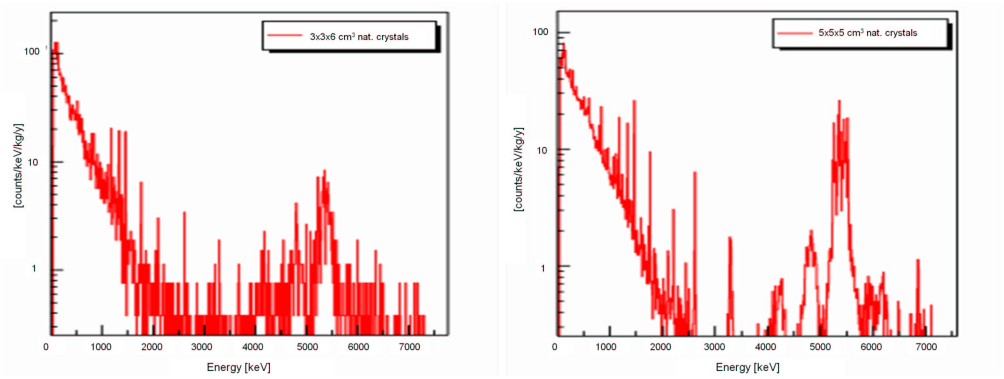

Figure 4.6: Summed background spectra from the operating $5\times5\times5$ cm^3 and (natural abundance) $3\times3\times6$ cm^3 crystals.

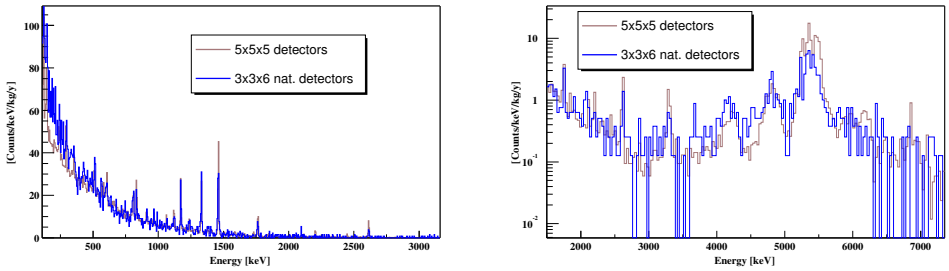

Figure 4.7: Comparison between the background of the $5\times5\times5$ cm^3 crystals and that of the natural $3\times3\times6$ cm^3 crystals in the gamma region (left) and in the alpha region.

spectra of the detectors) are compared in Fig. 4.7.

The FWHM resolution at low energy, measured on the 122 keV gamma line of ^{57}Co, is $\sim$1.5 keV. The FWHM resolution on the ^{208}Tl gamma line at 2615 keV is evaluated to be of about 12 keV.

4.3.2 Background analysis

Many studies have been performed on the background analysis of CUORICINO [133]. Here the most important results are briefly summarized.

A complete background analysis is still on the way and will include the study of background differences among the detectors (now that the statistics on the single detector is high enough) and a comparison with MC simulations in an effort of identifying the different background sources. Some preliminary comments are however of relevance:

- Some data sets show the presence of a Rn contamination as it is clearly evident from the increased background counting rate on both continuum and ^{214}Bi peaks. The reason for this contamination is still not clear whether being due to a failure of the anti-radon box or to some other reason. Of course this is not a problem for 0nDBD search while it is for

2nDBD studies.

- A study of the distribution of the counting rates in the gamma region for the 13 Cuoricino planes showed an excess on both continuum and ^{214}Bi , ^{40}K , ^{60}Co peaks for the bottom plane.On the contrary, the 2615 peak seems to have almost the same intensity on all the planes.
- A study of the counting rates of the 13 planes in the region of the Tl peak (2615 keV) and of the ^{210}Pb peaks (5.3 and 5.4 MeV) showed a correlation of the former with the counting rate in the neutrinoless DBD region while no correlation is observed for the latter.

In Fig. 4.7 a comparison between the background spectra of the large and small crystals is shown. General spectral shapes and counting rates (when normalized to the mass of the crystals) are quite similar. On the other hand the intensities of the gamma lines do not show a clear behavior: the ^{214}Bi 1764 keV (of the ^{238}U chain) and the ^{208}Tl 2615 keV lines (of the ^{232}Th chain) seem to scale with the efficiency of the detectors (according to the results of the MonteCarlo analysis, the ratio of the detection efficiency between the $5\times5\times5$ cm^3 and the $3\times3\times6$ cm^3 crystals is $\sim$3). The ^{40}K line at 1460 keV has the same intensity per unit mass for the two types of detectors. The ^{60}Co lines at 1173 and 1332 keV, on the contrary show a higher intensity per unit mass in small crystals. Moreover, they undergo a larger reduction by the anticoincidence cuts with respect to other γ–lines.

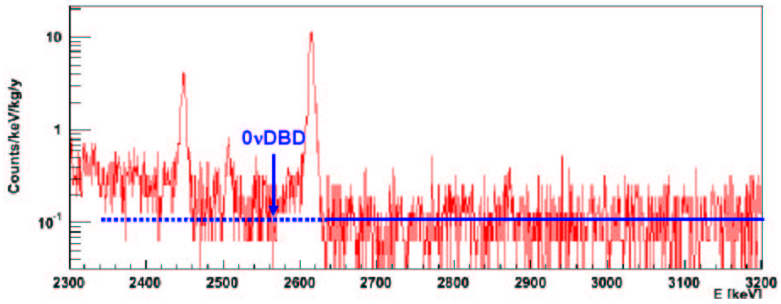

Figure 4.8: .

In Table 4.1 the counting rates in different energy regions are reported. It is clearly evident that an improvement was obtained in the 2-3 MeV region (a reduction of $\sim$30% in the counting rates per unit mass either of the small and of the large crystals) despite the reduced internal lead shield used in CUORICINO ($\sim$1.2 cm thickness of roman lead) with respect to MiDBD-II ($\sim$3 cm thickness of roman lead). An even better reduction was obtained in the 3-4 MeV region where background is mainly dominated by surface contamination contributions.

Our interest is obviously focused on the 0νDBD region. In this region, between the two γ lines at 2448 and 2615 keV (^{238}U and ^{232}Th chains respectively), we should have contributions from both degraded α's from surface contaminations and ^{208}Tl γ's from bulk contaminations. This can be done comparing the background with the one observed in the region just above the ^{208}Tl 2615 keV line, where background sources should be limited to surface contaminations.

By using a background model resulting from the MiDBD analysis, and taking into account that we changed both the detector structure and the internal set-up of the cryostat (the roman lead

counts/keV/kg/year	1-2 MeV	2-3 MeV	3-4 MeV	4-5 MeV
MiDBD-II	3.21±0.08	0.61±0.04	0.29±0.02	1.88±0.06
3×3×6 natural	4.60±0.06	0.38±0.04	0.24±0.03	0.78±0.05
5×5×5	4.33±0.02	0.41±0.03	0.17±0.02	0.55±0.03

Table 4.1: Counting rates per unit mass in MiDBD-II and in CUORICINO.

Table 4.2: Estimate of the relative contributions of the different sources responsible for the background measured in CUORICINO.

Source	^{208}Tl	$\beta\beta(0\nu)$ region	3-4 MeV region
TeO_2 ^{238}U and ^{232}Th surface contamination	-	10± 5%	20± 10%
Cu ^{238}U and ^{232}Th surface contamination	∼15%	50± 20%	80± 10%
^{232}Th contamination of cryostat Cu shields	∼85%	30± 10%	-

shield and the cryostat copper radiation shields) we evaluated its consistency for CUORICINO. Its results tend to identify the most important sources of the CUORICINO background, giving a quantitative guess of their relevance. The percentage result of the measured background in the DBD region, is summarized in table 4.2. It should be noticed that CUORICINO data seem to indicate a shallower depth for the crystal surface contaminations relative to MiDBD.

Analysis of the CUORICINO background above 3 MeV

The analysis is based on both the coincidence (not used in the previous analysis) and the anticoincidence spectra collected with 5×5×5 cm^3 detectors during the first run of CUORICINO and calibrated with a new, more reliable, technique in the alpha region. As mentioned above, the spectra have been calibrated and linearized in energy assuming a power law dependence for the pulse amplitude that yields better results in the alpha region. The anticoincidence sum spectrum of 5×5×5 cm^3 detectors calibrated in this way is compared in Fig. 4.9 with the analogous spectrum calibrated only with gama lines (assuming here a polynomial relationship between pulse amplitude and particle energy and extrapolating this calibration in the alpha region).

Alpha and beta particles produced by environmental radioactivity can give important contributions to the background above 3 MeV. Because of their low penetration range, these particles can only be located either in the crystals or on the surfaces of the materials directly facing the crystals: the copper holder or, less likely, small components placed near the crystals or on the crystal surface such as the NTD thermistor, the Si heater, their gold wires, the glue and other smaller parts. MonteCarlo simulations of the coincidence and anticoincidence sum spectra of 5×5×5 cm^3 detectors produced by radioactive contaminations of the above mentioned elements have been obtained using our GEANT4 based code. These spectra have been compared with the measured spectra in order to identify the actual contaminations responsible of the measured background.

As a first step, bulk and surface contaminations of the crystals have been considered. Both these contaminations give rise to peaks (centered at the transition energy of the decay) in the

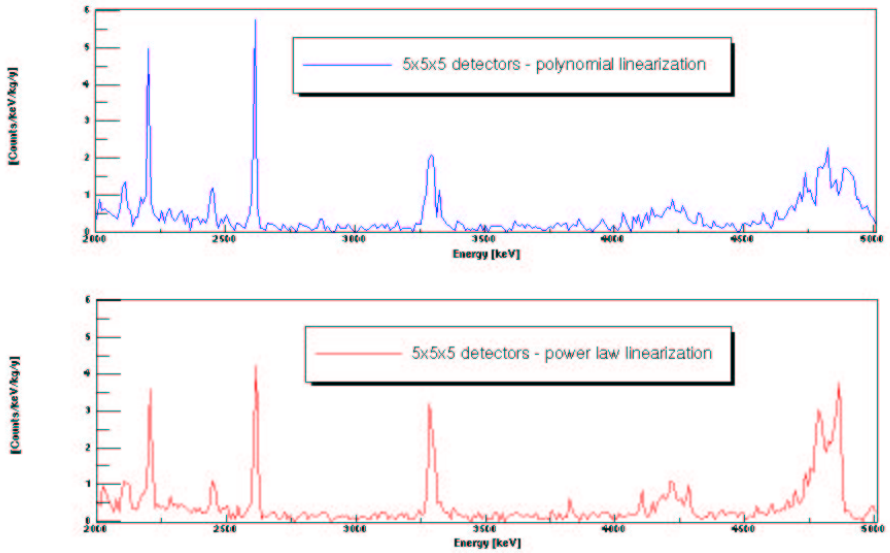

Figure 4.9: Comparison between spectra obtained with different linearization methods. The appearence of clear alpha structures with the *power law* metod is evident.

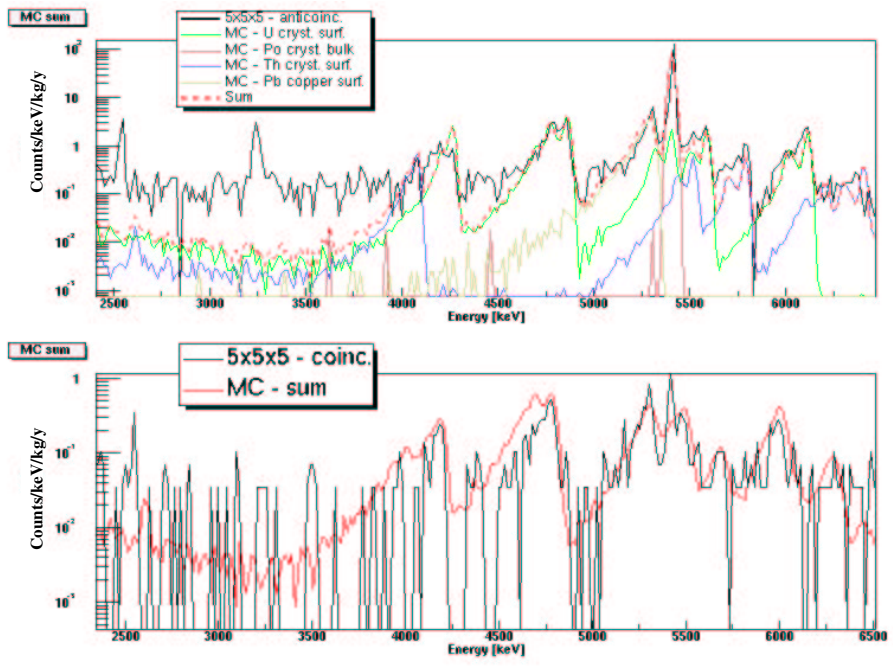

Figure 4.10: Comparison between MonteCarlo and CUORICINO anticoincidence (top) and coincidence (bottom) spectra in the case of the TeO_2 crystal surface contaminations ($\lambda \sim 1$ μm) specified in the figure.

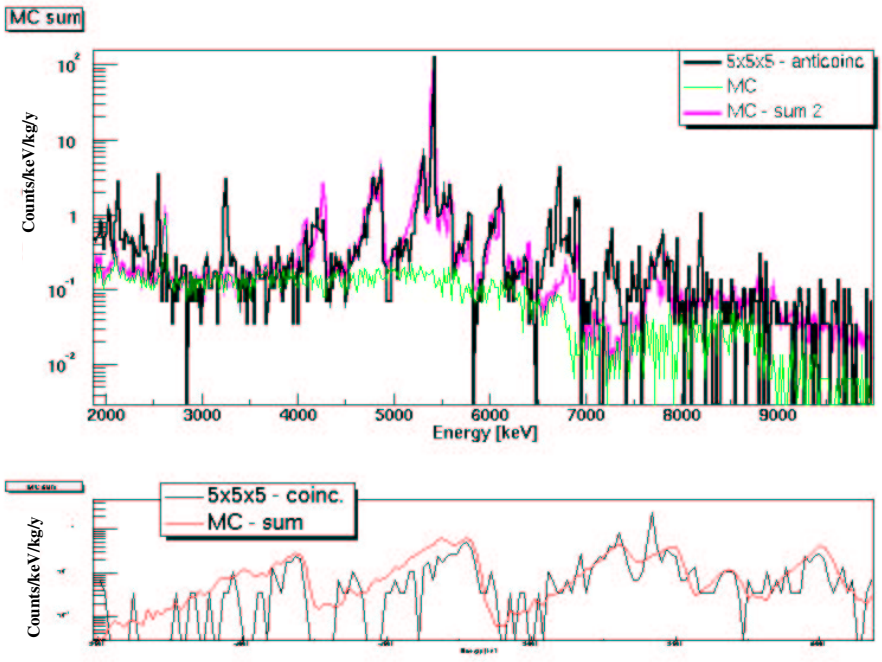

Figure 4.11: Comparison between Monte Carlo and CUORICINO anticoincidence (top) and coincidence (bottom) spectra when a Th surface contamination of the detector copper holder (green line) is added (pink line) to the crystal conatminations considered in fig. 4.10.

anticoincidence spectrum, but in the case of bulk contaminations these peaks are Gaussian and symmetric while in the case of surface contaminations the peaks show a low energy tail. On the contrary, the only possible sources contributing to the coincidence spectrum are the surface contaminations of the crystals. The general shape and the structures appearing in both background spectra strongly depend on the depth and density profile assumed for the contamination (an exponentially decreasing function characterized by a *depth* λ: $\rho(x) = Ae^{-\lambda x}$ yielded the best results). The results of the comparison between MonteCarlo simulations and measured spectra allow us to prove that the alpha peaks of the anticoincidence spectrum of CUORICINO are due to a surface (and not bulk) ^{232}Th and ^{238}U contamination of the crystals with the only exception of the ^{210}Po line which has to be attributed to a bulk contamination of the crystals. The shape of the peaks in the anticoincidence spectrum and the shape of the coincidence spectrum is fully accounted for when a surface contamination *depth* of the order of 1 μm or less is assumed. As shown in Fig. 4.10 the identified crystal contaminations yield a satisfactory explanation of the coincidence spectrum. Some contribution to the continuous part of the anticoincidence spectrum seems however still missing. In order to explain this continuum, a further source, not contributing to the coincidence spectrum, has to be considered. Such a source can be a ^{232}Th or ^{238}U contamination on the copper surface, as shown in Fig. 4.11. The *depth* of the contamination should be of the order of $\sim$5 μm (a deeper contamination would produce too high gamma peaks while a thinner contamination would give rise to a structure in the anticoincidence spectrum) with a total activity in the first 1.5 μm of the order of 10^{-9} g/g either in ^{238}U or ^{232}Th or both.

These results show that with a substantial reduction of the copper and TeO_2 crystal surface contamination levels the sensitivity goal for CUORE (i.e. a background counting rate of the order of 0.01 counts/keV/kg/y or better) can be reached.

Chapter 5

Developing detectors for the inverted hierarchy region: the CUORE project

As pointed out in Chapter 1, the next generation of experiments for 0νDBD search should be able to explore the inverted hierarchy mass region (see 1.5). From Fig. 1.4 this corresponds to a sensitivity in $\langle m_\nu \rangle$ better than $\sim$50 meV. In the case of ^{130}Te this came out to correspond to a sensitivity for the life time better than a few 10^{26} y.

The consistent improvements in cryogenic spectroscopy achieved by the MiDBD and CUORICINO experiments, presented in the previous chapters, show that we have available today a technology to achieve such a fundamental physics goal. This is the starting point from which the CUORE was developed.

In this chapter I will present an overview of the CUORE experiment with only some details about the main detector (for details see [134]). Finally, the experimental laboratory and setup are described.

5.1 CUORE project: a Cryogenic Underground Experiment for Rare Events

The CUORE detector will consist of an array of 988 TeO_2 bolometers arranged in a cylindrical configuration of 19 towers containing 52 crystals each (Fig. 5.1), for a total mass of $\sim$770 kg. Each of these towers is a CUORICINO-like detector consisting of 13 modules, 4 detectors each.

As described in Chapter 4, the excellent performance of the $5\times5\times5$ cm^3 crystals to be used in CUORE was already proved with CUORICINO [135, 136]. Reproducibility was tested with a dedicated measurement on the MiDBD type array, on 15 $3\times3\times6$ cm^3 detectors operating simultaneously. The results were satisfactory as shown with the load curves in Fig. 5.2. These results were confirmed for the $5\times5\times5$ cm^3 crystals in several other different tests with four-detector modules during the CUORICINO R&D program. The pulse amplitudes spanned an interval from 50 to 150 μV/MeV at $\sim$100 MΩ operation point, in agreement with the thermal model (see sec. 2.2). The full width at half maximum (FWHM) was $\sim$1 keV for low energy gamma peaks, and $\sim$5 to 10 keV at 2.6 MeV.

According to the original CUORICINO-like design each stack of thirteen 4-detector modules will be connected by two vertical copper bars. The development of a new design for the

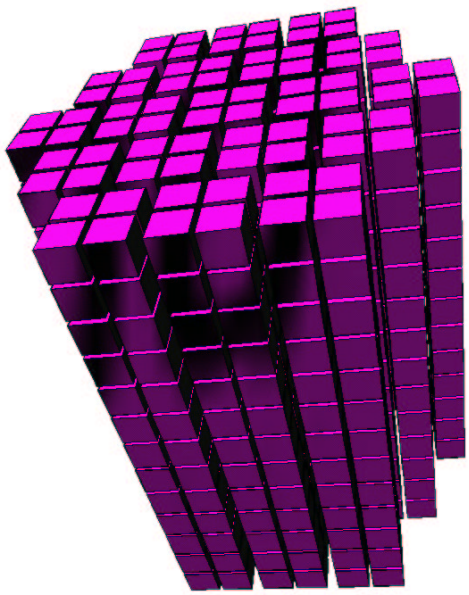

Figure 5.1: The CUORE detector (cylindrical-shaped) built of 19 CUORICINO-like tower.

CUORE detector setup is one of the goals of my PhD work and it will be described in detail in Chapter 9. The details of the towers wiring are also under development; however, the current choice is for 50 μm diameter twisted pairs of nylon coated constantane wire running along the vertical copper bars. On the top of each tower there will be 52 twisted pairs of wires for the thermistors and four for the heaters. Two more twisted pairs will be required for diagnostic thermometers, one on top and one on the bottom of the tower.

The CUORICINO detector, presently taking data at LNGS, is identical to one of the 52 future detector towers of CUORE with the exception of the two planes containing the $3\times3\times6$ cm^3 crystals discussed earlier. The 19 towers of CUORE will be suspended independently from a large cylindrical copper plate, thermally connected to the mixing chamber of the dilution refrigerator. In this manner, all the tests done on CUORICINO will be used as tests for the CUORE array. The array will be suspended from the mixing chamber by a vertical spring to decouple the detector from the vibrations of the dilution refrigerator. Some tests were done with the purpose of optimizing the suspension setup both in the Hall C R&D cryostat and in CUORICINO's cryostat. As a result, a pendulum-like suspension will be designed for the entire CUORE array.

The heavy shielding of CUORE will present non-trivial problems for the energy calibration with radioactive sources. The presently considered option is to use radioactive metal wires encapsulated in PTFE tubes. The tubes will be placed vertically between the towers, and free to slide along a fixed tube to the appropriate calibration point. A tight vacuum sliding seal will allow the part of the tube containing the wire to be inserted and extracted from the cryostat.

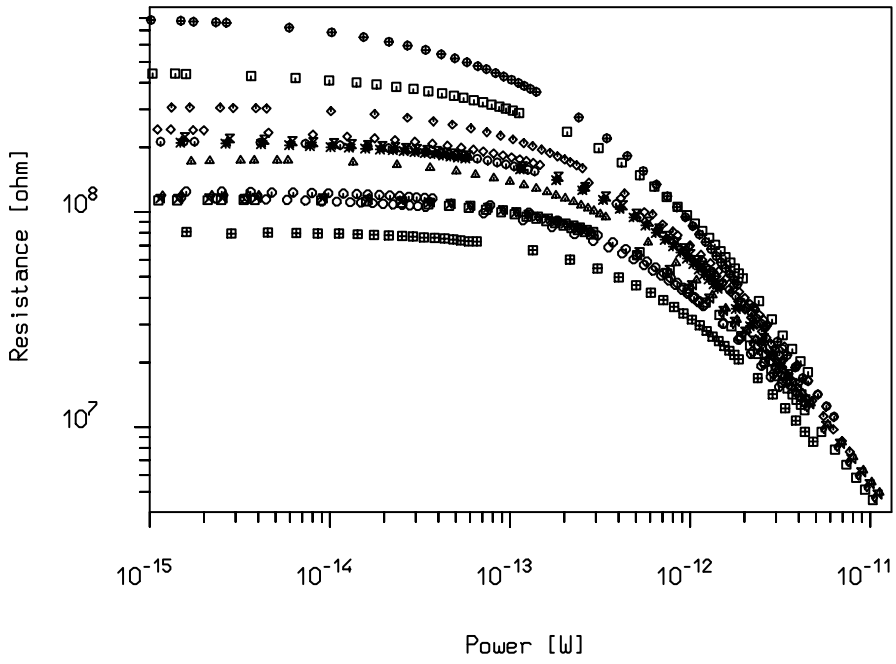

Figure 5.2: Fifteen thermistor load curves for the 20 crystal array.

5.1.1 Location

CUORE will be located in the underground hall A of Laboratori Nazionali del Gran Sasso (LNGS, L'Aquila - Italy) at a depth of 3500 m.w.e. where the muon flux is reduced to $\sim 3 \times 10^{-8}$ μ/cm^{-2}/s and the neutron flux to $\sim 10^{-6}$ n/cm^{-2}/s. After the approval of CUORE by the Gran Sasso Scientific Committee its final location just near the CRESST installation was decided as shown in Fig. 5.3

5.2 Sensitivity and discovery potential

As discussed in Chapter 1, a number of recent theoretical interpretations of atmospheric, solar and accelerator neutrino experiments imply that the effective Majorana mass of the electron neutrino, $|\langle m_\nu \rangle|$, expressed in Eq. 1.5, could be in the range from 0.01 eV to the present bounds.

In the remaining of the section, the Physics Potential of the CUORE experiment with respect to its double beta decay discovery potential. For this purpose, we will rely on the CUORE background expected sensitivity tested with the results already obtained in CUORICINO (sec. 4.2). More details on the expected background are described in sec. 5.3).

5.2.1 Expected performances

In CUORICINO the background is improved by a factor 1.5 with respect to the one measured in MiDBD-II in the $\beta\beta(0\nu)$ region. The analysis of the low energy region, relevant for dark matter search, has not been completed but we expect a similar improvement there also. For what

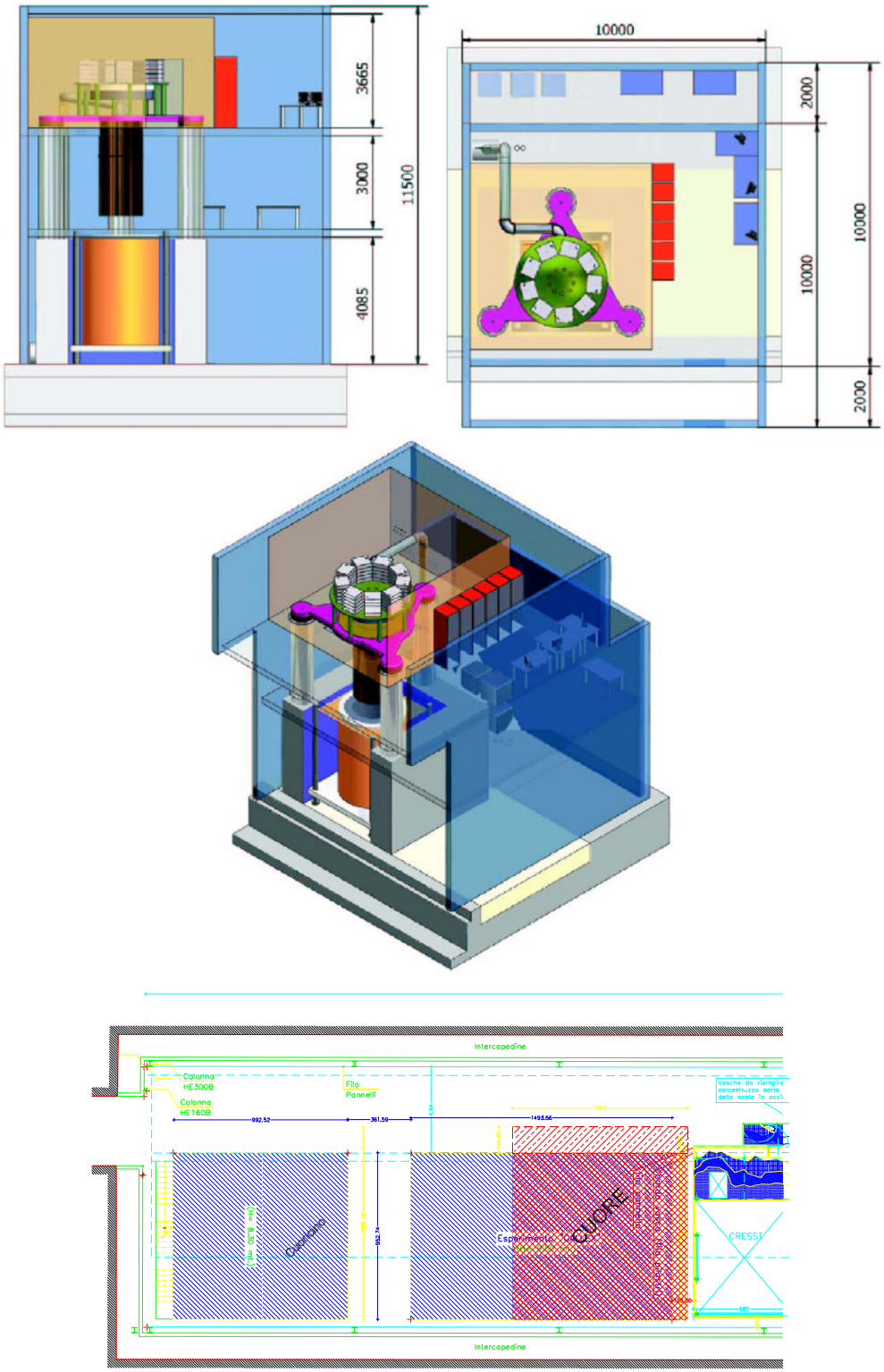

Figure 5.3: Design of the CUORE building with the cryostat installation: front view (top left), top view (top right) and 3D projection. Below: final location of CUORE in Hall A of the underground Laboratori Nazionali del Gran Sasso.

concerns CUORE on the other hand, MiDBD and CUORICINO have shed light on how the background contamination dominating the two regions of interest is mostly the intrinsic background due to bulk and surface contaminations of the constructing materials. With the presently achieved quality of low contamination materials and considering the worst possible condition for bulk contaminations (i.e. all the contamination equal to the present 90%/,C.L. measured upper limits) we proved that the corresponding contribution to the CUORE background will be $\sim$0.004 counts/(keV kg y) at the $\beta\beta(0\nu)$ transition energy and $\sim$0.025 counts/(keV kg d) near threshold (see section 5.3). Even at these conservative values therefore, bulk contaminations will not represent a problem for CUORE sensitivity. A larger background contribution is however expected when extrapolating to CUORE the surface contributions measured in CUORICINO. A dedicated R&D aiming at reducing the radioactive surface contaminations of the detector structure (mainly copper) is therefore required. The details on this activity are reported in Chapter 8. A reduction by an order of magnitude of the surface contributions would be enough to reduce the $\beta\beta(0\nu)$ background contributions to the level of few counts/keV/ton/y. Further improvements are still possible (e.g. active surface bolometers) and are considered by the CUORE collaboration as part of a second R&D phase aiming at an even better sensitivity both for $\beta\beta(0\nu)$ and dark matter searches. In particular, the goal of this CUORE technical R&D will be the reduction of background to the level of $\sim$0.001 counts/(keV kg y) at the $\beta\beta(0\nu)$ transition energy and to $\sim$0.01 counts/(keV kg d) at threshold. The potential of the experiment in this background configuration will also be discussed.

Regarding the expected threshold and resolution, energy thresholds of $\sim$5 keV and energy resolutions lower than 1 keV at the 46 keV line of ^{210}Pb were obtained in some test measurements carried out at LNGS ("Hall C" setup) for the early CUORE R&D program [137, 138]. We will assume therefore conservative values of 10 keV for the energy threshold and of 1 keV for the energy resolutions at threshold, as observed in MiDBD and CUORICINO. As far as the energy resolutions obtained in the double beta decay region, values of 3 keV at 2615 keV were achieved in some of the above mentioned test measurements. On the other hand, a 9 keV average value has been measured in the CUORICINO calibration spectra. A possible energy resolution interval of 5-10 keV (taking into account possible improvements in the foreseen CUORE R&D, Chapter 9) will be therefore assumed for CUORE.

Taking into account these expectations, we discuss in the following the prospects of CUORE for double beta decay searches.

5.2.2 Double beta decay prospects

The main scientific objective of the CUORE detector is the search for the neutrinoless double-beta decay of the ^{130}Te isotope contained in the (natural) TeO_2 crystals.

The detector factor-of-merit $F_D^{0\nu}$ (Tab. (1.2.1)), or detection sensitivity, introduced earlier by Fiorini, provides an approximate estimate of the neutrinoless half-life limit (1σ) achievable with a given detector. In the case of a 5$\times$5$\times$5 cm^3 TeO_2 bolometers (for which the $\beta\beta(0\nu)$ detector efficiency is 0.86) we have $F_D^{0\nu} \sim 7.59\times10^{23}\sqrt{\frac{Mt}{B\Gamma}}$, with M the crystal mass in kg and B the background in counts per keV per year and per kg of detector mass.

To demonstrate the full CUORE physics potential, let us evaluate F_D according to our conservative projection for the CUORE array (750 kg of TeO_2). We assume that a background of B=0.01 c/keV/kg/y would be achievable with a slight improvement of the current available

material selection and cleaning techniques and exploting the possibility to build a dedicated cryostat with low activity materials and effective shields. Assuming finally an energy resolution Γ(2.5 MeV)=5 keV, we get $F_D^{0\nu}$ of $9.4\times10^{25}\sqrt{t}$ years ($6.5\times10^{25}\sqrt{t}$ years for Γ=10 keV), which in t years of statistics would provide $|\langle m_\nu\rangle|$ bounds in the range 0.036–0.2 $t^{-1/4}$ eV (according to QRPA models F_N predictions, Tab. 1.2.1). However, the R&D to be carried out in CUORE, if successful, would provide a value of B$\sim$0.001 c/keV/kg/y, i.e. a detection sensitivity of $F_D\sim2.96\times10^{26}\sqrt{t}$ years ($2.1\times10^{26}\sqrt{t}$ years for Γ=10 keV), or $|\langle m_\nu\rangle|$ bounds in the range $\sim$0.02–0.11 $t^{-1/4}$ eV. TeO_2 crystals made with ^{130}Te enriched material have been already operated in MiDBD and CUORICINO, making an enriched CUORE a feasible option. Assuming a 95% enrichment in ^{130}Te and a background level of b=0.001 c/keV/kg/y, the sensitivity would become $F_D\sim8.32\times10^{26}\sqrt{t}$ years. For an exposure of 5 years, the corresponding $|\langle m_\nu\rangle|$ bounds would range from 8 meV to 45 meV depending on the nuclear matrix element calculations.

5.3 Simulation and predicted performances

The goal of CUORE is to achieve a background rate in the range 0.001 to 0.01 counts/(keV·kg·y) at the $\beta\beta(0\nu)$ transition energy of ^{130}Te (2528.8 keV). A low counting rate near threshold (that will be of the order of $\sim$5–10 keV) is also foreseen and will allow CUORE to produce results for Dark Matter and Axions searches. In Sec. 5.3.1 a very conservative evaluation of the background attainable with CUORE is presented; this is mainly based on the state of the art of detector design and of radioactive contaminations. This rather pessimistic approach in background evaluation is the only one that presently guarantees a reliable prediction. More details on the present R&D effert are reported in Chapter 8.

5.3.1 Background simulations

Radioactive contamination of individual construction materials, as well as the laboratory environment, were measured and the impact on detector performance determined by Monte Carlo computations. The code is based on the GEANT-4 package; it models the shields, the cryostat, the detector structure and the detector array. Even smallest details of the detector apparatus (copper frames, screws, signal wires, NTD thermistors, etc.; Fig. 5.4) and of the cryogenic setup are taken into account.

Table 5.1: Bulk contamination levels (in picograms per gram) used in the simulation for TeO_2 , copper and lead.

Contaminant	^{232}Th	^{238}U	^{40}K	^{210}Pb	^{60}Co
TeO_2	0.5	0.1	1	10 μBq/kg	0.2 μBq/kg
copper	4	2	1	0	10 μBq/kg
Roman lead	2	1	1	4 mBq/kg	0
16 Bq/kg lead	2	1	1	16 Bq/kg	0

It includes the propagation of photons, electrons, alpha particles and heavy ions (nuclear recoils from alpha emission) as well as neutrons and muons. For radioactive chains or radioactive

isotopes alpha, beta and gamma/X rays emissions are considered according to their branching ratios. The time structure of the decay chains is taken into account and the transport of nuclear recoils from alpha emissions is included.

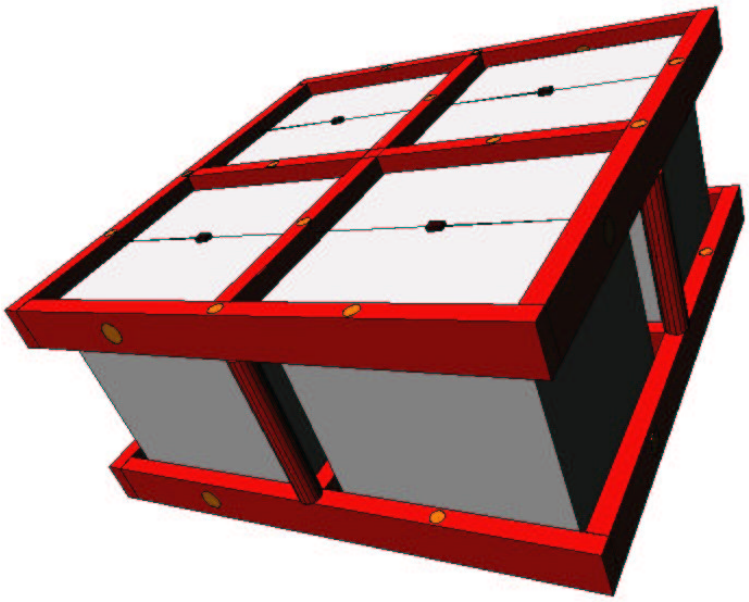

Figure 5.4: Details of the CUORE single modules accounted for in the Monte Carlo simulations

The considered background sources are:

1. bulk and surface contamination of the construction materials from the ^{238}U, ^{232}Th chains and ^{40}K and ^{210}Pb isotopes;
2. bulk contamination of construction materials due to cosmogenic activation;
3. neutron and muon flux in the Gran Sasso Laboratory;
4. gamma ray flux from natural radioactivity in the Gran Sasso Laboratory;
5. background from the $\beta\beta(2\nu)$ decay.

In the next sections these background sources and their contribution to CUORE background are discussed. It will be shown that, in a very conservative approach where the CUORE-tower mechanical structure is assumed identical to the structure used in CUORICINO, considering the worst possible condition for bulk contaminations (i.e. all the contamination equal to the present 90% C.L. measured upper limits (Table 5.1)) and assuming for surface contamination a reduction of about a factor ten with respect to CUORICINO, the CUORE background will be $\sim$0.007 counts/(keV·kg·y) at the $\beta\beta(0\nu)$ transition and $\sim$0.05 counts/(keV·kg·d) near threshold.

5.3.2 Bulk contaminations

The main contribution to background from bulk contaminants comes from the cryostat structure (cryostat radiation shields), the heavy structures close to the detectors (the copper mounting structure of the array, the Roman lead box and the two lead disks on the top of the array) and from the detectors themselves (the TeO_2 crystals). The radioactivity levels used in the computations for these materials are given in Table 5.1. These levels are nearly equal to the best upper limits obtained for the radioactive content of these same materials as shown in Table 5.2.

All the values reported in this table are 90% upper limits. Indeed in all cases no evidence of the presence of radioactive contaminants was obtained for the material examined. The contamination levels of TeO_2 reported in Table 5.2 were obtained from the data collected in the first run of CUORICINO with the $5\times5\times5$ cm^3 crystals. Copper [139] and lead [140] contaminations were determined through low activity Ge spectrometry. These data represent the best evaluation reported in literature for the radioactive contamination of TeO_2, copper and lead. From a comparison between Table 5.2 and Table 5.1 it is clear that the contamination levels assumed for the CUORE simulation are perfectly compatible with the presently available upper limits. The only exception is that of ^{60}Co in TeO_2 crystals, whose presence as a cosmogenic contamination of the crystals will be discussed later (sec. 5.3.4).

Concerning small (mass) components of the CUORE detector, which we have not considered so far in the simulation (e.g. NTD Ge thermistors, Si heaters, glue layers, pins, wires and soldering material,etc.), a very careful selection according to their contamination is planned for the future. In some case we already have upper limits on their contamination that make their contribution to the CUORE background negligible; in other cases further measurements will be required.

The results of the Monte Carlo simulations (see Fig. 5.5) using the contamination levels discussed here are given in Table 5.3 for the $\beta\beta(0\nu)$ decay and the low energy (10-50 keV) regions. The assumed threshold is 10 keV and only values obtained after requiring an anticoincidence between detectors are indicated. These values have to be considered as upper limits on the possible contribution of bulk contaminations to the CUORE background; they prove that with the available materials, background levels lower than $\sim4\times10^{-3}$ counts/keV/kg/y in the $\beta\beta(0\nu)$ decay region (see Fig .5.6) and $\sim3\times10^{-2}$ counts/keV/kg/d in the low energy (10-50 keV) region (see Fig.5.7) are assured.

Table 5.2: Available 90% C.L. upper limits for bulk contaminations of TeO_2, copper and lead (levels in picograms per gram if not differently indicated).

Contaminant	method	^{232}Th	^{238}U	^{40}K	^{210}Pb	^{60}Co
TeO_2	bolometric	0.7	0.1	1.	100 μBq/kg	1 μBq/kg
Copper [139]	Ge diodes	5.6	2	0.3	-	10 μBq/kg
Roman lead	Ge diodes	50	30	2	4 mBq/kg	-
Low act. lead [140]	Ge diodes	3.4	2.7	1.7$\pm$ 0.3	23.4$\pm$ 2.4 Bq/kg	18$\pm$ 1 μBq/kg

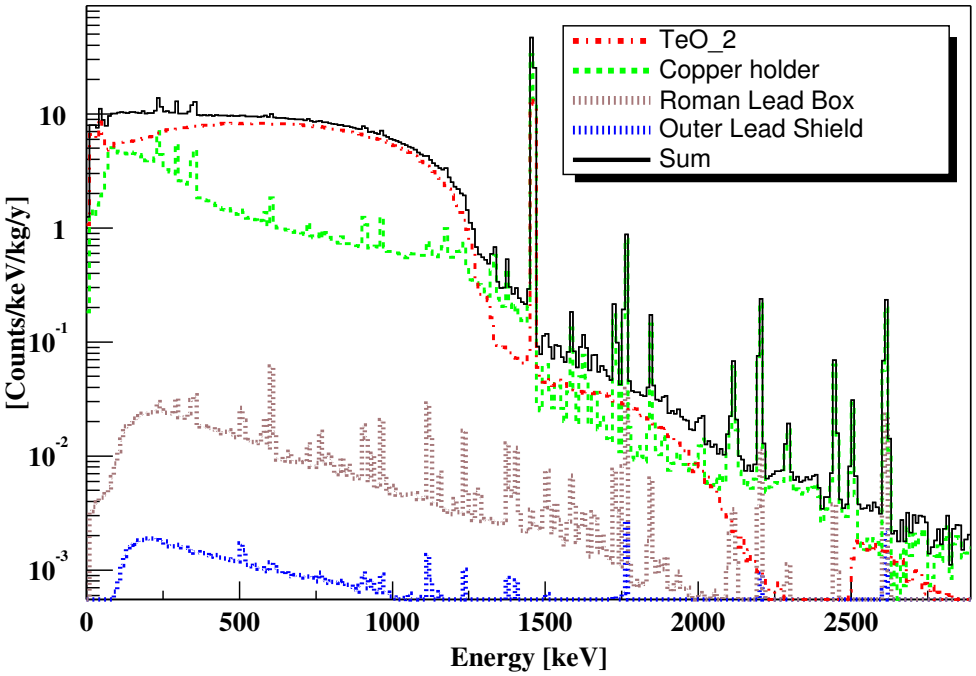

Figure 5.5: Simulated spectra for bulk contaminations of the TeO_2 crystals, the Copper structure, the Roman Lead shield and the outer Lead shield. Each spectrum is obtained by summing the simulated anticoincidence spectra of all the CUORE detectors.

5.3.3 Surface contaminations

Surface contaminations contribute to the background only when they are localized on the crystals or on the copper mounting structure directly facing them. As learned in MiDBD and CUORICINO (Chapters 3 and 4), the presence of even a very low level of radioactive impurities on the surfaces of the detectors can produce a non negligible contribution to the $\beta\beta(0\nu)$ background level. Unfortunately this kind of contamination, that is important mainly for detectors without a surface dead layer (as is the case of bolometers), is poorly studied. Lacking any data coming from direct measurements of the typical impurity levels present on TeO_2 and copper surfaces, we rely on the results obtained in MiDBD and CUORICINO.

These indicate that both a surface contamination of the crystals and of the copper surface of the mounting structure is present. In the case of TeO_2 , we know that the contamination is mainly ^{238}U and that its presence is strictly connected to the kind of surface treatment suffered by the crystals. In the CUORICINO $5\times5\times5$ cm^3 crystals this contamination produces a background counting rate in the $\beta\beta(0\nu)$ region of about $(4\pm 3)\times10^{-2}$ counts/keV/kg/y (table 4.2). Concerning the copper surface contamination, we still miss a clear indication of its origin and identity (i.e. we are not yet able to distinguih between contributions generated by different sources), but we have an evaluation of the $\beta\beta(0\nu)$ background counting that can be ascribed to them (whatever they are, ^{238}U or ^{232}Th): $\sim0.1\pm$ 0.05 counts/keV/kg/y.

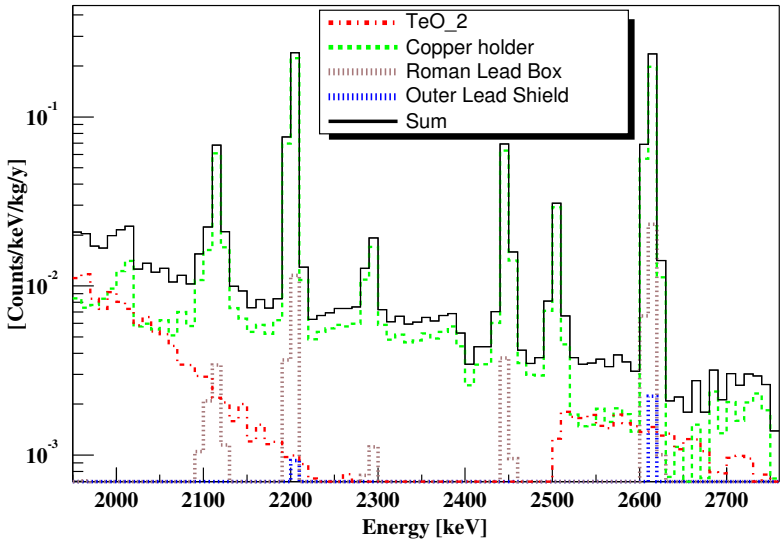

Figure 5.6: Double beta decay region of the simulated spectra for bulk contaminations of the TeO_2 crystals, the Copper structure, the Roman Lead shield and the outer Lead shield. Each spectrum is obtained by summing the simulated anticoincidence spectra of all the CUORE detectors.

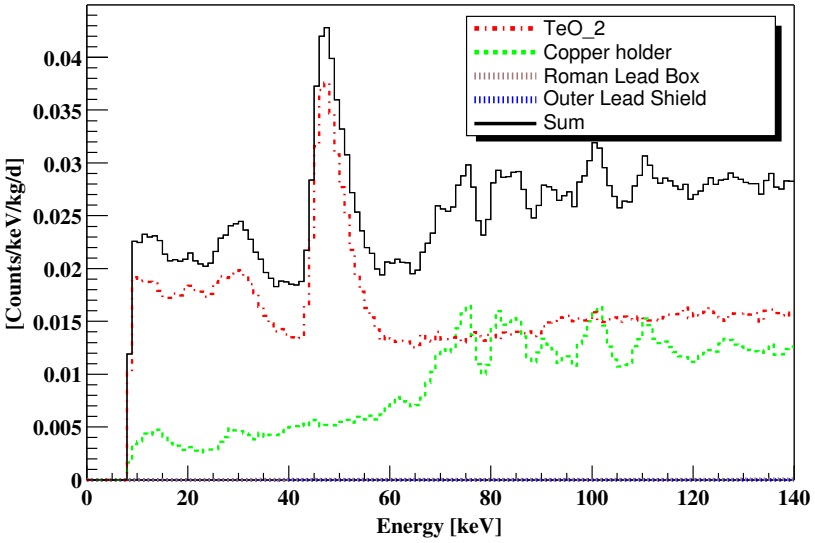

Figure 5.7: Dark matter region of the simulated spectra for contaminations of the TeO_2 crystals, the Copper structure, the Roman Lead shield and the outer Lead shield. Each spectrum is obtained by summing the simulated spectra of all the CUORE detectors after the anticoincidence cut.

Simulated element	TeO_2 crystals	Cu structure	Pb shields	TOTAL
$\beta\beta(0\nu)$ decay region counts/keV/kg/y	1.6×10^{-3}	1.5×10^{-3}	7.0×10^{-4}	3.8×10^{-3}
dark matter region counts/keV/kg/d	2.3×10^{-2}	9.6×10^{-4}	5.0×10^{-5}	2.4×10^{-2}

Table 5.3: Computed background in the $\beta\beta(0\nu)$ decay and in the low energy regions for bulk contaminations in the different elements, the Cu structure accounts for the detector mounting structure and the 50 mK shield.

According to a Monte Carlo simulation of the CUORE detector, based on the CUORICINO contamination levels, we obtained a background counting rate in the $\beta\beta(0\nu)$ region (after the anticoincidence cut) of about 1.6×10^{-2} counts/keV/kg/y and 5.8×10^{-2} counts/keV/kg/y for the TeO_2 crystals and the copper structure respectively 5.5. The goal of CUORE is to reduce the surface contribution by a factor at least 20 with respect to this evaluation, obtaining a background coming from surfaces of about 3×10^{-3} counts/keV/kg/y. Improvements of a factor of $\sim$1.5–2 are expected simply by possible reductions of the copper mounting structure dimensions (the Monte Carlo simulation we used so far refers to an identical mechanical structure for the CUORE and CUORICINO single detector modules). A reduction by a factor of at least ten of the copper (TeO_2) surface contamination is therefore the first milestone of CUORE.

The expected shape of the background produced by surface contaminations in CUORE (after a reduction by a factor 20 of both the crystal and copper surface contaminations but assuming the same mechanical structure of CUORICINO) is given in Figures 5.8 and 5.9. The corresponding background contributions in the two regions of interest are summarized in Table 5.4.

The MiDBD crystal surfaces were contaminated, probably during the polishing procedure with highly contaminated powders. Polishing powders with a much lower radioactive content are however commercially available [141] and have already been used for CUORICINO (see Chapter 4) obtaining a clear improvement in the surface contamination. Final complete control of the surface treatments undergone by the crystals after growth, and the use of radiopure substances should guarantee an even better result than that obtained in CUORICINO.

A similar situation holds for copper. In MiDBD and in CUORICINO the copper surfaces were treated with an etching procedure [142] optimized in order to reduce impurities on surfaces before the sputtering process.

This procedure significantly improved the surface quality of copper and reduced its surface contamination. However it was not optimized from the point of view of background. The use of low contaminated liquids (water and inorganic acids are available with ^{238}U and ^{232}Th contamination levels lower than 0.1 pg/g) in a low background environment will allow a considerable improvement of the copper surface contamination.

Cleaning methods similar to those used in building CUORICINO but with much more care taken to prevent radioactive contamination are under study . The results of this activity will be reported in Chapter 8. Fast diagnostic methods to measure the surface contamination levels of copper and determine the effectiveness of the adopted surface cleaning procedures are also under investigation. Preliminary results indicate that high resolution ICPMS could satisfy our

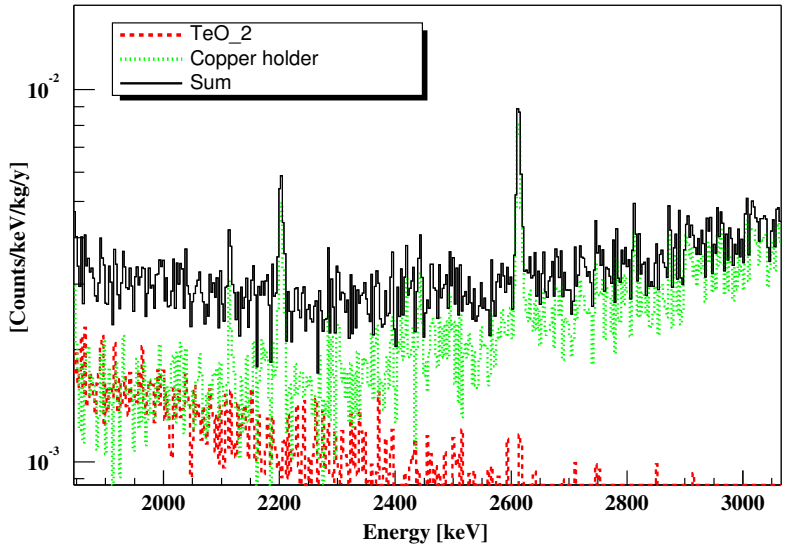

Figure 5.8: $\beta\beta(0\nu)$ region of the simulated spectra for the surface contaminations of the TeO_2 crystals and of the Copper structure. Each spectrum is obtained by summing the simulated spectra of all the CUORE detectors aftre the anticoincidence cut.

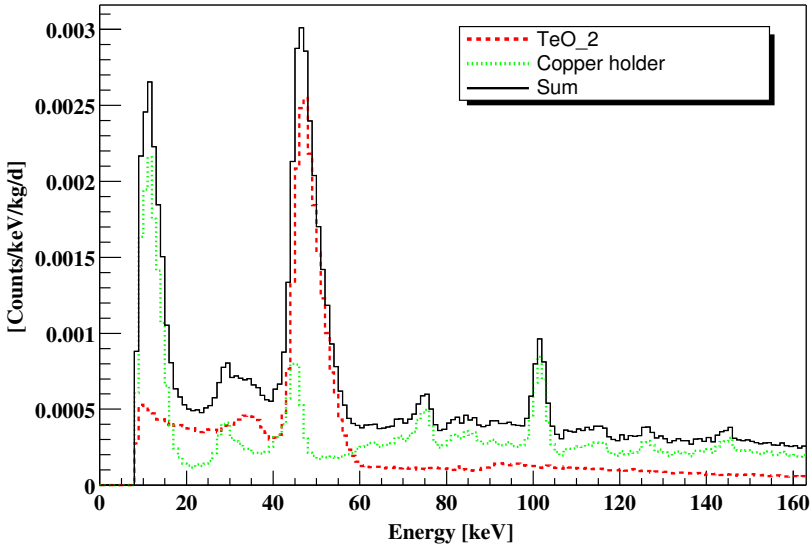

Figure 5.9: Dark matter region of the simulated spectra for the surface contaminations of TeO_2 crystals and of the Copper structure. Each spectrum is obtained by summing the simulated anticoincidence spectra of all the CUORE detectors.

Cylindrical structure

Simulated	^{232}Th	^{238}U	^{60}Co	Sum
TeO_2	212±23.6	14.5±5.11	1200±19.5	1420±31.0
Cu Box	393±46.3	84.8±28.3	-	4784±54.3
Cu Bars	29.7±4.08	27.1±5.12	-	56.8±6.55
Cu Frames	163±21.5	233±33.7	-	397±39.9
Cu 50mK Shield	31.9±2.21	-	-	31.9±2.21
Roman Pb Shield	604±24.4	-	-	604±24.4
Sum	1430±61.5	360±44.6	1200±19.5	2390±74.5

Table 5.4: Computed background (after the anti-coincidence cut) in the $\beta\beta(0\nu)$ energy region for bulk contaminations in the different elements for cylindrical structure in units of 10^{-6} c/keV/kg/y.

Element	Contamination Bq/cm^2	Contribution to the$\beta\beta(0\nu)$ region c/keV/kg/y
TeO_2	1.9E-08 ± 9.8E-09	1.6E-02 ± 8.4E-03
Copper	4.9E-08 ± 1.9E-08	5.8E-02 ± 6.6E-03
Total	3.4E-08 ± 1.3E-08	7.4E-02 ± 1.1E-02

Table 5.5: Estimated upper contribution to the CUORE $\beta\beta(0\nu)$ region from surface contaminations obtained by using the surface contamination levels evaluated for CUORICINO and assuming an exponential density profile with λ=1 μm for TeO_2 crystals (^{238}U) and λ=5 μm for Copper (^{238}U and ^{232}Th).

requirements [143]. Sensitivities achievable with this technique for ^{238}U and ^{232}Th are in the range of $10^{-(3-2)}$ ppt of solution under investigation. Since the maximum solution concentration can be 2×10^{-3}, the expected sensitivity on the solute contamination (copper) would be in the range 1–10 ppt of ^{238}U and ^{232}Th, i.e. enough for our requirements. From the above discussion in fact, the surface contamination measured in CUORICINO (assuming a 1 μm copper layer) is of the order of ∼1–10 ppb of ^{238}U and ^{232}Th. Of course, radio-purities comparable with the instrumental sensitivity are required for liquids (mainly acids and water) to be used in the solution preparation. Liquids satisfying this requirement are however already commonly available.

5.3.4 Cosmogenic contribution

Cosmogenic activation is produced by cosmic rays when the crystals are above ground (during fabrication and shipping to the underground laboratory). To determine the activation we used COSMO, a code computing cross sections, to estimate the type and amount of radionuclei produced by cosmic rays on TeO_2 [144]. The radionuclei produced by the activation of tellurium are mostly tellurium isotopes (A=121,123,125,127) as well as ^{124}Sb, ^{125}Sb, ^{60}Co and tritium, these last three being of more concern because of their long half-life (^{125}Sb: beta decay of 2.7 years, end-point energy of 767 keV, ^{60}Co: beta decay of 5.27 years end-point energy 2823 keV

and ^{3}H: beta decay of 12.3 years, end-point energy of 18 keV).

We have studied and agreed, together with SICCAS (the company that produces the crystals) a possible time schedule for the crystal growth and shipping to Gran Sasso that can guarantee the required low level contamination of ^{60}Co (see Fig .5.10). In the case of CUORE, the control on crystal production will be severe. A single 750 g crystal can be grown in about two months, while to grow the 988 CUORE detectors will require 18 months. Once grown the crystals will be shipped to Italy and stored underground, therefore their total exposition to cosmic rays could be limited to about 4 months. The total induced activities remaining after 2 years underground have been estimated [144] and the consequent contribution to the detector counting rate was deduced by a MC simulation. The radionuclei that contribute to background through their β^- decay are:

- the long living ^{60}Co isotope, with an activity of $\sim$0.2 μBq/kg in the $\beta\beta(0\nu)$ region; a minor contribution is due to the isotopes ^{110m}Ag and ^{124}Sb whose activity is 4 times lower and faster decreasing with time;
- in the dark matter regions the long lived nuclei of ^{3}H and ^{125}Sb with activities of $\sim$7 μBq/kg and of $\sim$15 μBq/kg, respectively.

The influence of ^{60}Co to the CUORE background was already considered in the evaluation of the contributions due to bulk contaminations of the crystals, while the contribution of ^{3}H and ^{125}Sb to the dark matter region is completely negligible if compared to the intrinsic background from all other sources.

A recent experimental determination of the ^{60}Co production cross section on Te by 1.85 GeV protons has been obtained at LNBL. The measured value (0.63$\pm$0.15 mb) is in strong disagreement with the value used by the COSMO program. A similar disagreement, even if at a lower extent, has been found on the basis of an activation measurement carried out at CERN at an energy of 24 GeV, which is however less important for cosmic ray activation. The contribution to CUORE $\beta\beta(0\nu)$ background by cosmogenic ^{60}Co discussed above, could be therefore overestimated and the allowed exposure period for TeO_2 crystals could be consequently much longer. Further measurements of the ^{60}Co production cross section are therefore of crucial importance and we plan to have, in the near future, other direct measurements by irradiating Tellurium samples with proton beams of suitable energies.

5.3.5 Underground neutron, μ and γ interactions

As mentioned earlier, neither contributions from underground cosmic muons nor neutrons have been taken into account in detail in the estimation of the background. However, the following simplified arguments will serve to have an approximate idea of their contribution. The depth of the LNGS (3500 m.w.e) reduces the muon flux down to $\sim 2\times10^{-8}$ cm^{-2}s^{-1}, but a further effective reduction could be obtained with the use of an efficient (99.9%) active veto for muons traversing the CUORE setup in order to tag possible events associated with them. The muon-induced contribution to the background is therefore expected to be negligible.

On the other hand, the heavy shields surrounding the CUORE detector will substantially reduce the event rate due to environmental radiation of various origin (neutrons and photons), environmental radioactivity (natural decay chains U/Th, ^{210}Pb, ^{40}K, ...), as well as muon interactions in the surroundings rock or in the shielding itself.

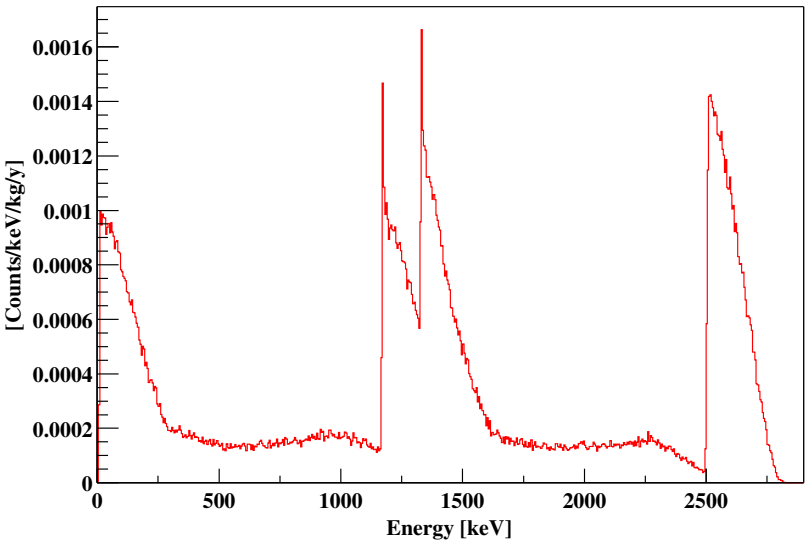

Figure 5.10: Simulated spectrum for the assumed ^{60}Co bulk contaminations of TeO_2 crystals. The spectrum is obtained by summing the simulated anticoincidence spectra of all the CUORE detectors.

Neutrons may constitute a worrisome background for the dark matter experiment because for appropriate neutron energies (few MeV) they can produce nuclear recoils ($\lesssim$100 keV) in the detector target nuclei which would mimic WIMP interactions. Simple kinematics implies that in the case of tellurium, neutrons of 1(5) MeV could elastically scatter off tellurium nuclei producing recoils of energies up to 31 (154) keV. In general, one considers neutrons of two origins: from radioactivity in the surroundings or muon-induced. Depending on the overburden of the underground site (i.e., depending on the muon flux), muon-induced neutrons are produced, at lesser or greater rate, both inside and outside the shielding. They are moderated (according to their energies) by the polyethylene/lead shield (when produced outside) or tagged by the muon veto coincidence (when produced within the passive shielding).

In the case of external neutrons (from the rocks, from fission processes or from (n,α) reactions, as well as neutrons originated by muons in the walls of the underground site), the environmental neutron flux has been measured in LNGS. The result is of $\sim 1\times10^{-6}$ cm^{-2}s^{-1} for the thermal component, $\sim 2\times10^{-6}$ cm^{-2}s^{-1} for the epithermal and $\sim 2\times10^{-7}$ cm^{-2}s^{-1} for energies over 2.5 MeV. They are fairly well moderated by the polyethylene and eventually absorbed or captured.

We have carried out a Monte Carlo simulation of the propagation of neutrons through the 10 cm thick borated polyethylene shield of CUORE. The result is that the neutron induced event rate on the entire energy range (from threhsold to 10 MeV) is much lower than the contribution due the bulk contamination of crystals. Neutrons produced by muon interaction inside the shielding materials are very scarce and they can be efficiently tagged by the muon veto. We have estimated that for the LNGS muon flux (2.5×10^{-8} μ/(cm^2 s)), muons would produce in the CUORE shielding of polyethylene (10 cm) and lead (20 cm)), about $\sim$0.04 neutrons/day in the

polyethylene shield and ∼25 neutrons/day in the lead shell. So, independent of the mechanism used to reject or tag the events associated to neutrons, their rather small number is expected to play a secondary role in the total background compared with other main sources of background.

A preliminary evaluation of the influence of the environmental γ background in Gran Sasso resulted in a negligible contribution for the $\beta\beta(0\nu)$ region and a contribution similar to that of bulk contaminations for the dark matter region.

A more complete and detailed study of the background rates from external sources for CUORE is underway and will be used for the optimization of shieldings and muon veto.

5.3.6 Two neutrinos double beta decay background

Using the present upper limits for the ^{130}Te $\beta\beta(2\nu)$ half-life, the unavoidable background produced by the $\beta\beta(2\nu)$ decay in the dark matter region is lower than 10^{-4} counts/(keV·kg·y) and is completely negligible in the $\beta\beta(0\nu)$ region. This is true because of the relatively good energy resolution of the TeO_2 bolometers.

Chapter 6

The R&D activity on CUORE detectors: motivations and experimental setup

As already mentioned above, my PhD activity was dedicated to the development of the single detector and of the final structure of the CUORE experiment. This is one of the main research activities in view of CUORE, being connected both with improving the sensitivity to reach the target mass region and to the standardization and engineering of the construction and assembly process of the final 988 detectors.

My activity was performed during the first three years of activity of the CUORICINO detector, which provided, for the first time, a statistically relevant amount of data from macrobolometers. The information coming from CUORICINO is the real starting point of this work.

In this chapter I will present the leading ideas that guided the R&D activity and the way this information was used to project new developments.

Finally I will describe the experimental setup of the R&D test facility located in Hall C of the Gran Sasso National Laboratory.

6.1 Detectors development: research lines

My PhD activity was developed following three main leading ideas with three different scientific goals:

- Increasing the detector's sensitivity.
- Improving the detector's reproducibility, comprehension and reliability.
- Improving the modularity of the final detector.

Actually the activity of the last three years gave rise to three different tests, each consisting of one or more cold runs in the Hall C R&D facility. Each of these tests was designed to follow one or more of these topics. In the following I will introduce motivations and ideas for the three different research lines. In the next three chapters the experimental runs will be described recalling the motivation of each specific measurement and detailing the setup.

6.2 Improving sensitivity

The sensitivity of the experiment for the νDBD process $S^{0\nu}$ is defined as the minimum number of detectable events over background at a given confidence level.

It can be estimated starting from the disintegration rate of the process:

$$N(\tau) \;=\; N_0 e^{-\lambda\tau} \tag{6.1}$$

where N_0 is the number of nuclei under control at τ = 0, τ is the time and λ the inverse of life time T. The half life of the process is the time $\tau_{1/2}$ for which $N(\tau_{1/2})$ = N_0/2. So:

$$\begin{aligned} \frac{1}{2}N_0 \;&=\; N_0 e^{-\lambda\tau_{1/2}} \\ ln(2) \;&=\; \lambda\tau_{1/2} \end{aligned} \tag{6.2}$$

Differentiating eq. 6.1 one has:

$$\frac{dN}{d\tau} \;=\; \lambda N(\tau) \;=\; \lambda N_0 e^{-\lambda\tau} \;=\; \lambda N_0 \tag{6.3}$$

for $T \;=\; \frac{1}{\lambda} \;\gg\; \tau$. On the other side the variation of the number of nuclei can be written as the number N_D of decays after a time t, divided by the measuring time t:

$$\frac{dN}{d\tau} \;=\; \frac{N_D}{t} \tag{6.4}$$

Substituting 6.4 in 6.3 one gets:

$$\lambda \;=\; \frac{N_D}{t \cdot N_0} \tag{6.5}$$

Now substituting this expression into 6.2:

$$\tau_{1/2} \;=\; ln(2) \cdot \frac{N_0 \cdot t}{N_D} \tag{6.6}$$

In order to detect N_D in an energy window ΔE (which corresponds to the energy resolution of the detector), the presence of the radioactive background counts is one of the most severe limiting factors. There are two possible cases: a)$b \neq$0: Fluctuations of the background can cover the expected peak; b)b=0: No background events are observed.

a) Here we will focus our attention on the problem that the peak could be hidden by background fluctuations (b$\neq$0). One might consider to assume the for background events, coming from nuclear decays, a Poissonian distribution for the background events coming from nuclear decays. The standard deviation is then the square root of the number of events. If we consider N_B background events at the time t in the energy window ΔE, the deviation is given by $(N_B)^{1/2}$.

For given N_B and t, the minimum number of decays N_D needed to reach a certain significance of the peak (i.e. a C.L. of ξ%), corresponds to the inverse probability of having a background events fluctuation equal to the peak:

$$N_D = n \cdot (N_B)^{1/2} \tag{6.7}$$

where n is the number of deviations corresponding to a probability of (1-ξ)%.

The sensitivity at a fixed C.L. is defined as the half life when the peak is exactly equal to n background fluctuation. Substituting 6.7 into 6.6 one has:

$$S_{n\sigma}^{0\nu} \equiv \tau_{1/2} = ln(2) \cdot \frac{N_0 \cdot t}{n \cdot (N_B)^{1/2}} \tag{6.8}$$

For values of N_D bigger the 10 the poissonian probability corresponds to the gaussian probability. Note that in the case of a peak plus background analysis only the positive fluctuations of the background events can simulate the peak. Therefore to calculate the confidence level only the positive fluctuations should be taken in account. Thus the probability of having a simulated peak given by an n standard deviations fluctuation is (1-P(within $n \cdot \sigma$))/2. For example a 1σ fluctuation of the background to simulate a peak has a probability of 16% instead of the usual 32%. To estimate the sensitivity of a given C.L. is then necessary to take in account this reduction: a 90% C.L. is given by a $1.19 \cdot (N_B)^{1/2}$ peak.

The number of background events in the energy region can be estimated as

$$N_B = b \cdot M \cdot t \cdot \Delta E \tag{6.9}$$

where b is the background level in counts/keV/kg/y in the detector and M the total detector mass (in kg). On the other hand, the total number of nuclei under control is

$$N_0 = (M \cdot a \cdot N_A/A) \cdot \epsilon \tag{6.10}$$

where A is the atomic (molecular) weight in Kg, N_A the Avogadro number, a the isotopic abundance of the isotope of interest and ϵ the detector efficiency for the process of interest. In the case of a molecular compound the final value should be multiplied by this number of atoms of interest per molecule.

Actually we need one more correction since here the fluctuations are calculated only on the FWHM (ΔE) interval and not on the entire Gaussian peak. Since the area under the Gaussian integrated only on the FWHM corresponds to 1.17σ, it is just 0.758 of the total and we should normalize N_D by this factor:

$$S_{n\sigma}^{0\nu} \equiv \frac{ln(2) \cdot 0.758}{n} \cdot N_A \cdot \frac{a}{A} \cdot \left(\frac{M \cdot t}{b \cdot \Delta E} \right)^{1/2} \cdot \epsilon \tag{6.11}$$

It is evident from this formula that to increase the sensitivity of the experiment, one must act on the parameters inside the square root M, t, b and ΔE or, if possible, on the isotopic abundance a. In the following sections the possibility of acting on each of this parameter is analyzed and commented.

b) One more comment should be added here for the case in which there are no measured events. To evaluate the sensitivity one consider that for the poissonian distribution, 0 observed events are compatible with μ_n events at a given C.L. ξ%. Therefore one should substitute in the 6.8:

$$\mu_n = n \cdot (N_B)^{1/2} \tag{6.12}$$

The sensitivity 6.11 becomes:

$$S_{n\sigma}^{0\nu} \equiv \frac{ln(2) \cdot 0.758}{\mu_n} \cdot N_A \cdot \frac{a}{A} \cdot M \cdot t \cdot \epsilon \tag{6.13}$$

Thus to increase in this case the sensitivity one should act on the mass and on the time of measurement.

6.2.1 Detector mass

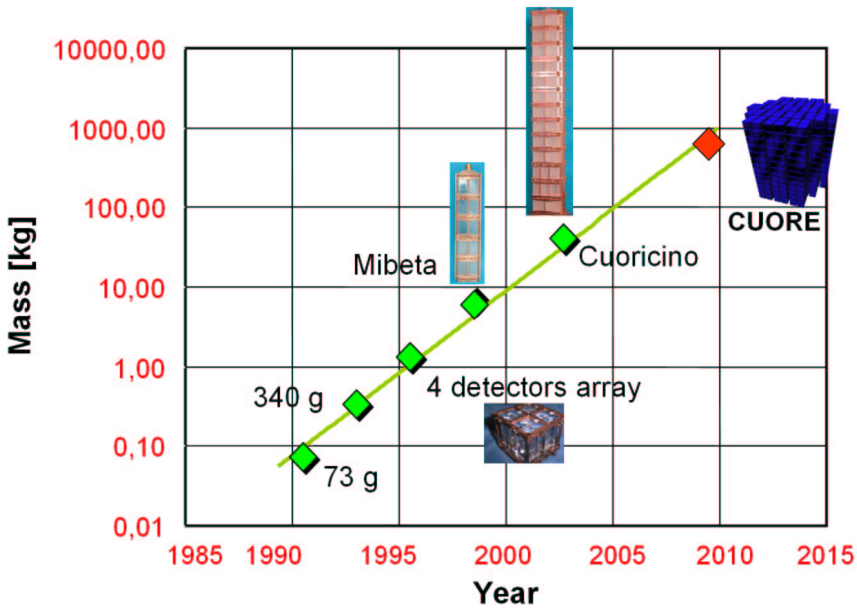

Figure 6.1: Time vs. mass evolution of TeO_2 bolometric experiments (Bucci's law). A gain of an order of magnitude is expected every 5 years.

Increasing the detector mass is the easiest way to increase the experiment sensitivity. Nevertheless, the present mass scale of TeO_2 experiments does not allow much increase. In fact, since CUORICINO mass is about 41 kg, an increase of at least one order of magnitude is needed to make a non-negligible gain in sensitivity.

The chosen solution for CUORE (988 detectors for a total mass of about 0.74 tons) will increase the sensitivity on the order of $\sqrt{M_{CUORE}/M_{CUORICINO}} \cong 4.25$. A further increase by the same factor requires another increase by a factor of (741/41) $\cong$ 18 in magnitude which is probably beyond the possibility of present cryogenic techniques for the cooling a large mass. Therefore the CUORE mass increase will be maximum feasible for present techniques.

Two different approaches were used: increasing the mass of a single absorber crystal and increasing the number of detectors. As described in Chapter 3, during the last fifteen years the Milano TeO_2 group pursued both strategies (see Fig. 6.1). These solutions have advantages and disadvantages. Increasing the number of channels has no consequences for the detector's behavior but implies major technical problems (large number of channels, large effort in optimizing different detectors, etc...) and bigger costs. On the other hand increasing the absorber mass is a cheaper solution (for the same mass the number of channels can be much lower). However, this gives rise to some physical problems. In fact, the heat capacity of the absorber grows proportionally with volume. Since the temperature variation for a given energy deposition E is ΔT

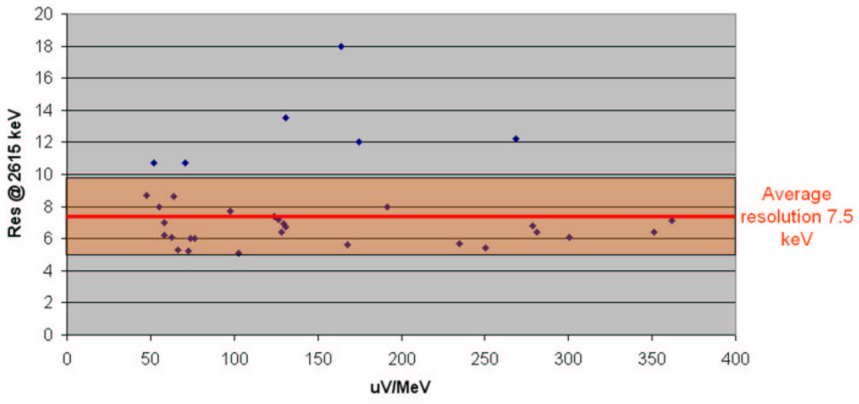

Figure 6.2: Energy resolution 2615 keV versus μV/MeV for CUORICINO's $5 \times 5 \times 5$ cm^3 detectors (run I).

= E/C, the bigger is C, the lower the pulse hight. In practice this problem does not affect the detector's behavior in terms of resolution and signal to noise ratio. This can be well understood by looking at CUORICINO data.

μV/MeV vs. Resolution

The best way to give a quantitative estimate of the variation of detector's behavior with C, is by using the detector response (μV/MeV). We denote with μV/MeV response of a detector (i.e. a thermistor) in μV to a given energy excitation.

In CUORICINO this parameter takes a wide range of values for different detectors. In Fig 6.2, CUORICINO's resolution values on ^{208}Tl gamma peak at 2615 keV are plotted versus μV/MeV (see sec. 6.2.2). One can immediately notice that there is no clear correlation between the resolution and the pulse height. This can be easily understood since CUORICINO detector's noise is dominated by the thermophononic (TP) component, the oscillation of the base T. TP noise is the result of heat dissipation in the detector converting it into phonons. Its major source is the friction noise which comes from vibrations being converted into heat via frictions between the crystal and the holder (PTFE, Cu, etc.). Other contributions can come from different phenomena like acoustic waves inside the crystal.

This means that both the energy pulse and the noise are produced inside the detector. Thus the the response of the detector in μV/MeV is the same for the energy pulse and for the baseline oscillations (TP noise). For example for a detector with a response of 50 μV/MeV a pulse 1 MeV gives rise to a response of 1 MeV $50 \cdot$ μV/MeV = 50 μV. On the same detector a noise fluctuation of 10 keV = 0.01 MeV give rise to a signal of 0.5 μV. The consequent S/N is (1 MeV $\cdot$ 50μV/MeV)/(0.05 MeV $\cdot$ 50μV/MeV) = 100 is independent from the response of the detector.

Therefore we can say that the resolution is more or less constant for different detector's responses.

To a rough approximation, the increase of the absorber mass does not affect the behavior of the detector. Nevertheless, one more comment should be added about the ongoing developments for noise reduction. One must consider the possibility that CUORE, due to the present R&D

effort, will not be dominated by TP noise but by electric or microphonic noises. In this case the higher the μV/MeV is, the better is the S/N. So one should choose the best compromise between the absorber mass and the response reduction (see next chapter for further discussion).

6.2.2 Energy resolution

The energy resolution in the 0νDBD region is evaluated as the FWHM of the γ peak of ^{208}Tl at 2615 keV. From Fig. 6.2 it is clear that the average resolution is quite good (a few per ‰ at 2615 keV) and the spread from average is quite small. In fact only $\sim 10\%$ of the detectors have a resolution worse than 9 keV and by excluding these channels the average goes from 7.5 keV down to 6.6 keV. This is already a notable performance but nevertheless it is still possible to improve the resolution for CUORE.

As we have seen in the previous section the resolution is roughly independent of the response of the detector. The only way to improve resolution is to reduce the noise on the detectors (i.e. TP noise). This must be done in two different ways: reducing the noise sources and reducing the sensitivity to noise of the detector.

Since is impossible to eliminate many of the important sources of noise (e.g. pumps and compressors of the cryogenic setup) the adopted solution is to try to prevent the transfer of these vibrations from the cryostat to the detector. The trivial part of this work is the use of common damping systems to decouple the vibrating machine as much as possible from everything else. This is not always passible since the pumps of the gas handling system are directly connected to the cryostat, and some vibration will pass through the pumping lines. The more delicate work consists in decoupling the detector from any vibration source via mechanical filters. This is usually done by using combined oscillating systems. This is non trivial due to the fact that the damping system has to operate at low temperature. Several developments are in progress on this topic (see for example [145]).

On the other hand the work of this thesis is focused on the reduction of sensitivity to noise of the single detector. We denote by sensitivity to noise the response of the detector to some external or internal perturbation of the apparatus like vibrations coming from the activities in the underground lab, mechanical noise from the cooling pumps and compressors, vibrations from 1K Pot filling, etc. This is mainly the sensitivity to TP noise. Unfortunately it is not easy to assign a figure of merit to this parameter to compare different detectors. This can be better done using two noise-parameters that are in some way complementary: baseline stability and N_{rms}. The stability (or instability) of the baseline is related to the sensitivity to noise of the detector. In the case of instability, the presence of triangular shaped oscillations can be observed (see Fig. 6.3). The behavior of the baseline is not a good parameter to evaluate the noise since is difficult to assign a quantitative information to the baseline variation. On the other hand, N_{rms} is a good parameter to use for comparison because it provides a precise numerical evaluation of the noise. Nevertheless N_{rms} must be carefully analyzed because of the different contributions entering in it (see par. 6.2.2).

Baseline stability

There are two contributions that influence the baseline stability in time: the performance of the dilution refrigerator and the presence of TP noise.

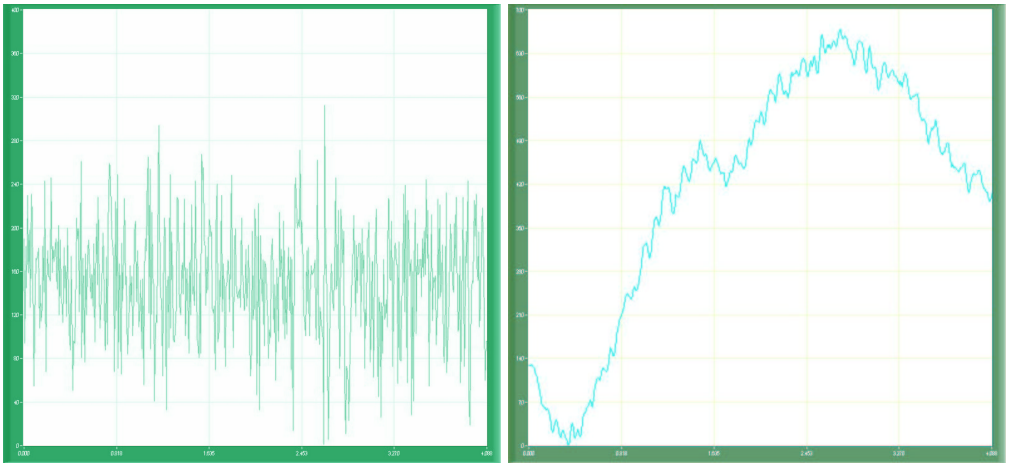

Figure 6.3: On the left a baseline with electric noise (pkpk $\sim$ 3 mV), on the right the effect TP noise with typical "triangular" shape (pkpk $\sim$ 45 mV).

The former comes from the fact that, if some proprieties of the cryostat slightly change in time, the baseline can change accordingly (variation of the LHe level in the MB, changing of the pressure on the condenser, etc). This problem can be corrected off line via software. The amplitude linearization of the test pulse as a function of the baseline is described in Chapter 4. Of course this can be done if the change is a well defined function of time (typically a straight line) and if the total variation is limited. If not there can be problems of resolution degradation. In summary, since the baseline variation corresponds to a slight change of the base temperature of the cryostat, you get a different response of the thermistor to the same released energy and this worsens the resolution. To minimize this problem a T stabilization technique was developed for CUORICINO. This keeps the entire detector at a fixed T above a base temperature by dissipating heat inside the detector by means of a ohmic resistor. The variations from T are compensated by increasing or decreasing the power on the tower (see [146]).

The second contribution to baseline instability is due to how tightly the crystal is held by the PTFE. In fact, since vibration is the main source of TP noise, sensitivity to noise is actually sensitivity to vibrations. Vibrations reach the crystal trough the Cu holder. Most vibrations are cut off by the mechanical filtering (a steel spring in CUORICINO [147]). Nevertheless if the crystal can move inside the holder, the oscillations are converted into heat and noise through friction. A good mechanical connection between detector and holder minimizes the heat dissipation. There are clear indications that the tighter the crystal is held by PTFE supports, the less sensitive to vibrations the detector is (the comparison can be done via rms noise and resolution).

The design and test of new PTFE supports and Cu holder is reported in chapter 9.

N_{rms} /G noise amplitude per unit of gain

The measurement of N_{rms} guarantees the possibility to compare the behavior of different detectors. This parameter is a good estimate of TP noise when its value is big. On the other hand, when TP noise is quite low, other contributions became comparable (e.g. Johnson noise) and it

is more difficult to evaluate the impact of vibrations. At present apparently the dominant contribution on most of the CUORICINO channels is by far TP noise. More comments on this are reported in chapter 9.

6.2.3 Measurement time and duty cycle

This topic is not part of this PhD work and I will not develop it too much. The modification of the measurement time can contribute only slightly to the increase of sensitivity. In fact the typical life of TeO_2 bolometric experiment is of a few years. After that, further contribution are more or less negligible. In fact if we get a certain sensitivity $S^{0\nu}$ after 5 years, then to increase the statistic by a factor 2 an increase of a factor of 4 in live time is required. This means that in 20 years of measurement the sensitivity is just two times better than after the first 5 years.

The only important work in progress on measurement time is regarding the increase of the duty cycle. There are two different kinds of limitation on this: first calibrations and DAQ settings and second apparatus maintenance and failures, respectively. Calibration and DAQ settings cannot be significantly reduced at the moment; their contribution to the total activity time is between 6% and 10%. This percentage cannot be significatively reduced in the future experiment since it is necessary for a good quality of the measurement. The second point is more delicate. In fact apparatus failure caused big problems in Run I and in the first part of Run II due to the presence of the LHe liquefier connected with the cryostat. For several months we got a live time as bad as 25%. Presently the situation is improved since the old He liquefier was dismissed and now the cryostat is refilled every two days with LHe. This operation contributes to the dead time with another $\sim$10%. This contribution will be possibly removed in CUORE due to the new LHe-free cryostat presently under construction. Unfortunately there is a contribution of about 15% of the dead time that comes from apparatus failures, due to the oldness of CUORICINO's cryostat and to the unavoidable critical state of all 10 mK machines, respectively. in present duty cycle is $\sim$65; results better than 75% are impossible even for the future experiments.

6.2.4 Background

It turns out that background comes out to be the most important parameter. In fact from previous section, we saw that once fixed the detector mass the only tunable parameter available to increase significantly sensitivity is the background. Therefore background reduction is the main development required for CUORE,

This work is obviously strongly connected with the interpretation of CUORICINO data and the understanding of the origin of the background. Several analysis have been done on this topic (main reference can be found in [134, 133]).

My activity is concentrated on the so called Internal Background Source (IBS). With this expression we refer to those radioactive contaminations that are inside the lead shields and cannot be suppressed using any kind of shielding, being very near the detector or on the detector itself. There are parallel activities going on to reduce External Sources of Background (EBS). The main effort of EBS reduction development is focused on the shielding against external radiations (lead for gammas, hydrogen compounds loaded with boron for neutrons) and on the flagging of very high energy cosmic rays (muon veto).

As pointed out in chapter 5 the main source of internal background is the surface contamination which is the result of the machining process of the different materials constituting the detector whose bulk contamination are on the contrary selected to be very low (see Tab. 5.3). More details are reported in chapter 8.

Two different strategies were adopted to solve this problems: the first aims to reduce the amount of contaminants on the surface of the materials (clean the materials) and the second to reduce the amount of material at all. The latter refers of course only to inactive material. The first task, from which the major reduction is expected, leads to the developing of a new cleaning procedure and to some special tests of contamination of specific material that have been tested in two dedicated measurements in the R&D test facility. This will be reported in chapter 8. The second task is a part of the complete re-design of the detectors holder realized for CUORE that will be presented in chapter 9.

A third contribution to this effort was proposed and tested by introducing the $6 \times 6 \times 6$ cm^3 TeO_2 absorbers. This approach, as will be detailed in the next chapter changes the surface to volume ratio, reducing the amount of radioactive surface contamination per gram. This test even if successful didn't lead to modifications of the CUORE design for several reasons that will be explained later.

6.2.5 Isotopic enrichment

Isotopic enrichment can be very important for the sensitivity of an experiment since $S^{0\nu}$ is directly proportional to a (see Eq. 6.13). In TeO_2 bolometers this contribution is not so significant due to the high natural isotopic abundance of ^{130}Te ($\sim$34%). Nevertheless, this option is considered with interest from the collaboration since can guarantee an increase of sensitivity of a factor 3 with a relatively small effort. It should be mentioned though that the experience of the Milano group with the enriched crystals in MiBeta and CUORICINO was not positive because of the bad quality of the enriched TeO_2 powder. This indicates that probably, if the enrichment option is chosen, some R&D is probably needed.

6.3 Improving detector's behavior and reproducibility

As widely reported, CUORICINO obtained very good performances on different bolometers. Nevertheless there are still large differences of behavior from one detector to another. This has been observed mainly in the detectors response (see Fig. 6.2) and in the corresponding pulse shape. In figure 6.4 normalized pulses from different detectors are plotted. The energy resolution shows a smal spread in values. This spread, even if it is small, is the strongest motivation of an effort of improving reproducibility.

The main reasons that are pushing ahead this activity are related with the data analysis of a larger number of channels. There are two main requests: one is more technical , the other more physical.

6.3.1 Pulse shape and response

First, let us notice that the more the behavior of different detectors is similar, the easier is the application of automatic procedures or standard software algorithms. This is connected also to the fact that a reproducible behavior can help in the comprehension of the physics of the detector

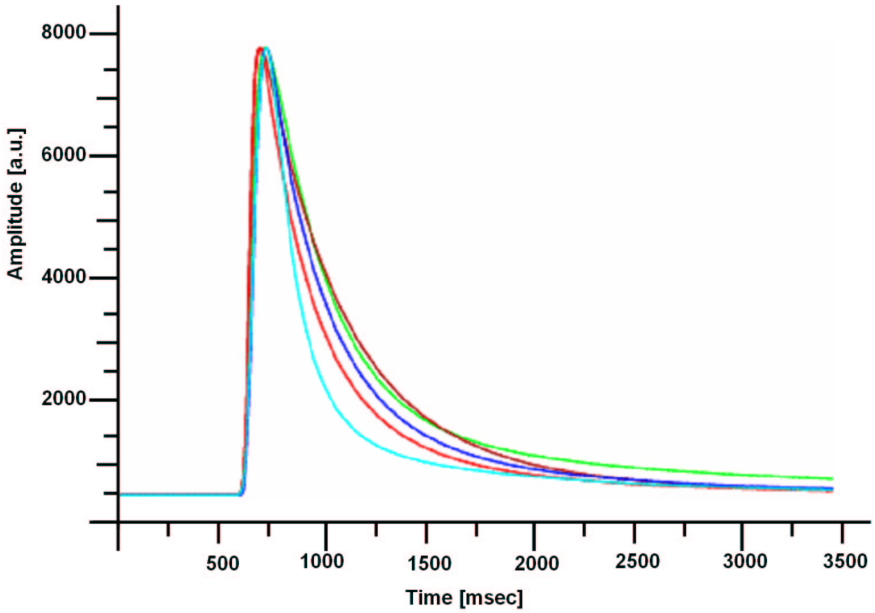

Figure 6.4: Normalized pulses for different detectors in CUORICINO.

and leads to a better data control. Unfortunately the contributions of the various elements of the detector to the time development of the pulse are not well understood. Even though many attempts where done in the past years ([148, 149]), there is still no complete model that can reproduce in detail the dynamic behavior of a detector. Nevertheless all this experience pointed out what are the components that can possibly contribute to the pulse shape. The strategy adopted in this work, that will be detailed in chapter 9, is to try to improve the reproducibility of each of the different components (PTFE, Cu, thermistor, etc.).

6.3.2 Energy resolution

The need for a uniform energy resolution originates mainly from the necessity of summing the spectra from different detectors to get a global analysis of the data.

In fact the template for the expected peak is almost a Gaussian shape, due to resolution effects of the detector. Nevertheless, the sum of all the spectra acquired on different detectors having different resolution can be different from a Gaussian distribution. To avoid this problem one can try to fit the peak with a distribution that is the sum of different Gaussians with different FWHM. The FWHM is the resolution on the peak in the spectrum of each detector.

The experimental setup of CUORE will consist of a large number of detectors (988). This large number of channels corresponds eventually to a large number of different resolutions. This means a large number of different FWHM for the different Gaussian distributions fitting the peak. This spread in resolution can lead to problems in the future global analysis. For this reason some effort was dedicated to improve the uniformity in energy resolution. One of the part of this PhD project (reported in chapter) was the attempt of making TP noise as reproducible as possible on the different detectors to reach a better uniformity in S/N.

6.4 Improving modularity

This task starts as a very simple technical problem: since the assembly and construction of CUORICINO took about six months, if we scale this to a 988 detector is a factor $\sim$16. This necessity matches the possibility of having some non-negligible improvements in the previous two necessities. Finally this originated the new optimized setup presented in chapter 9.

6.4.1 Improving sensitivity

The contribution of a new setup to this topic is in terms of possible background reductions via background sources reduction. This is done mainly reducing the amount of copper present around the detector as will be detailed in sec. .

A further contribution will possibly come from resolution improvements obtained by reducing the sensitivity to noise of each absorber crystal and so the TP noise (see).

6.4.2 Improving detector's behavior

As a secondary result there is the possibility to obtain more reproducible detectors in respect with two different tasks:

- The reduction of TP noise will provide a more uniform distribution of resolution.
- The new structure improves the reproducibility of thermal contacts between different components of the detector (Cu-PTFE, PTFE-crystal, etc.). This means a more uniform distribution of thermal conductances and possible of pulse shapes and decay constants.

More details are reported in chapter 9.

6.5 Experimental setup

All the experimental activity described in the next three chapters was performed in the Hall C R&D facility of the group. In the following I will describe the experimental setup and the equipment used in all the cold tests. Dedicated modifications, if any, will be presented at the beginning of each chapter.

6.5.1 Cryogenic setup

The cryogenic setup consists of an Oxford dilution refrigerator with a power of 200μW at 100 mK.

Inside the cryostat a special damping system reduces the contribution of incoming vibrations to noise. In fact the main sources of TP noise [147] are the vibrations of the overall cryogenic set-up, so that the friction between absorber and supports determines sudden heat spots or unwanted temperature fluctuations. The large spread of harmonic frequencies which are involved in the phenomenon implies a noise spectrum that has a $1/f$ roll-off, and is therefore particularly annoying for bolometers, which have very low characteristic frequencies. That is why the damping system which mechanically decouple the detectors from the cryogenic set-up is so important. In the hall C setup the system is a double stage harmonic oscillator (see Fig.

6.5). The first stage consists of 14 kg Pb disk, with a diameter of 17 cm and a height of 5.5 cm, framed inside a Cu structure. It is mechanically anchored to the cryostat by means of three 4 cm long stainless steel wires, that are connected to the lead through three harmonic stainless steel strips. These strips can slightly bend, resulting in a longitudinal intrinsic oscillation with the frequency of $\sim$ 7 Hz. The choice of the lead was imposed also by radioactivity reasons, since a 5.5 cm thickness of ancient roman lead [150], that is free of ^{210}Pb (a natural radioactive isotope of Pb), acts as a good radioactive shield against the entire dilution unit components. The second damping stage is realized by hanging the detector box to the above mentioned Cu frame of the lead, through a stainless steel spring and a copper bar. The longitudinal intrinsic oscillation frequency of this second stage is $\sim$ 3 Hz. The thermal link between the detectors and the cryostat is ensured by two Cu (99.999 %) thin strips of 50 μm thickness linking the Mixing Chamber (MC) to the first stage, and by a second pair of strips linking the first stage to the detector box.

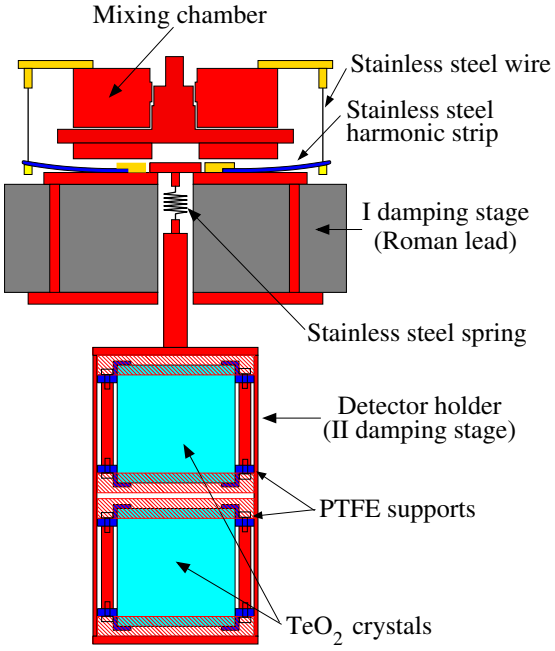

Figure 6.5: The two-stage damping system with a 2 bolometers setup.

6.5.2 Readout of the detectors

The signal is read, from the pins to the MC, with 60 μm dia. constantan wires, in twisted pairs, while 100 μm dia. NbTi wires were used from the MC to room temperature. In the latter case the twisted pairs are also shielded by a CuNi wire netting. Two different front-end systems were used. For one of the 4 thermistors we chose one of the channels available in the cold buffer stage that is thermally anchored at 4.2 K plate, inside the cryostat, while for the other 3 thermistors a room temperature 12-channel front-end was adopted [151]. The cold buffer stage consists of 12 independent differential channels, composed of 12 pairs of silicon JFET transistors in source follower configuration and 12 pairs of load resistors (27+27 GΩ) for thermistor biasing [152]. The operating temperature of about 110 K for this stage is achieved by thermally decoupling

the two printed circuit boards, each of them housing 6 channels, from the box in which they are enclosed by means of nylon wires. The thermal impedance thus achieved guarantees the correct temperature to the FETs when they are working, and therefore dissipating power. In order to avoid any possible irradiation from the circuit boards, the box is gold plated and is as much as possible hermetic to IR rays. The room temperature front-end and the second stage of amplification are located on the top of the cryostat. A big Faraday cage, containing the cryostat, the electronics on top of it, the radioactive shields made of Cu (5 cm minimum thickness) and Pb (10 cm minimum thickness) and the anti-radon plexiglas box, is used to avoid EM interferences to the detector read-out. After the second stage, and close to the acquisition system, there is an antialiasing filter (a 6 pole roll-off active Bessel filter) and a programmable analog triggering and shaping circuit [153]. A small Faraday cage encloses this last stage of amplification. The signals were acquired by a 16 bit ADC embedded in a VXI acquisition system and the data analysis was completely performed off-line.

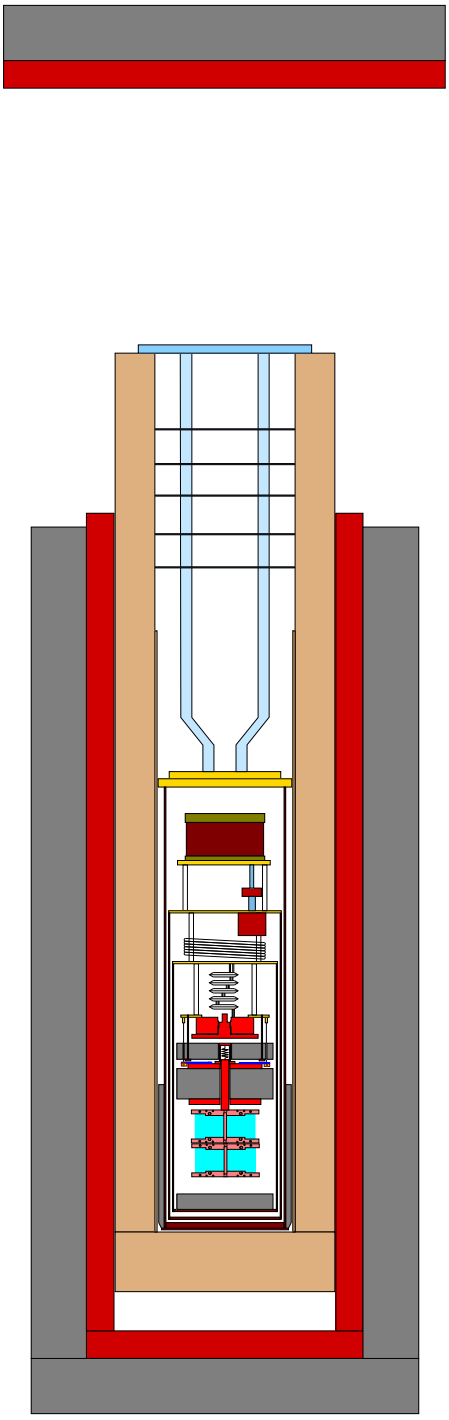

Figure 6.6: The hall C cryostat.

Chapter 7

The $6 \times 6 \times 6$ cm^3 bolometers

In 2004 the possibility of increasing the absorber mass for the future CUORE detector was investigated in Gran Sasso with two cold tests [68]. The results were encouraging, but finally a conservative choice in favour of the old $5 \times 5 \times 5$ cm^3 (0.78 kg in mass) was preferred.

In this chapter I will present the motivations of this test comparing possible advantages and disadvantages. I will then describe the experimental setup and the cold test. Finally I will show the results and comment on the final choice of rejecting the $6 \times 6 \times 6$ cm^3 option.

7.1 Increasing the absorber mass

There are several reasons in favor of an increase of the absorber mass, both scientific and technical. In 2004 we considered the possibility of increasing the mass of the TeO_2 absorber changing from the CUORICINO $5 \times 5 \times 5$ cm^3 (0.78 kg) crystals to a $6 \times 6 \times 6$ cm^3 absorber with a mass of 1,3 kg.

7.1.1 Motivations

The obvious technical advantage is the reduction of the number of bolometers needed for a 1 ton experiment by a factor 1.67, translated in a consistent effort reduction in construction, expense for DAQ chain and in operating and optimizing the detectors. This reason even if purely technical can be non-negligible. In fact, as widely exposed in Chapters 2 and 3, macrobolometers are non-standard detectors which are not produced industrially but require to be assembled by a highly qualified staff.

Gain of sensitivity

There is also a scientific reason in favor of the increase of the absorber mass that is the need of a background reduction exposed in section 6.2.4. In fact, by growing the dimension of the cubic absorber, the surface to volume ratio decreases, thus reducing the contribution of possible surface contaminations to the total background. In CUORICINO's $5 \times 5 \times 5$ we have a volume of $5 \times 5 \times 5 = 125$ cm^3 and a surface of $5 \times 5 \times 6 = 150$ cm^2, that means $S/V = 1.2$ cm^{-1}. In the new $6 \times 6 \times 6$ cm^3 absorber the volume is $6 \times 6 \times 6 = 216$ cm^3 and the surface is again $6 \times 6 \times 6 = 216$ cm^2, that is a $S/V = 1$ cm^{-1}. So being, the mass being proportional to the volume, the

Figure 7.1: A $6 \times 6 \times 6$ TeO_2 crystal (left) compared with the old CUORICINO $5 \times 5 \times 5$ and MiBeta $3 \times 3 \times 6$.

contribution to background of the possible surface contamination in counts/keV/kg/y is reduced of a factor 1.2 (i.e. 83% of the previous value). According to MonteCarlo simulations [134] the contribution of ^{238}U and ^{232}Th radioactive chains contamination from TeO_2 surface to the total background observed in CUORICINO in the $3-4$ MeV region (see sec. 4.3.2) is between 10% and 30% of the total. Thus, the total reduction is 2% and 6% of the total, respectively. Being the value of bkg in CUORICINO of 0.18 ± 0.02 counts/keV/kg/y, the reduction coming from S/V effect can lead to a value between 0.177 and 0.169 counts/keV/kg/y. This, apparently, it is not a big reduction compared to present values. Nevertheless, if we compare this reductions of $\sim 0.003-0.011$ counts/keV/kg/y with the aimed bkg for CUORE, that is 0.01 counts/keV/kg/y, we can see immediately that this contribution is not at all negligible.

One comment must be added about the sensitivity for multi-Compton events in the DBD region. Since the Q value of the 0νDBD of ^{130}Te (2528 keV) is between the ^{208}Tl gamma (2615 keV) line and its Compton edge (2382 keV) the effect of multiple Compton scattering is that of generate events in the region between the edge and the peak. This is measured in the calibration with the ^{232}Th gamma source via the ratio between the intensity of the peak and the continuum background between the edge and the peak for a $6\times6\times6$ cm^3 and for a $5\times5\times5$ cm^3 detector with the same flux of gammas. This measurement shows a slightly badly behavior for the bigger detectors but the effect is almost negligible.

To complete this overview concerning the change of the properties of the detector one should also observe that the heat capacity of the crystal is proportional to volume. As described in section 2.2 the T variation of the detector is proportional to the energy E, released by the incident radiation, divided by the heat capacity C: $\Delta T = E/C$. An increase in C corresponds to a reduction of the measured ΔT for a given energy. Nevertheless, the detector's response (in μV/MeV) is not a good parameter in evaluating the performance (see section 6.2.1) while the best figure of merit for estimating detector's behavior is the energy resolution (or signal to noise ratio) in the operating region of interest. If the dominant noise is thermophononic noise, by increasing the heat capacity then the noise and the signal are reduced in the same way and the S/N is constant. This is presently the case of CUORICINO; a volume increase of 1.728 (signal reduction by the same factor) is assumed acceptable.

Loss of sensitivity

There are also some considerations which disfavor the $6 \times 6 \times 6$ choice but, as we will see, they do not affect the performance of the detector at this level. In fact, the phenomena that can contribute to a worsening of resolution, like trapping of phonons in impurity sites or propagation effects, are typically proportional to the dimensions of the absorber. In the case of phonon trapping, for example, if the impurities distribution is uniform in the crystal the bigger is the crystal, the wider is the distribution with distance of events from the sensor, the bigger can be the energy loss for an event far away from the sensor. This can generate an additional fluctuation on the measured T variation for the same deposited energy and so a spread in the shape of the peak (worst resolution). Anyway, up to now there is no systematic and clear evidence of the contribution of such a phenomenon so we decided to test experimentally the bigger absorbers and compare the results with CUORICINO's.

7.2 $6 \times 6 \times 6$ test

In the early 2004 two $6 \times 6 \times 6$ crystals were bought from the SICCAS Company (Shangai Institute of Ceramics). This is the same company that provided the crystals for CUORICINO. This was the first successful growth of TeO_2 of this large size. The two crystals travelled to Gran Sasso in February 2004 (see figure 7.1). A special holder for the two crystals was designed and built at the LNGS machine shop. More details on this new holder will be given in chapter 9. This was actually a first test of a new design for the copper and PTFE supports.

7.2.1 Experimental setup

Both bolometers had, with an absorber consisting of $6 \times 6 \times 6$ cm^3 TeO_2 crystal, a heat capacity of 2.33×10^{-9} J/K at 8.5 mK, as can be calculated assuming a Debye law with Θ_D= 232 K [115]. The temperature sensors (for redundancy we decided to glue two of them on each crystal) were the usual CUORICINO $3 \times 3 \times 1$ mm^3 NTD Ge thermistors, series #31 [154](see Fig. 7.2). They are thermally coupled to the absorber with 9 spots of epoxy glue of $\sim$ 0.6 mm diameter and $\sim$ 50 μm thickness. In order to correct for thermal instabilities [146] a Si resistor is attached to each crystal with 1 single spot of epoxy glue and is used as a heater. Each crystal is fastened to a Cu frame by means of 8 S-shaped PTFE supports that hold it in each corner of two opposite faces (see Fig. 6.5). The two independent bolometers are assembled one on top of the other and covered with Cu plates, to form a single box, which is then fastened to the dilution unit of the cryostat through a two-stage damping system, as shown in Fig. 6.5.

7.2.2 Measurement

The measurement was divided in two different cold runs with the same setup. Each run consisted of about 12 days of data taking was preceded and followed by a calibration. The calibrations were performed with the usual ^{232}Th gamma source currently used in CUORICINO (see sec. 4.1.1). Unfortunately, the first measurement was affected by severe apparatus problems so the collected data didn't give conclusive answers. The most relevant problem was related to the impossibility to reach temperatures lower than 14 mK. This avoided the comparison of the new detectors with the CUORICINO ones at in the same conditions. For this reason the results

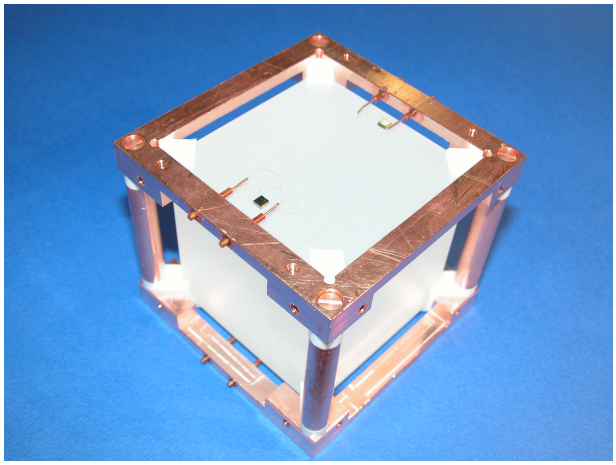

Figure 7.2: A $6 \times 6 \times 6$ TeO_2 crystal (left) compared with the old CUORICINO $5 \times 5 \times 5$ and MiBeta $3 \times 3 \times 6$.

	$L1\#1$	$L1\#2$	$L2\#1$	$L2\#2$
$R\ [M\Omega]$	244 (95)	163 (41)	272 (107)	142 (83)
Signal [μV/MeV]	200 (104)	109 (44)	265 (148)	136 (62)
T^{rise}(10-90)% [ms]	86 (75)	90 (74)	82 (68)	74 (65)
T^{decay}(90-10)% [ms]	170 (194)	244 (275)	150 (168)	234 (249)

Table 7.1: Main properties of the detectors at the two different holder working temperatures T_{base}= 7.3 mK (T_{base}= 8.8 mK).

presented below refer only to the second of the two cold test. A second problem showed up in the first cooling down: many of the corner crystal brook. The analysis and solution of this problem is reported in Chapter 9.

7.3 Analysis and results

During the entire run, that lasted $\sim$12 days, we observed the crystal holder cooling down following an exponential law. This behavior probably originated from the slow ortho-para conversion of the molecular hydrogen trapped in the copper elements of the detector holder [119]. This effect is a common problem that arises in cryogenic setups when a mechanical decoupling from the cryostat (which acts also as a thermal decoupling) is introduced. A compromise between the best thermal conductance and the minimum mechanical coupling must be found. This was achieved using the Cu stripes [155] described before, decoupling the MC from the first stage and the latter from the detector's holder. In our case the smallest conductance was between the MC and the first stage, and was measured to be (2.8$\pm$ 1.2) 10^{-5} W/K at 8 mK. The base temperature T_B on the detector holder, reached after 6 days, was $\sim$ 7.3 mK. We measured the performances of the two detectors at two different holder temperatures: T_B=7.3 and T_B=8.8 mK. The corresponding main properties of the two bolometers (L1 and L2), as read by the two

	583 keV	911 keV	2615 keV	O.F. keV
L1#1	3.3 ± 0.3	3.9 ± 0.4	3.6 ± 0.6	2.4
L2#2	3.4 ± 0.3	3.5 ± 0.4	4.2 ± 0.6	2.5

Table 7.2: FWHM resolution (keV) obtained with the two bolometers. The baseline widths, after Optimum Filtering, are shown in the last column.

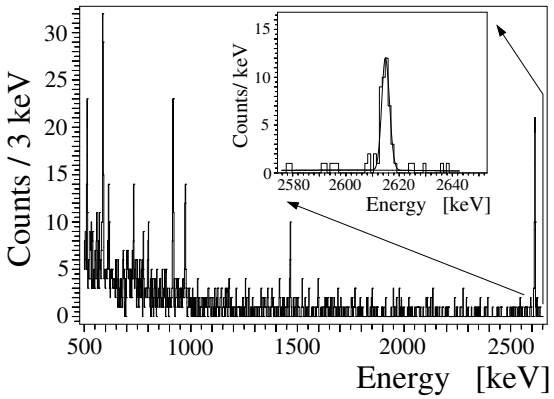

Figure 7.3: Calibration spectrum in the γ-ray energy region obtained with one detector exposed for 25 h to a ^{232}Th source . The peak at 2615 keV of ^{208}Tl, magnified in the inset, shows a FWHM resolution of 3.6 keV.

thermistors (#1 and #2), are summarized in Tab. 7.1. The thermistor L2#2 was the only one acquired through the cold buffer stage. The energy calibration was performed using a ^{232}Th γ-ray source placed outside the cryostat. The energy resolutions FWHM obtained with the two detectors are summarized in Tab. 7.2. The thermistors mounted on the same crystal showed only slight differences ($\leq$ 20 %) in energy resolutions, probably due to the different microphonic noise coming from the different read-out wires, while the results obtained with the same thermistor at the two T_B were equal within the statistical error. The energy dependence of the resolution is surprisingly very loose, respect to the usual behavior of real calorimeters. The calibration spectrum obtained with the L1#1 detector is shown in Fig. 7.3. A very good result was obtained for the α line at 5407 keV due to the internal contamination of ^{210}Po, a common impurity in Te-based materials [150]. We obtained 4.3 ± 0.4 keV with L2 (see Fig. 7.4) and 5.0 ± 0.5 keV with L1. These results were obtained without any temperature stabilization of the detector holder, which was slowly cooling down during data taking. This probably caused a slight asymmetry on the full energy peaks, that smeared the energy resolution.

If one tries to evaluate the deviation from linearity of the detectors, expressed as $\Delta L\% = (E^{expected} - E^{measured})/E^{expected}$, where $E^{expected}$ is obtained assuming a linear response of the detector calculated from the lowest calibration line (583 keV) with no offset, an evident dependence from energy shows up, as can be seen in Tab. 7.3. This can be explained by the changes of the thermal parameters of the detectors during the evolution of the signal: the temperature increase due to an energy release in the absorber is small, but finite, with respect to the working temperature.

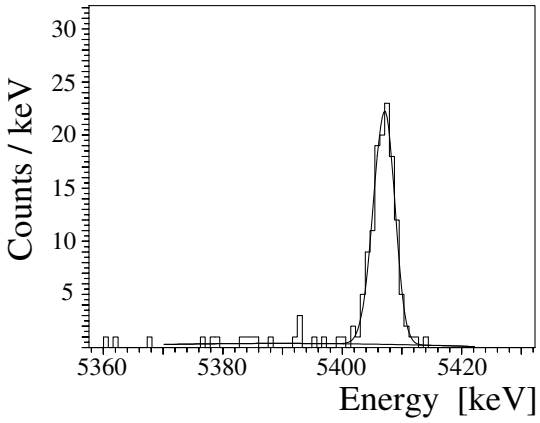

Figure 7.4: The α peak of ^{210}Po at 5407 keV

	$L1\#1$	$L1\#2$	$L2\#1$	$L2\#2$
ΔL [%] @911 keV	0.2 (0.5)	0.1 (0.1)	0.3 (0.4)	0.2 (0.2)
ΔL [%] @1461 keV	0.5 (1.0)	0.4 (0.8)	0.9 (1.0)	0.4 (0.3)
ΔL [%] @2615 keV	1.0 (2.2)	0.5 (1.5)	2.0 (2.2)	0.7 (0.6)
ΔL [%] @5407 keV	1.5 (3.8)	0.4 (2.3)	3.6 (3.9)	0.6 (0.6)

Table 7.3: Deviation from the linearity of the detectors at the holder working temperature of T_{base}= 7.3 mK (T_{base}= 8.8 mK) normalized to the 583 keV γ-line of ^{208}Tl

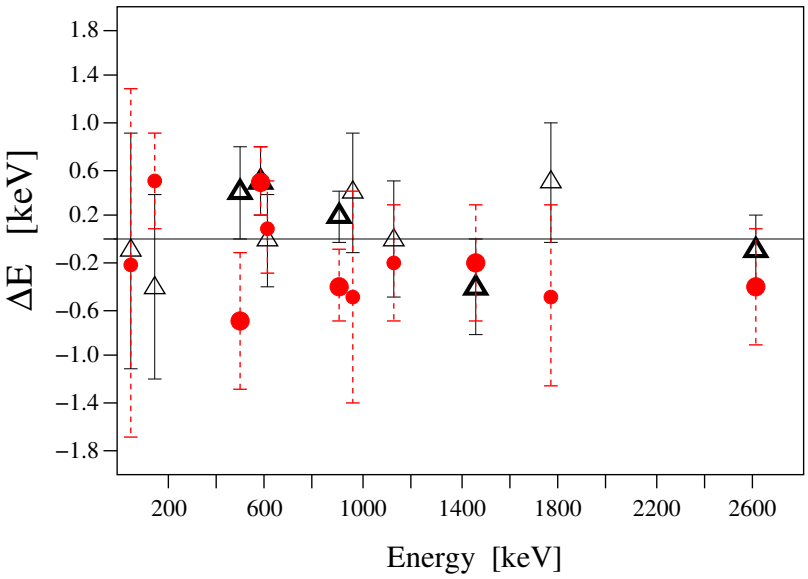

Figure 7.5: Deviation between the reconstructed energy and the nominal values for L1#1 (circle) and L2#2(triangles). The symbols in bold represent the γ lines used for the linearization fit.

This causes a non-linear energy response of the detector. Fitting with a polynomial it came out that the non linearity can be well described by an empirical quadratic form, $E = ax + bx^2$, where x represents the signal in mV. On the contrary, the differences within the same crystal and between the two working temperatures can be ascribed to the different working points of the thermistors, chosen in order to maximize the S/N ratio.

The linearization fit was calculated including only the most intense lines of the calibration spectrum: 511, 583, 911, 1461, and 2615 keV γ-lines. The corresponding energy of all the lines appearing in the spectrum was then evaluated. The deviation between the reconstructed energy and the nominal value of each identified peak is shown in Fig. 7.5. As it can be seen, the energy reconstruction in the γ region is better than $\simeq 0.6$ keV, showing that the non-linearity of the detector is well under control.

In many rare event searches the low threshold is essential. Therefore, to evaluate it, the low energy region of detector L2#2 background spectrum was studied. This channel, being the only one read through the cold buffer stage at 4.2 K, showed in fact a less pronounced thermophononic and microphonic noise, which can worsen the threshold level. A 12 hour measurement was performed with the threshold set at 12 keV, applying a pulse shape analysis [156] to discriminate noise from physical pulses. A typical low energy pulse from L2#2 detector is shown in Fig. 7.6.

7.4 Conclusions

It is the first time that two bolometers heavier than 1 kg show energy resolutions similar to those obtained with Ge diodes. In the Neutrinoless Double Beta Decay region for ^{130}Te (2528.8 keV) the obtained energy resolution is better than the mean energy resolution of the CUORICINO

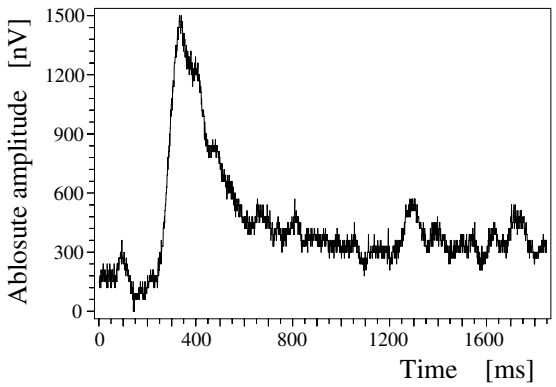

Figure 7.6: Typical low energy pulse of L2#2 detector without amplification, corresponding to a deposited energy of 18 keV.

experiment, which is 8 keV. This was achieved thanks to the improved holder design and to the two-stage damping system that minimize the noise induced by the vibrations of the cryogenic apparatus. Thresholds could be certainly improved with less microphonic read-out wires, but this was not our main goal, at least during this test.

The statistic on different detectors is not very high of course, but the good agreement between the two detectors is a good indication of reproducibility.

The information we can certainly get is that there is a future for large macrobolometers as rare events detectors, even bigger than 1 kg. This, of course, needs to match with the possibility of growing crystal so big. Probably more R&D is needed on these detectors.

After some investigation the CUORE collaboration decided not to include the "6×6x6" option in the experiment project. This was done mainly for two reasons. The first is that the indication of the detector's behavior described in this chapter are not conclusive in respect to the possible secondary effects due to the new absorbers. The second reason is that the experimental volume in the R&D setup of hall C does not allows to test a four detectors module without dramatic modifications of the setup. This modifications are not compatible with the CUORE time schedule.

Finally this test remains as a window on future applications for rare events physic with very large mass detectors.

Chapter 8

Reducing radioactivity

In this chapter I will present the second R&D activity developed during my PhD work, that is the reduction of the background for improving the sensitivity (as exposed in sec. 6.2.4). Two experimental tests, Rad1 and Rad2, were performed in the Hall C cryostat during 2004 and 2005. This was a very important R&D activity in view of CUORE. In fact only background reduction can improve the sensitivity to reach the desired level (see sec. 6.2.4).

The results presented in the following show that we have built and operated one of the most radio-clean detectors ever built and that we completed at least one of the two main goals of the CUORE background reduction program.

8.1 Physical goal

The Q of the ^{130}Te 0νDBD (2528 keV) focus our attention for the energy region between the gamma line of ^{208}Tl at 2615 keV and its Compton edge (2382 keV). In the CUORICINO spectra one can observe that, away from the peaks, we have a more or less flat and continuum background in the 0νDBD region. This is not a peculiar property of the 2.5 MeV region but is characteristic of all spectrum between the ^{208}Tl and the alpha peaks (above 4 MeV), a region where natural radioactivity background is not present.

Starting from this experimental evidence, the origin of the background was suggested to be due to degraded alpha particles, that is alpha particles coming from decays near the surface escaping from the crystal before releasing all their energy. Two different processes are considered: alpha decays in the crystal near the surface, and alpha particles escaped from the surface of some other component of the detector impinging on the crystal, respectively. In the first case the alpha particle releases part of its energy in the absorber and then escapes and releases the remanent energy on a different part of the detector (another crystal, the holder, the external shields, etc.). In the second process the alpha particle hits the crystal coming from a different source and having already lost part of its energy in the source material.

The worst scenario is when one of the two objects hit by the alpha particle is not an active material (that is everything but the absorber and the thermistor). In fact, as pointed out in chapter 5, one of the main improvements of the CUORE structure is the optimization of the coincidence technique for background selection and rejection. The fragmentation of the final detector maximize the surface of the crystal faced to active material (other crystals) allowing the possibility of selecting two events in time coincidence on different crystals and rejecting

both (or eventually reconstruct the original energy summing the two energies). Unfortunately there is still a non negligible fraction of the total surface that is faced to non active material, that can contribute dramatically to background (more comments on this will be presented in the next chapter).

Presently the best candidates for the role of source of this background are copper and TeO_2 crystals, because they are by far the most abundant materials inside the detector. The main goal of these runs was to reduce the surface contamination of the crystals and copper frames. For this reason both chemical and mechanical procedures were developed and performed.

8.1.1 Physical approach

The main problem in preparing a test for very low rate contamination is the low statistics. In fact in CUORICINO we have a background in the 0νDBD region of 0.18 counts/keV/kg/year. This means that, if we consider a 50 keV region and a total mass for the R&D setup of $\sim$ 6.24 kg (8 detectors), we will have 59.28 counts/year that is $\sim$ 0.16 counts/day. To measure the background with a precision of 10% we will need 100 counts, that means 625 days of live time of the detector. Considering that we are interested in reducing the background contaminations at least by a factor of 10, we will never be able to test the contamination in the 0νDBD region.

There is an important physical assumption that can help us in evaluating the background, that is that the source of background are the degraded alpha particles. The degraded alpha processes produce, as we have already noticed, a continuum of events starting from the alpha region ($\sim$ 4 MeV) down to 0. If this is the main contribution to background, it is not necessary to evaluate it in the physical region of interest but we can choose any other region wide enough and free from other radioactive contributions. This chosen region is actually the 3-4 MeV region, that is between the highest natural gamma peak and the alpha region.

Measuring background events in the 3-4 MeV region, instead of the 0νDBD region, increases the sensitivity by a factor of 20. This means that about 1 month of live time is needed to reach a 10% sensitivity if the background is the same like in CUORICINO. In this way, if reduce the background by a factor of 10 we will measure the contamination in $\sim$ 3 months of live time, with an error of $\sim$17%.

Finally, evaluating the number of events in the 3-4 MeV region we can extrapolate the contribution of degraded alpha particles to the background in the 0νDBD region. A big reduction of events in this region can confirm the capability of reducing background in the region of interest.

8.1.2 CUORE background reduction program

The background reduction program of the CUORE experiment [157] started from the estimation of the different contributions to the CUORICINO background (0.18 $\pm$ 0.02 c/keV/kg/y) and from the minimal goal for the background of CUORE (0.01 c/keV/kg/y). As pointed out in sec. 5.3.3, the contribution of degraded alpha particles in the 0νDBD region from Cu surface is estimated, via MonteCarlo simulations, to be $\sim$ 50% $\pm$ 20%. This means that we have between 0.05 and 0.13 c/keV/kg/y coming from Cu surfaces. This contribution must be reduced to 0.005 c/keV/kg/y. We get a reduction by factor of about 36.

8.2 The Rad1 setup

The goal of this measurement was to clean all the surfaces of the detector and to test the result. The guideline for the preparation of the setup was to try to control all the cleaning processes and the handling of the detector trough the entire assembly and preparation of the detector.

The test was performed on 8 bolometers (two CUORICINO modules) assembled in two superimposed modules of 4 detectors each (see Fig. 8.1). Half of the detectors were also provided with a second thermistor for redundancy. The temperature of the detectors' copper holder was stabilized via a heater and a feedback circuit [146].

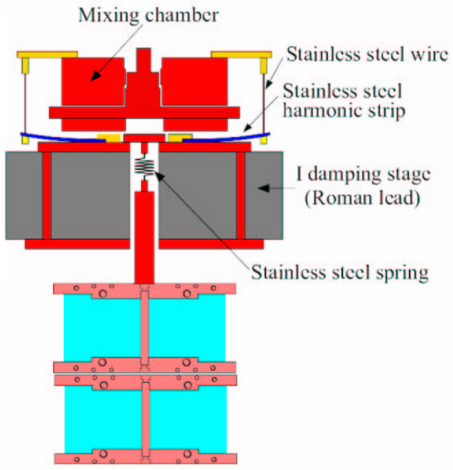

Figure 8.1: The Rad1 experimental setup inside hall C cryostat.

8.3 Surface cleaning

The best way to fix a cleaning procedure is to use only a few radioclean materials and to minimize the number of cleaning steps. Two important rules were followed: to use only radiopure cleaning materials (acids, lapping powders, etc...) and, to prevent the detector parts or the cleaning materials to be in contact with any kind of not-clean material, respectively. The work was subdivided in two parts: crystal surface cleaning and copper surface cleaning. The main common task to start these activities was to select a decontamination procedure for the containers where to perform the washing and acid attach. PTFE vessels were used for crystal etching and polyethylene pots for copper cleaning. Each material was selected and measured during the past 2 years in the Gran Sasso National Laboratory facilities using different techniques : the High Purity Germanium (HPGE) detectors and the Inductively Coupled Plasma Mass Spectrometry (ICPMS) tool.

8.3.1 Container cleaning

The cleaning of the vessels was performed into a ultrasonic bath with a series of washing and rinsing procedures with ultrapure water (18 MΩ/cm) and different soaps. The various steps are

reported in Tab. 8.1. After the treatment, the vessels were stocked in double sealed double layer

Treatment	Solution	Temperature [°C]	Time
washing into ultrasonic bath	5 % micro 90 basic soap	40	30 min.
rinsing	ultrapure water	room T	
washing into ultrasonic bath	5 % of Elma 60 Acid soap	40	30 min.
rinsing	ultrapure water	room T	
vessel filled	ultrapure water	room T	1 week
rinsing	ultrapure water	room T	
washing into ultrasonic bath	5 % of Superpure HNO3	40	3 weeks
rinsing	ultrapure water	room T	
washing into ultrasonic bath	5 % of Superpure HNO3	40	3 weeks
rinsing	ultrapure water	room T	

Table 8.1: Vessels cleaning procedures. The solutions are always intended in ultrapure water. In the long time cleaning the ultrasonic bath is used only during the day for safety reasons.

plastic bags in nitrogen atmosphere.

8.3.2 Crystal surface cleaning

From all the sources, the crystal surface contamination is the one we have a better understanding about. The crystal, being an active part of the detector, any time a radiation passes trough it (e.g., an alpha particle), it is detected. The observed shape of the background and the rate of coincidence events of the CUORICINO detector indicate the presence of events coming from the crystal surface. The number of these events is not compatible with the measured bulk contamination coming from the ^{238}U and ^{232}Th radioactive chains. The bulk contamination of the crystal measured in CUORICINO are at a level $<0.7\cdot10^{-12}$ g/g for ^{232}Th chain and $< 0.1\cdot10^{-12}$ g/g for ^{238}U chain. For $5 \times 5 \times 5$ cm^3 crystal (0.78 kg) we have that the background in the 0νDBD region is $0.18 \times 0.78 = 0.14$ c/kev/y. For the same crystals the contribution of degraded alpha particles is calculated (via MonteCarlo simulations) from the measured limits to be of the order $<10^{-3}$ counts/keV/kg/y. This means that if the contribution of degraded alpha particles is the dominant contribution, there is an excess of contaminants near the surface of the crystals. This is reasonable since the crystals were cut and polished and lapped after being grown.

For this reason we developed procedure of surface cleaning. The idea is very simple and it is based on the previous experience of the group. Two different ways to clean crystal surfaces were tested previously, both with advantages and disadvantages: etching the crystal with nitric acid or polishing and lapping mechanically.

The first one is very easy to perform, requires only to use clean materials and usually gives very good results. This procedure was abandoned before CUORICINO due to the strange behavior of the detectors treated in this way. The response in pulse shape of the bolometers with etched absorber was quite different from the usual having a very long decay time. This is probably due to the fact that the solution of acid creates a layer of molecules on the surfaces of the crystal. This in the operating the detector constitutes an additional thermal interface that changes the response. This is a well known problem in etching crystal surfaces. It is usually

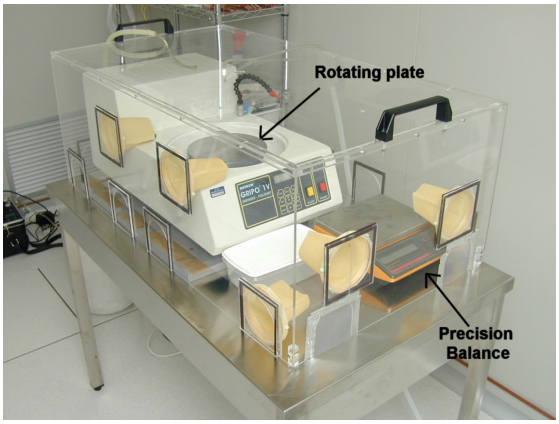

Figure 8.2: Lapping Machine

avoided by worming up the crystal in a pumped volume. Unfortunately warming up TeO_2 crystals of big dimensions is not easy because of unevenly distributed temperatures that can make them break.

The second way, i.e. mechanical lapping and polishing, is another well known technique in crystal processing and it is actually the origin of the surface contaminations in TeO_2 . The lapping tool is very simple (see Fig. 8.2): it is a rotating wheel on which an abrading pad is fixed. The standard technique consists in pouring a solution of water and lapping powder on the wheel and then press the crystal on it. The friction between the pad, the powder and the crystal removes material from the surface of the crystal. This procedure was successfully adopted in CUORICINO. The limitation of this technique is that the material removed from the surfaces, that contains the radioactive contaminants, remains for some time on the wheel and due to the friction can be mechanically diffused again inside the crystal. The success of this technique is confirmed by the CUORICINO data, in which a reduction of a factor two is observed.

To prepare a new setup a simple idea was followed, that is to combine the two techniques using radiopure materials. The crystals were first etched to remove the radioactive contaminants and then lapped to remove the layers of acid on the surface. In Tab. 8.3 the measured values for the used materials are reported, both for etching and lapping, compared with CUORICINO values.

Crystal etching

The first step is to chemically etch the crystals in an ultrapure nitric acid solution. The chosen molarity is 4.5; the time of etching is 4 hours at room temperature. These parameters were chosen to remove a layer on all the surface of about 10 μm and the longer time of attach guarantees a good uniformity. After the etching, crystals were rinsed with water and dried with nitrogen. In Tab. 8.2 are reported the removed values for 8 crystals. The mean etched surface is $\sim$ 9.4 μm.

Crystal	In Weight [g]	Fin Weight [g]	ΔWeight [g]	ΔL [μm]
B2	766.78	766.06	0.72	7.6
B8	788.40	787.50	0.90	9.5
B11	788.39	787.41	0.98	10.3
B22	799.73	798.93	0.80	8.5
B4	761.09	760.17	0.92	9.7
B5	811.30	810.23	1.07	11.3
B19	801.53	800.57	0.96	10.1
B20	800.28	799.45	0.83	8.8

Table 8.2: Results of the chemical attach on 8 crystals of TeO_2 .

	238U [10^{-9} g/g]	232Th [10^{-9} g/g]	40K [10^{-9} g/g]	Technique
Demineralized H_2O	<0.0005	<0.002	—	ICPMS
Ultrapure HNO_3	<0.0005	<0.002	—	ICPMS
SiO2 Powder	<0.032	0.1	<0.03	HPGE
Al2O3 (CUORICINO)	<1.5	40	<0.4	HPGE
Lapping Pad (Buehler)	<1	2.2$\pm$1.2	2.1$\pm$0.2	HPGE
Lapping Pad (CUORICINO)	3.1$\pm$0.9	10.3$\pm$2	3.1$\pm$0.3	HPGE

Table 8.3: Radioactive contamination of different Surface Cleaning materials for crystals, compared with CUORICINO values.

Crystal polishing

The second step in crystal surface processing consisted in lapping all the surfaces. I already described the lapping machine that was used in CUORICINO. We chose a new powder and different cleaning pada: a rougher lapping pad (a Nylon pad of 10 μm from Buehler) and a finer lapping powder (SiO_2, particle size 1.3 - 2 μm). After some test we chose the percentage of SiO_2 40 - 60% of water (in weight). The different behavior of hard and soft surfaces was also taken into account. In order to remove the same amount of surface, an appropriate time was chosen: 20 minutes for hard faces and 5 minutes for soft faces, respectively. The mean removed surface was $\sim$ 11 μm.

8.3.3 Copper surface cleaning

Similar considerations can be done for copper bulk and surface contaminations. Obviously, copper was also mechanically machined after production.

The procedure of cleaning the copper was more difficult for different reasons. First of all the shape of Cu frames is quite complicated and so one should be very careful in checking that all the surface is cleaned in the same way. A second big problem is that Cu is quite reactive to oxidation: this means that after cleaning the surface starts to oxidize. During this process other kinds of contaminants present in air can be trapped on the surface. To prevent this the

copper must be passivated. The most common passivation technique to do this is to treat the surface with citric acid ($C_6H_8O_7$). After several tests we decided to divide the cleaning process into 3 steps: 1) rough cleaning, 2) Etching and 3) Electroerosion. In Tab. 8.5 the measured contaminations of the different materials used during all the procedures are reported.

Rough cleaning

The first part of the procedure is developed to remove mainly the contaminations coming from the machining of the copper, like machine oil and grease and eventually other dirt present on the surface. The best way to remove external material (not copper nor implanted contaminants) is to wash the copper in ultrasonic bath with some soap.

Thus, the first step was to wash in ultrasonic bath with a ultrapure water (18 MΩ/ cm) and 5 % of Micro 90 basic soap at a temperature of $\sim$ 40 Celsius for 1 hour. After being rinsed with ultrapure water the frames were again washed in ultrasonic bath with a ultrapure water and 5 % of Elma 60 Acid soap at a temperature of $\sim$ 60 Celsius for 1/2 hour. Then the copper was rinsed with ultrapure water and finally passivated with a solution of 10% citric acid at 60 Celsius for 1 hour. At the end the pieces were cleaned and dried with alcohol and clean room papers.

Etching

The second step removes a layer of Cu from surface to eliminate the contaminations implanted inside during the machining. This is done by etching the copper pieces in a solution of 0.5 Molar Ultrapure nitric acid in ultrasonic bath at 40 Celsius for 1/2 hour. The frames then were rinsed with ultrapure water and passivated again in a solution of 10% citric acid at 60 Celsius for 1 hour. Finally, all the copper was rinsed with ultrapure water and dried with nitrogen. The mean etched surface of copper after this second step was $\sim$ 5 μm, extrapolated from the weight difference and the surface area.

Electroerosion

The final step, copper electroerosion completed the removal of material from the surface (eliminate implanted contaminants) and, at the same time, applied the final passivation to the frames. The advantage of this technique is that, using the appropriate electrolyte, this method is very simple and can be completely controlled. The possible disadvantage is the surface roughness obtained after the treatment, much more than in CUORICINO final frames. This can increase the capability of the surface, even if passivated, to collect dirty material after the treatment and partially destroy the result of the cleaning effort. To minimize this effect we kept the frame always in clean boxes and in nitrogen atmosphere, handling everything with the proper clean gloves.

The electrerosion setup (Fig. 8.3) is constituted by two electrodes immersed in an electrolytic solution. One of the electrodes is the copper frame itself while the other is shaped in a way that guarantees the best facing and uniformity in the attach. These two were immersed into an electrolytic solution of citric acid (10%) in ultrapure water. Considering the weight before and after for each piece, together with active surface faced to the cathode mask, the amount of removed material was evaluated as reported in Tab. 8.4.

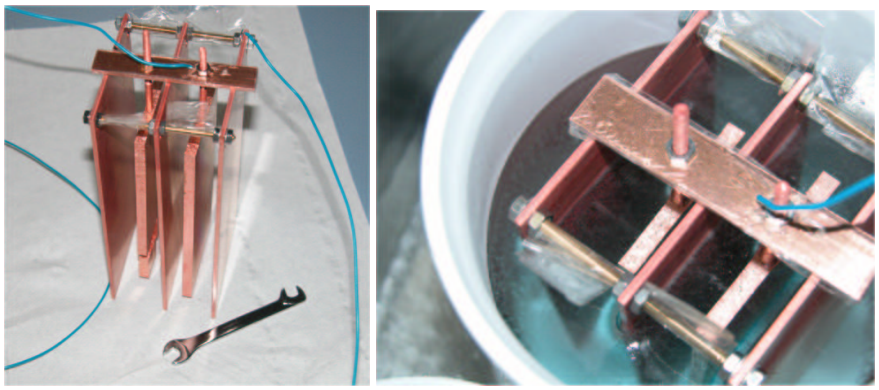

Figure 8.3: The electrerosion setup: the catod and the anod are connected to a current supplier that provides a current of $\sim$ 1 Amp/50 cm^2. In the picture the test setup with a rectangular sample of copper to be cleaned.

	$\Delta L_{electro}$ [μm]
Frames (4)	25
Lateral bars (2)	30
Lateral covers (2)	15
Top and Bottom cover	30

Table 8.4: Material removed via electroerosion for the different copper pieces: average on the number of pieces of the type (reported in parenthesis). Deviations from the average are less than 2 μm.

After the electroerosion each piece was rinsed with ultrapure water an passivated again in a citric acid solution with O_2 bubbling. Then the pieces were rinsed again with water, dried only with nitrogen and enclosed in plastic bags filled with nitrogen.

8.4 Analysis and result

The final tower of 8 detectors was cooled down inside the hall C experimental facility in late August of 2004. The data is divided into 4 runs that differ one from another by minor changes in the stabilization system. One channel (crystal B19) and one heater (on crystal B22) were lost during the cooling down of the cryostat (contact or wire broke due to the thermal contractions). An external 10 cm lead shield was added between Run I and Run II. Each run consists in a set of data with a calibration to linearize the spectrum. The heaters power was tuned to stay in the range between 1700 and 2100 keV and not in the usual 6 MeV region to prevent degraded heater pulses to appear in the 3-4 MeV region and distort measure results. The detector without heater (B22) was stabilized on 2615 keV gamma line in Run I and on the 5.3 meV alpha line in the following runs in which the gamma events are suppressed by the additional lead shielding. The total measurement time (background data taking) was about 1125 h (about

	238U [10^{-9} g/g]	232Th [10^{-9} g/g]	40K [10^{-9} g/g]	Technique
Elma 60	430	0.8	—	ICPMS
Micro 90	4.9	4.4	—	ICPMS
Rodastel soap (CUORICINO)	5.6	0.4	—	ICPMS
GP17-40 SUP soap (CUORICINO)	208	7.1	—	ICPMS
Citric Acid (pure)	<0.024	<0.14	<0.1	HPGE
Citric Acid (10% solution)	<0.0005	<0.002	—	ICPMS
Demineralized H_2O	<0.0005	<0.002	—	ICPMS

Table 8.5: Radioactive contamination of different Surface Cleaning materials for copper, compared with CUORICINO values.

47 days) acquired during 3.5 months. In the final analysis the detector B22 (the one without heater) was excluded because of some linearization problem. The total statistics is [0.13 y]·[6 (number of channels)]·[0.78 kg (weight of each detector)] = 0.6 kg·y.

8.4.1 Background analysis

The analysis of the data is done mainly comparing the sum spectrum of the 6 channels of the Rad1 array with the CUORICINO data. To have a better comparison for the background coming from copper we decided not to use all the CUORICINO data but only those coming from the top and bottom planes (Btb spectra). In fact most of the CUORICINO 4 detector modules are located between two other modules while the Rad1 modules have one of the two horizontal faces faced to the external copper cover. The same situation is present in the CUORICINO top and bottom modules. For this reason the comparison is with the summed top and bottom spectrum is the most relevant.

The different contamination contributions in the different energy regions can be summarized as follows [158].

- **Gamma region**: the comparison is not very significant due to the different shielding of CUORICINO with respect to the hall C. The addition of the Lead shield gives a reduction by a factor of about 1.5 in the whole spectrum rate. In the hall C spectrum the heater peaks are visible in the energy region between 1.7 and 2.1 MeV (see Fig. 8.5).

- **DBD0n region**: in the hall C the rate in this region is higher. This is in agreement with the higher intensity of the 2615 keV peak> 3.8$\pm$0.4 10-2 counts/h in respect to 0.71$\pm$0.03 10-2 counts/h of CUORICINO (about a factor of 5 higher in hall C). The 2.6 MeV peak is reduced in the hall C by a factor 1.5 after increasing the lead shield.

- **Region 2700-3200 (continuum)**: the rates measured in hall C are compatible with those of CUORICINO.

- **Region 3400-4000 (continuum)**: reduction by a factor of about 1.8$\pm$0.3 with respect to the Btb CUORICINO spectrum.

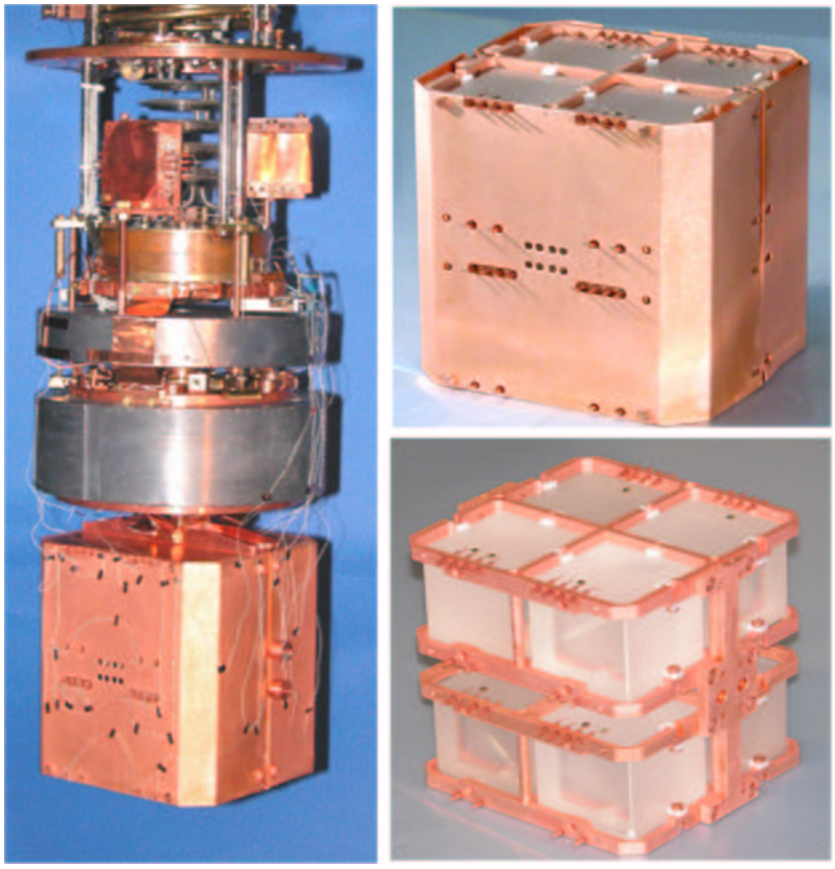

Figure 8.4: The Rad1 detector connected to the hall C cryostat (right). On the left the 8 detectors at two different stages of the assembly.

- **Region 4000-4350**: (containing the peaks of ^{232}Th and ^{238}U) reduction of the counting rate by a factor of about 2.0$\pm$0.3 with respect to the Btb CUORICINO spectrum (see Fig. 8.6). In the hall C spectrum it is clearly visible the ^{232}Th peak at the transition energy (4104 keV). This corresponds to a decay occurring in the crystals. In addition the peak has a gaussian shape indicating a bulk contamination. In the same region in the CUORICINO spectrum a structure that can be ascribed ^{238}U is visible. The non-gaussian shape and the existence of coincidences in nearby crystals give indications of surface ^{238}U contaminations of the crystals. For the hall C sum spectrum the approximated values are: 0.003 $\pm$ 0.001 counts/h for the line $\sim$4104 keV and $<$ 0.004 counts/h for the ^{238}U "structure". For CUORICINO Btb the values are: 0.0018 $\pm$ 0.0007 counts/h for the line $\sim$4110 keV and 0.017$\pm$0.005 counts/h for the ^{238}U "structure". The U surface contamination seems to be reduced by a factor of about 4 with respect to CUORICINO.

- **Region 4350-4600 (continuum)**: the rates measured in the hall C are compatible with those measured in CUORICINO.

- **Region 4600-4950**(containing the peaks of ^{234}U, ^{230}Th and ^{226}Ra of the ^{238}U chain):

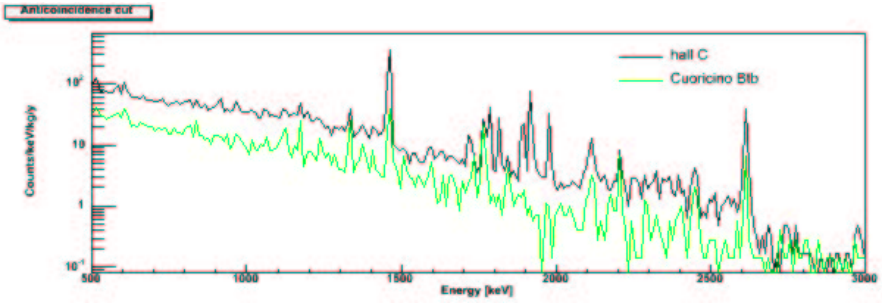

Figure 8.5: Comparison between CUORICINO and Rad1 spectra in the region between 500 keV and 3 MeV.

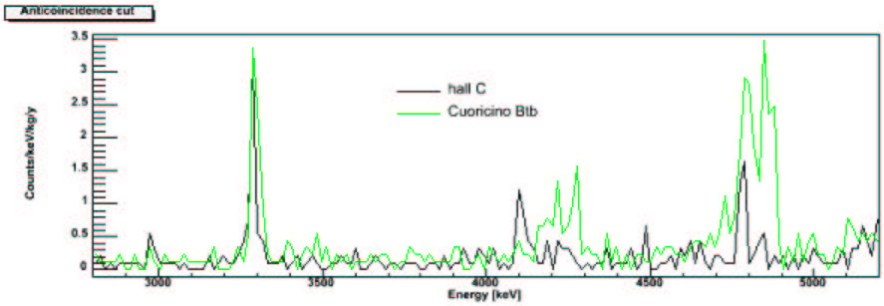

Figure 8.6: Comparison between CUORICINO and Rad1 spectra in the region between 3 and 5 MeV.

in the hall C spectrum only a gaussian peak at 4774 keV is visible (bulk 230Th?). In CUORICINO is visible a structure that could be ascribed to the sum of a bulk ^{230}Th and a surface ^{238}U contamination. The integral is reduced by a factor of 3.8$\pm$0.5. The hall C measurements seem to give indications of crystal bulk contamination in Th out of secular equilibrium. Only the long living Th isotopes from both chains seem to have survived. Added to this internal contamination a U surface contamination (clearly evident in CUORICINO) in secular equilibrium is present. In hall C it is only possible to evaluate upper limits for this contamination. Nevertheless a reduction by a factor of about 4 with respect to CUORICINO can be evaluated.

- **Region 4950-5200 (without peaks)**. In this region no peak is present. A tail of the 5.3 MeV Po peak is instead a possible source for the background in this region. A reduction factor of about 3.3$\pm$0.6 is observed. This reduction can not be ascribed to a reduction of the 5.3 MeV peak, since in hall C the peak is higher than in CUORICINO.

- **5.3 MeV peak**: its intensity (see Fig. 8.7) is higher in the hall C measurement (by a factor of about 2). In the coincidence spectra (Fig. fig:R1Q5-6coinc:RedRad), both for hall C and CUORICINO, the 5.3 MeV peak is visible, this indicating that at least part of the contamination responsible for it must be on the crystal surface.

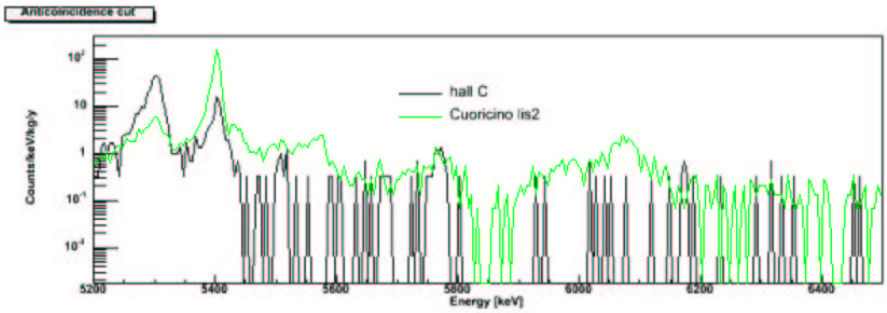

Figure 8.7: Comparison between CUORICINO and Rad1 spectra in the region between 5 and 7 MeV.

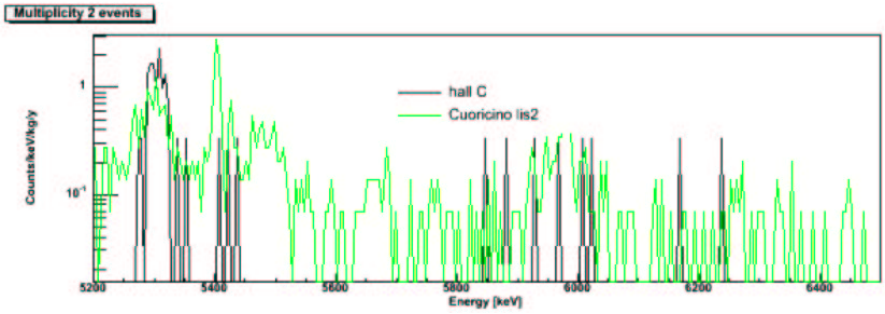

Figure 8.8: Comparison between CUORICINO and Rad1 multiplicity 2 events spectra in the region between 5 and 6 MeV.

- **5.4 MeV peak**: its intensity is higher in CUORICINO where, in addition, it is seen to decrease with time (the CUORICINO spectrum regard a period of about 6 months). A global reduction by a factor of about 4.0±0.6 is found. The observed reduction in the region above the Po peak and the disappearance of the structures that were present in CUORICINO are again indications of a reduction of the crystal surface contamination (also in this region we have a reduction by factor 4).

Finally in order to evaluate possible contributions to the 3-4 MeV energy region due to the sources responsible of the 5.3 MeV peak the integral in the 3-4 MeV region has been plotted versus the intensity of the 5.3 MeV peak both for hall C detectors and for CUORICINO. As it is clear from Fig 8.9 no correlation seems to exist between the two energy regions. The same analysis done for the ^{238}U peaks (surface contaminations of the crystals) both for CUORICINO and hall C detectors yielded identical results validating the hypothesis that a minor contribution came in the DBD region from the surface contamination of the crystals.

8.4.2 Conclusions

The comparison with CUORICINO shows a reduction of the surface contamination of the crystals by a factor of ~ 4. This result is very important since this reduction is one of the CUORE

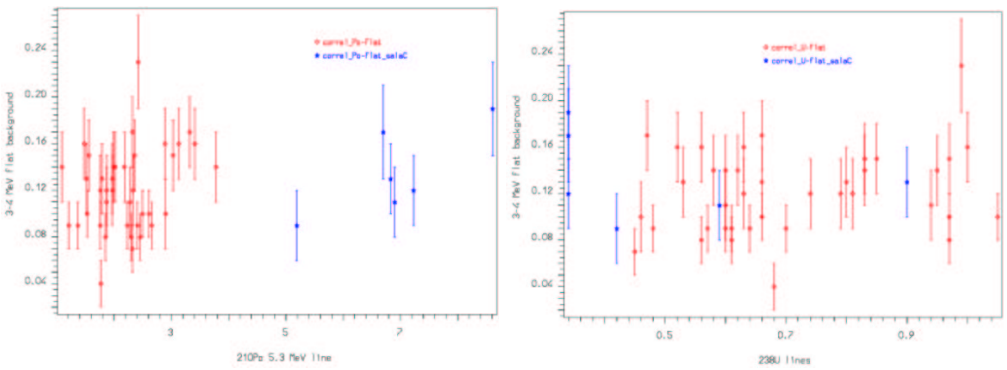

Figure 8.9: Integral in the 3-4 MeV region plotted versus the intensity of the 5.3 MeV Po peak and of the ^{238}U peaks for CUORICINO and Rad1.

milestones.

Moreover a bulk contamination of the crystals in long living Th isotopes from both chains is observed. This contamination was not easy to be identified and up to now the 4 MeV line was always interpreted as an indication of Th surface contamination of the crystals.

The higher intensity of the 5.3 MeV peak in hall C with respect to CUORICINO is an indication of a higher contamination in ^{210}Pb (it could also be a Po contamination but we should have had a longer measuring time to see if the rate is decreasing in time). Part of the contamination is on the crystal surface. In fact a fraction of the 5.3 MeV events had low energy coincidences in facing crystals. In order to reproduce the Po peak, with a low energy tail, a surface contamination of an inert material facing the crystals is needed. The continuum background in the region between 3 and 4 MeV does not seem to be changed with respect to CUORICINO. This is a further proof of the fact that the crystal surface contaminations do not give high contributions to the continuum in this region (confirming the estimate of 20 $\pm$ 10 %). Candidate sources for this background are the surface contaminations in U and Th (with all the possible chain breaks) of the inert materials facing the crystals.

The worst results obtained in this run regards the, so called, copper contaminations. In fact the integral in the 3-4 MeV region is compatible with the CUORICINO background. This is a strange result if the origin of the background is really the copper surface contaminations. The copper was treated with materials as clean as the ones used for crystals (in some cases exactly the same materials). It is difficult thus to explain why this cleaning procedure should have worked for the crystals and not for the copper. Moreover it is a strange coincidence that completely different treatments (CUORICINO and Rad1) give the same results.

These results opened the way to hypothesis about the origins of the background different from that coming from copper surfaces.

8.5 The Rad2 setup

Starting from the results of the Rad1 test, a second measurement was performed to search for possible sources of background different from the copper inside the detector.

The idea of the measurement was to exclude all the other small parts of the detector as

possible background sources. Apart copper the other materials faced to the absorber are the thermistors, heaters, gold wires (that connect the chips with the output copper pins) and the PTFE supports (see Fig. 3.4). All these materials were tested in the last 15 years with HPGE and selected for their very low bulk contamination.

The thermistors can be rejected as a background source, since radioactive contaminations coming from the surface must release at least part of their energy inside the thermistor. This energy release will generate a very fast pulse signal on the thermistor. The heat is released directly on the thermistor without the mediation of the glue spots' conductance. This will lead to shorter rise time (almost negligible). On the other hand the heat is dissipated immediately via the gold wires without passing trough the PTFE supports. This should lead to shorter decay times. Since the background events in the 0νDBD region are identical with all the events elsewhere the hypothesis of thermistor events was rejected.

To reject the other components a test was prepared in the following way. The idea is to face a square (5 cm^2) of material to be tested to a crystal of known background. To do this the Rad1 tower was used. After the experimental test this tower was disconnected from the cryostat and stored, without dismounting anything, under nitrogen atmosphere. For Rad2, 6 dedicated squares of different materials were fixed to the top and bottom frames. In Fig. 8.10 the tower of the Rad2 test and the samples are visible. PTFE pieces were faced to 4 detectors while the heaters and wires to 2 crystals each, respectively.

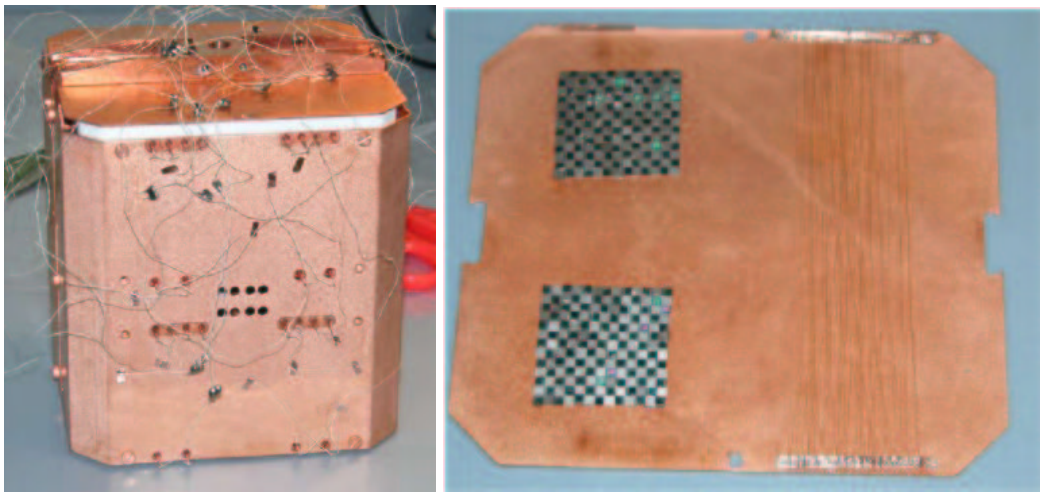

Figure 8.10: The Rad2 tower (left); the PTFE sample is visible on the top, faced to the crystals. On the right the samples of gold wires and heaters are visible; the chess effect of the heater is due to the fact that they are arranged both front and back.

In Tab. 8.6 the amount of material of each sample is compared with the amount of the same material present inside the CUORICINO tower.

8.5.1 Analysis and Result

The results of the Rad2 measurement were very clear. In fact the contribution of these samples to the CUORICINO background was completely excluded.

		Volume (mm^3)	Surface (cm^2)
PTFE	CUORICINO	1544	5
	Rad2	7890	30.25
	Ratio (R/C)	5.11	6.05
		length (cm)	
Wires	CUORICINO	8	
	Rad2	638	
	Ratio (R/C)	79.75	
		number	
Heaters	CUORICINO	1	
	Rad2	169	
	Ratio (R/C)	169	

Table 8.6: Comparison of the amount of material per detector between the Rad2 setup and CUORICINO. Note that while in CUORICINO each detector is exposed to all the samples in Rad2 each detector sees only one sample.

The tower was cooled down in April 2005. During the cooling process the electrical contact of one of the 4 detectors faced to PTFE was lost. The total collected statistics was about 540 hours. This means 1080.02 h·detector for heaters and the wires (2 detectors each) and 1620 h·detector for PTFE (3 detectors).

In Tab. the results are reported with the comparison between Rad2, CUORICINO and Rad1. The results showed that the contributions of the heaters and wires are completely negligible. The PTFE contribution is still compatible with being at maximum the source of 15% of the CUORICINO background (see Tab. 8.7). In Tab. the new limits for bulk and surface contaminations for these samples are reported.

8.6 Conclusions and Prospects

The results of Rad2 maintain open the problem of background reduction. We considered two different strategies for the future tests and R&D activities.

The first was based on the believe that the sources of the contaminations are really degraded alpha particles. This means that the main background source is the copper and that during the cleaning procedure a failure must had happened. The definitive test we suggested to understand this problem is to cover all the surface of copper facing the crystals with a special radio-clean plastic layer to stop alpha particles eventually escaping from copper. The main advantage of this plastic foil is that, since is very thin, the bulk contamination and the surface contamination are the same. This allows a measurement with HPGE which is in the same time a measurement of bulk and surface contamination. Once selected a clean foil (that came out to be a commercial plastic foil for alimentary applications) all the copper holder will be covered and then measured (the so called Rad3 test). In Fig. 8.12 (left) the detector during the assembling phase is presented. The plastic foil is clearly visible on the internal surface of the copper covers and on the frames.

mass = 0.79	Time [h]	2700-3200	Err.	3200-3400	Err.	3400-4000	Err.
PTFE	1620	0.28	0.07	0.46	0.13	0.21	0.05
Ratio (Rad1)		1.46	0.39	0.94	0.30	1.63	0.47
Heaters	1080	0.12	0.05	0.35	0.14	0.12	0.05
Ratio (Rad1)		0.61	0.28	0.71	0.30	0.92	0.40
Wires	1080	0.14	0.06	0.75	0.21	0.14	0.05
Ratio (Rad1)		0.73	0.31	1.53	0.47	1.07	0.44
Rad1		0.19	0.03	0.49	0.06	0.126	0.019

4000-4350	Err.	4350-4600	Err.	4600-4950	Err.	4950-5200	Err.
0.35	0.09	0.25	0.09	0.24	0.07	0.46	0.12
1.32	0.37	1.44	0.58	0.73	0.24	1.68	0.51
0.10	0.06	0.23	0.10	0.23	0.09	0.19	0.09
0.37	0.22	1.36	0.66	0.70	0.28	0.67	0.35
0.27	0.09	0.09	0.07	0.33	0.11	0.56	0.16
0.99	0.37	0.54	0.40	0.99	0.34	2.02	0.66
0.27	0.04	0.17	0.03	0.33	0.04	0.28	0.04

5200-5350	Err.	5350-5450	Err.	5450-6500	Err.	6500-10000	Err.
4.70	0.53	2.32	0.39	0.13	0.03	0.03	0.01
0.54	0.06	0.75	0.14	0.94	0.25	1.53	0.47
5.62	0.71	2.32	0.47	0.21	0.05	0.03	0.01
0.65	0.08	0.75	0.16	1.58	0.40	1.31	0.51
9.19	0.91	3.38	0.57	0.08	0.03	0.02	0.01
1.06	0.11	1.09	0.20	0.58	0.23	0.82	0.39
8.7	0.3	3.1	0.2	0.13	0.01	0.020	0.003

Table 8.7: Background measured in Rad2 (in counts/keV/kg/y) per energy interval (in keV) compared with the Rad1 results in the same energy intervals.

PTFE			^{232}Th	^{238}U
bulk		g/g	$6.30{\cdot}10^{-10}$	$3.80{\cdot}10^{-10}$
surface	$\lambda = 1\mu$m	Bq/cm^2	$3.20{\cdot}10^{-8}$	$1.30{\cdot}10^{-7}$
surface	$\lambda = 5\mu$m	Bq/cm^2	$5.90{\cdot}10^{-8}$	$1.40{\cdot}10^{-7}$
Si heaters			^{232}Th	^{238}U
bulk		g/g	$2.80{\cdot}10^{-8}$	$1.30{\cdot}10^{-8}$
surface	$\lambda = 1\mu$m	Bq/cm^2	$1.60{\cdot}10^{-6}$	$8.20{\cdot}10^{-7}$
surface	$\lambda = 5\mu$m	Bq/cm^2	$3.30{\cdot}10^{-6}$	$7.50{\cdot}10^{-7}$
Gold wires			^{232}Th	^{238}U
	bulk	g/g	$3.10{\cdot}10^{-7}$	$1.20{\cdot}10^{-6}$

Table 8.8: Contamination values measured for the different materials.

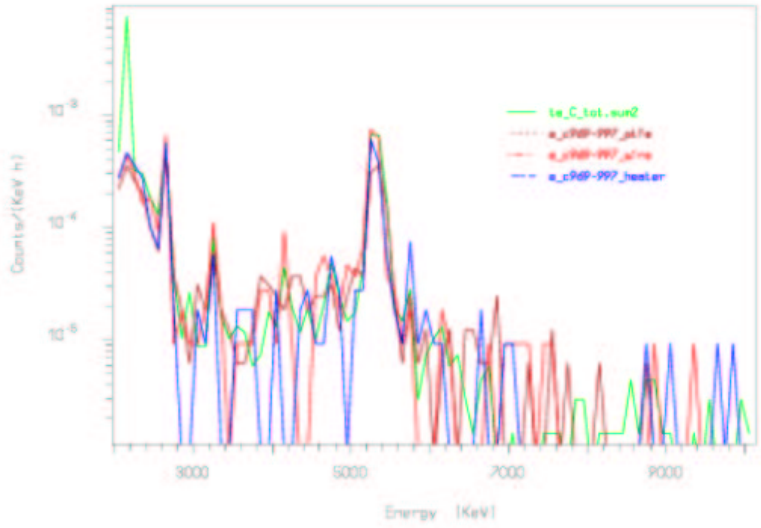

Figure 8.11: Final spectra from the Rad2 measurement. In purple PTFE, in red the heaters and in green the wires.

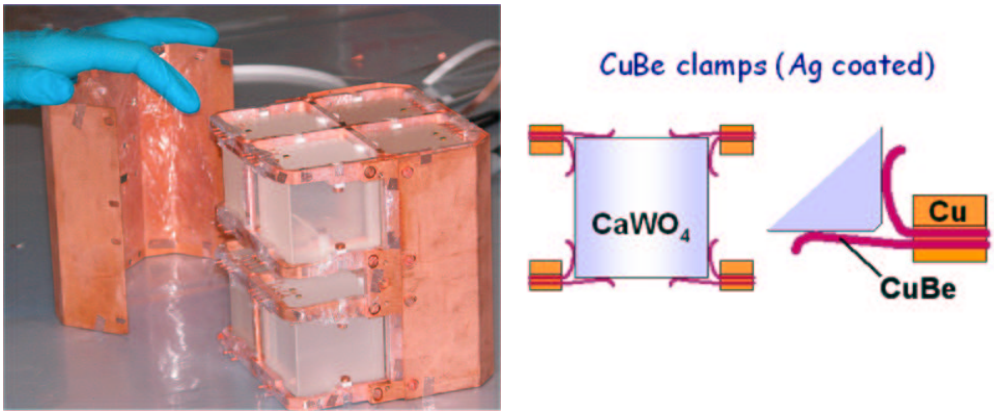

Figure 8.12: Assembling of the Rad3 tower with transparent plastic foil covering the copper (left). The CRESST experiment solution to substitute PTFE with copper-beryllium clamps (right).

A second solution is, on the other hand, based on the hypothesis that the copper was correctly cleaned and that the source of background are not degraded alpha particles but more exotic effects. One suggestion is that these background pulses can be originated from thermal release coming from the PTFE supports. This phenomenon can arise from mechanical adjustments of the PTFE (already observed in other bolometric detectors at lower energy [159]. Another possibility is that these energy releases are originated from radioactive decays inside the PTFE very near their surface. To exclude this "exotic" possibility a new test has been projected (Rad4) using copper-beryllium supports instead of the usual PTFE, as already suggested by the CRESST

collaboration for their detectors (see Fig. 8.12 right).

8.6.1 A possible contribution: the Liquid Bolometer approach

Finally I want to present a possible personal contribution to the study of background contaminations that I started to develop during the last months of this PhD work. This is just a preliminary R&D activity but the prospects can be quite interesting.

The idea is very simple and consists in using as the absorber a compound that is liquid at room temperature. A small "glass" is filled with the solution and a heater and a thermistor are suspended inside the solution. While cooling down the solution freezes trapping the thermistor and the heater inside. At low temperature this detector should work as a bolometer. The absorber will be an amorphous material and not a mono-crystal and this will, for sure, worsen the behavior of the detector due to dispersion on impurity sites and crystallin lattice irregularity. Nevertheless, several amorphous materials have been tested obtaining promising results (i.e. lead).

The important feature of this technique is the possibility of testing many different compounds or solutions that do not have available crystallin structures. The application that was at the origin of this development was the test of measuring the surface contaminations in copper. By etching a copper frame we remove the surface contaminations that in the end form a compound with the acid ($CuNO_3$). Measuring this solution (with the contaminations inside the absorber but not on the surface) will allow us to get a precise test of the contaminations by observing the corresponding lines in the spectrum.

Up to now two tests had been performed. The first one, with a PTFE glass and 2 g of $CuNO_3$, failed (no evidence of pulses was seen in the thermistor circuit). The second measurement (still going on) is performed with a tin glass and the same solution. In this measurement some evidence of pulses was observed but at the moment a complete spectrum is not yet available to understand the performance of the detector.

If the results will be confirmed a wide choice of applications will be possible using this technique.

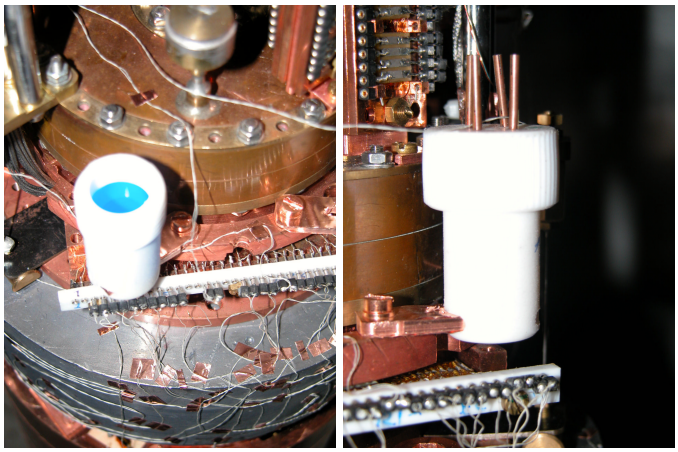

Figure 8.13: First prototype of the Liquid Bolometer: the PTFE glass with $CuNH_3$.

Chapter 9

Improving detector behavior: the new design

As widely reported in the previous Chapters, CUORICINO demonstrated the feasibility of a large mass experiment such as CUORE. The CUORE detector setup consists of an array of 19 towers with a structure identical to the CUORICINO one. Nevertheless big developments can be achieved by only slightly changing the detector setup.

In this chapter I will present the development, project and test of a new design for the CUORE detector. In the first part of the chapter the motivations and guidelines that I have followed are reported. The possible contribution to CUORE sensitivity and behavior are highlighted.

In the second part the experimental test and results are presented.

9.1 Motivations

The first indication of the possibility of obtaining good improvements on the detector's behavior with small changes in the experimental setup came from CUORICINO. The final design of the PTFE supports of the TeO_2 crystal, presented in section 3.4.2, was introduced just before the assembly of CUORICINO after a systematic study of the thermal contractions of the different components of the detector (copper, TeO_2 , PTFE, etc...). This new design produced important improvements. The most important of them was the suppression of the, so called, "very noisy detectors". These detector behavior, observed for the first time in MiDBD, showed after a few thermal cycles (cooling down and warming up of the tower) big baseline fluctuations (i.e. vibrational power dissipation), often higher than the particle signals. Obviously these detectors were useless for the measurement. This phenomenon was associated with the thermal contraction of the PTFE supports that left the crystal free to vibrate. In CUORICINO this behavior almost disappeared.

In the case of CUORE, the setup modifications can be summarized in two different task: the improvement of sensitivity and the improvement of detector behavior.

9.1.1 Improving sensitivity

As mentioned in Chapter 8 the reduction of the copper surface contamination is considered a primary task in the Contamination Reduction Program part of the CUORE project. One straightforward method of reduction can be the reduction of the amount of copper facing the detectors. This reduction will lead to: the increase of the visibility between active surfaces and the reduction of the copper surface and consequently the reduction of the amount of contaminant coming from copper surface, respectively.

Improving visibility

One of the significant gain passing from CUORICINO to CUORE is the granularity of the detector. In CUORE most of the detectors are surrounded in any direction by other detectors. This characteristic offers a natural tool to reject radiation passing trough different detectors, like high-energy muons or multi-interacting gamma rays. Granularity is at the same time an important tool to reject surface alpha contaminations by observing a signal in coincidence on two facing detectors. This technique has been already successfully tested in CUORICINO, even though the geometrical coverage of the solid angle seen by each detector is not so favorable. In CUORE the most important limitation in degraded alpha particles rejection will be due to the copper structure of the holder that partially shields one detector from the others. Reducing the dimensions of this copper structure will proportionally improve the efficiency of a multi-alpha events rejection.

Reducing Contamination

Since the copper surface is presently believed to be the most important source of background (see Chapter 8), a reduction of this surface implies a reduction of the background.

9.1.2 Improving Detector Behavior

The improvement of the detector behavior can be split in two branches: the necessity of having more uniform resolutions on different detectors and the challenge to improve the reproducibility of the response on different detectors (time evolution of the pulse, pulse hight, etc.), respectively.

Resolution

The presence of different resolutions on different detectors generates problems in analyzing summed spectra, especially in fitting summed peaks. Due to the statistical effects, the shape of a radioactive peak (alpha or gamma) is gaussian and the FWHM of the peak is the resolution of the detector. When one sums the spectra of different detectors, the shapes of the summed radioactivity peaks are not anymore gaussian but they are a sum of gaussian distributions with different FWHM corresponding to the resolution of each of the summed detectors. In the CUORICINO experiment the distribution of resolutions on the different detectors even if small is not negligible (see Fig. 4.2). The average value on the $5\times5\times5$ cm^3 detectors is 7.5 ± 2.8 keV . This means that the resolution on different detectors can differ by $\sim \pm 30\%$. Summing a small number of channels this problem can be fixed by using a "summed gaussians" fitting function. Increasing the number of channels both the summing operation and the fitting

are becoming more difficult and can generate broadening of the peak and thus worsening the resolution.

Detector Response

The irreproducibility of the response of the different detectors is a well known problem in macrobolometers, observed both in MiDBD and CUORICINO. A more reproducible response from different detectors will allow the use of automatic analysis tools to deal with a big number of channels.

The observed reduction of thermophononic noise in CUORICINO, thanks to the introduction of PTFE supports, showed that the detector's structure can contribute to the energy resolution.

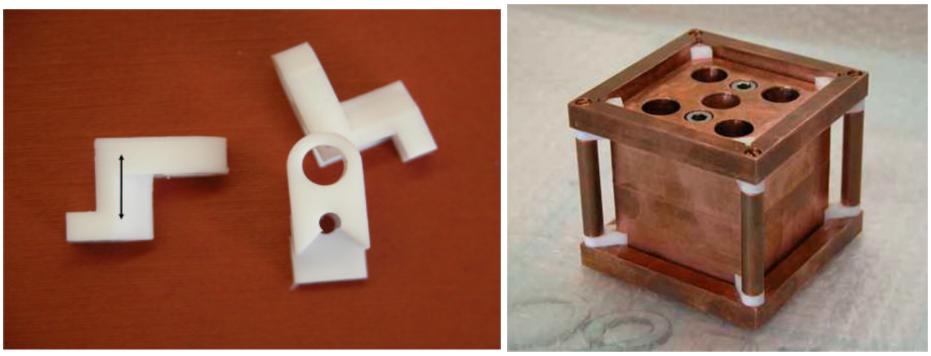

Figure 9.1: The new design of the PTFE supports to be fixed to the copper columns (left). First prototype of the new holder (right) with a dummy crystal, made of copper, to test mechanical properties. The holes in the dummy were made to reach the same weight as a TeO_2 crystal.

9.2 A New Design For the Single Module

I started to project the new crystal holder in 2003 after the start up of the second CUORICINO run. The starting point was the observation that the new PTFE supports introduced in CUORICINO reduced significantly the sensitivity to noise of the detectors but did not improve at all the reproducibility of the detector behavior (pulse evolution in time). This irreproducibility usually affects the thermal conductance and capacitance. These affect the thermal structure of the detector as presented in sec. 2.2. As an example the irreproducibility of the thermal conductance between the copper and the crystal, i.e. mainly the thermal interfaces between copper and PTFE and between PTFE and the crystal is always present. As can be seen from the picture 3.4 the PTFE supports in CUORICINO are often deformed due to their thickness and to the spread in dimensions of the TeO_2 crystals. In CUORICINO the dimensions of the $5\times5\times5$ cm^3 crystals can differ from the average with almost 1 mm (maintaining the cubic shape). This deformation produces big variation in the conductance between PTFE and crystal. In fact the conductance at low temperature is proportional to the contact area and to the pressure applied on that area (Kapitza conductance [119]). It is obvious that PTFE deformations can change the PTFE-crystal

contact area from one detector to another. To solve this problem I designed new pieces much stronger for which the deformation should be much less (see Fig. 9.1).

9.2.1 Reducing the Amount of Copper

At the same time, since the big effort deposed for background reduction as described in Chapter 8 was in the run, I designed the new holder trying to contribute also to this effort. The first improvement I introduced was the elimination of the copper screws. This components that are present in big quantities in CUORICINO (16 screws for each four-detectors module) need a complicated and dedicated machining. Moreover, the design of the screw is intrinsically complex with many corners and thus the clean procedure of the screws is not so easy and can fail. To prevent this the first step was to eliminate all the screws faced to the detector, fixing the PTFE supports directly on the copper columns of the holder. In Fig. 9.1 a picture of the first prototype I prepared is shown: a dummy crystal made of copper was prepared, of the same weight like the usual TeO_2 crystals.

9.2.2 An Easy Assembly

The final input for the new design came from the experience in assembling CUORICINO. This activity, that was performed in the second half of 2002 took more than 5 months to build and assemble the entire detector. For the 19 towers of CUORE this time per tower must be strongly reduced.

To simplify the assembly procedure one important task is that the dimensions of all the different pieces must be fixed and controlled. This is not an easy goal, due to the fact that both the copper and PTFE are soft materials. Specially PTFE suffers deformation both during the machining and during the assembly and its dimension are very difficult to control with a precision better than 1-2 tens of mm. Big improvements have been achieved in the past years in dimension control and for CUORE further gains will be obtained. The final production of the copper will be done via electroerosion with a precision on the dimensions of 0.5 tens of mm, while the PTFE will be produced with special blank modules that guarantee the same precision avoiding any mechanical machining.

9.3 First Test: the $6 \times 6 \times 6$ cm^3 Detectors

Since I was directly involved in the test of the large mass bolometers described in Chapter 7, the collaboration decided to test the new holder design for these detectors. The goal of this measurement was to test the resolution and sensitivity to noise of the detector and the reproducibility of the signal obtained with two detectors. This was not a radioactivity test and no particular care was devoted to background suppression. Thus no information could be gained about the contribution of screws suppression. The details of the apparatus and of the experimental setup are reported in sec. 7.2.

As mentioned in sec. 7.3 the results were encouraging from the point of view of the detector resolution (sensitivity to noise and baseline stability). The resolution on the two detectors for the ^{208}Tl gamma line was 3.6 and 4.2 keV, respectively (CUORICINO average 7.5 keV). Of course the number of detectors tested is not statistically significant, but it is an encouraging indication. Nevertheless a few problems related to the new holder came out, that needed a solution.

The biggest one was the breaking of some of the corners of the two crystals during the first cool down. This was probably due to the fact that the new PTFE supports deformed much less than the previous ones and tensioned very strong on the crystals. Unfortunately this was the first time that we used $6 \times 6 \times 6$ cm^3 and thus we do not know if the problem can be partially addressed to some intrinsic fragility of the big crystals. In the second cool down the problem was partially fixed by changing the orientation of the crystals. In fact the TeO_2 crystals were always mounted inside the holder with the top face perpendicular to the <001> axis. In this way, the force applied by the PTFE supports, when they undergo thermal contractions, is parallel to the <001> axis. The force is thus parallel to the breaking crystalline planes and the possibility of cracking the crystal increases. After the second cool down no further cracks were observed. This behavior is encouraging even though not definitive because the crystals were already broken.

Another negative answer came from the irreproducibility in the pulse shape and time evolution of the signals. The most interesting result, even if negative, was the big difference in the behavior of the two thermistors on the same crystals (see Tab. 7.1). Each couple of thermistors saw the same set of thermal capacitances and conductances apart their own connections with the crystal (glue) and with the heat sink (gold wires). This was an indication that the major uncertainties in the detector behavior are related to the thermal system of the thermistor. This indication is confirmed by the observation (statistically more significant) made in CUORICINO that the resistance at base temperature of different thermistors can be quite different (up to an order of magnitude), even if the intrinsic characteristics of the thermistors (ρ_0 and T_0) where measured to be very reproducible. This was usually addressed to the irreproducibility of the couplings crystal-thermistors (via glue spots) and thermistor-heat sink (via gold wires). Moreover the possibility that mechanical stress can change the behavior of the NTDs is also considered.

After collecting all the possible information from the results of this test I started the second phase of the project designing the four-detector module.

9.4 Four-Detector Module Design

The four detector module was designed following the additional goal, described in sec. 8.1, of reducing the copper amount and improving the visibility of different detectors.

The first problem was to scale the structure of the single module to a four-detector module. There are in fact just 4 columns for each module and I did not want to reintroduce screws. This problem was solved by introducing copper teeth on which the PTFE supports are fixed (see Fig. 9.2). An important additional task of this design is that the four crystal of a module must have the same vertical width. In fact the PTFE pieces are designed, as in CUORICINO, in a way that to support more than one crystal but they deformed much less than in the CUORICINO case and so they do not adapt to the different dimensions of the crystals.

This last request on the dimensions of the crystal materialize in a much more easier way of assembling. In the new design there is no need to compensate the different dimension of the 4 crystals tuning the screws and the position of PTFE.

The second important development of the holder is the reduction of the amount of copper present in the holder. This work was done in two steps: first reducing the copper of the four detectors module, and second reducing the big amount of copper used to connect together the different modules. The first contribution was to remove one of the arms of the cross of the base

and top frame of each module.

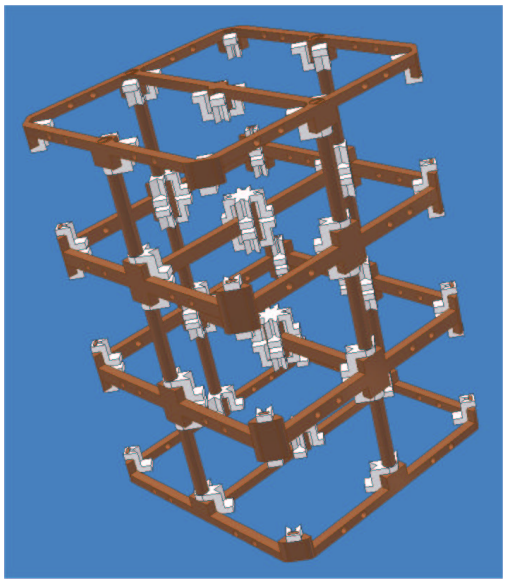

Figure 9.2: The new design 4 detector module design.

9.4.1 From a Module to a Supermodule

The biggest change in the final design is the elimination of the lateral copper bars that held the four detectors modules in the tower. To do this I decided to connect the different modules via the copper columns. Each column has a threaded hole on the top and ends with a screw. In this way the columns of one module are screwed directly on the columns of the module immediately below. This allows a second important improvement that is the removal of the top frame of each module. In the new design the top frame of one module coincides with the bottom frame of the module above.

Following these ideas I designed for CUORE a new "supermodule", that is the entire tower (see Fig. 9.3). Thanks to the new compact design there is not anymore a separation between the different 4–detector modules inside the tower because they are all connected together. The supermodule must be assembled in sequence starting from the bottom to the top.

9.4.2 A Contribution to Background Reduction

The possible contribution to background reduction, in the case the main radioactive source is the copper surfaces, comes from the reduction of the amount of this surface. In Tab. 9.1 the calculated surface for CUORICINO and for the new holder are compared. The advantage of this reduction technique is that the background is now independent from the level of the contaminations and from the cleaning procedure. In any case the new design provides a reduction of a factor of about 2 of the copper surface and thus on the amount of contaminants. Nevertheless in CUORE the contribution of the covers (in Tab. 9.1 normalized per detector) is not uniform

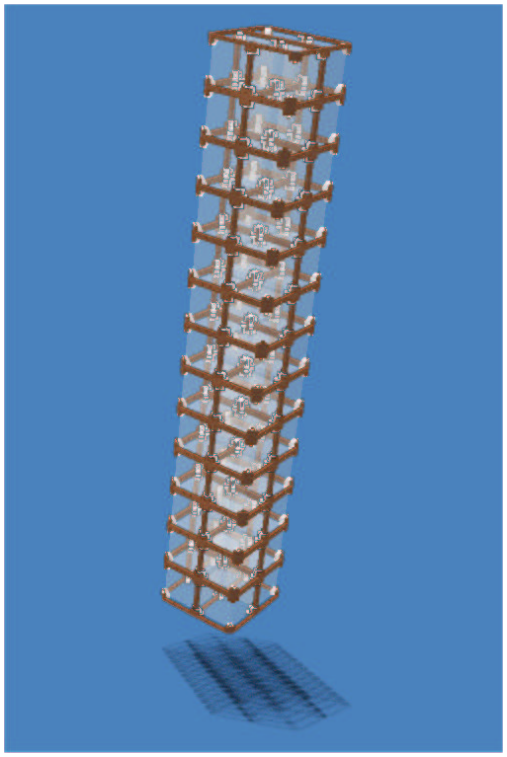

Figure 9.3: The supermodule tower as it will be in the CUORE setup.

because of the arrangement of the detectors; in the external ones it is much higher and in the internal it is almost zero.

Note that the contribution of the suppression of the copper external covers is not related to the new design but it is an intrinsic task of the CUORE design.

9.5 Second Test: The CAW Tower

The second test will be a dedicated measurement projected to test the mechanical behavior of the structure. The test is intended to show that the new holder has at least the same characteristics as in CUORICINO with respect to resolution and baseline stability. If this will be confirmed then the new holder can be adopted as the official CUORE holder and further developments on different topics can be done using this new structure. This test took the name *CAW tower* (from CUORE Assembling Working group, the R&D group that in charge of this development).

To make a reliable measurement it is necessary to reproduce at least the situation of the detectors inside CUORE. To do this I prepared a setup of 3 four-detector floors, since the top and bottom ones do not reproduce the situation of most of the floors in CUORE. In fact being the tower a 13 floors modules, 11 floors will be internal, i.e. between two other floors, while just 2 are in the top and bottom configuration, respectively.

	Frame surface (int)	Column surface	Frame surface (upper)	Other frame surface	Screws	Total	Covers	Total + Covers
CUORICINO	40	12	44	48	4	148	68	216
CUORE	34	12	34	–	–	80	17	97
Ratio	1.17	1	1.29	–	–	1.85	4	2.23
Reduction	14.6%	0%	22.4%	100%	100%	45.9%	75%	55.1%

Table 9.1: Average copper surface that one detector can see in CUORICINO and in the new CUORE design, calculated using a rough geometrical model of the frames.

9.5.1 Modification of the PTFE supports

In April 2005 a test was performed in the Seismic and Dynamic Laboratory of the Casaccia Center of Ente Nazionale per l'Energia Atomica (ENEA). This test intended to be a part of an ongoing program to study the sensitivity of the detector to vibrations and to develop the anti-vibration damping system. The test was performed on a vibrating platform. A prototype of one floor of the tower with 4 TeO_2 crystal was fixed on the platform inside a special dewar with an interspace filled with liquid nitrogen and a vacuum chamber for the prototype.

During this test some of the measurements were dedicated to study the breaking point of the crystal as a function of the force applied by the PTFE supports at room temperature. For the test new PTFE pieces were prepared with reduced vertical dimension. In fact detailed calculations showed that vertical dimensions of 4 mm instead of 8 mm (used in the first test) are enough to apply a force just below the breaking point of the crystal.

The 4 thermal cycles at 77 K (liquid nitrogen temperature) showed that the the best condition for not to break the crystals is to have, at room temperature, the distance between upper and lower PTFE supports exactly equal to the crystal dimension (no force applied).

This modification, together with the change of orientation of the crystals, seemed to completely fix the problem of breaking crystals.

9.5.2 Experimental Setup

The experimental setup was prepared with a 12 crystals arranged in 3 floors of 4 detectors each. To reproduce at best the CUORE configuration I decided not to add copper covers screwed directly on the crystals holder. These covers can increase the rigidity of the structure and change the behavior of the detectors in terms, for example, of the sensitivity to noise. For this reason I designed a copper vessel that is separated from the mini-tower and is connected only to the top frame (see Fig. 9.5). The wires of the DAQ chain run on copper bars, also not mechanically connected to the tower.

The 12 crystals used as absorbers in this test came from 3 different sets each of 4 crystals. Eight crystals (with codes from B63 to B70) were just arrived at that time from the SICCAS company, 4 of which lapped with a rough SiO_2 powder and 4 just cut after production with no additional treatment. The dimensions of these crystals are uniformo within 1 tenth of mm. The other 4 crystals came from the CUORICINO spear detectors. Unfortunately these crystals were in fact discarded from the CUORICINO set due to their dimensions. This set was thus quite not

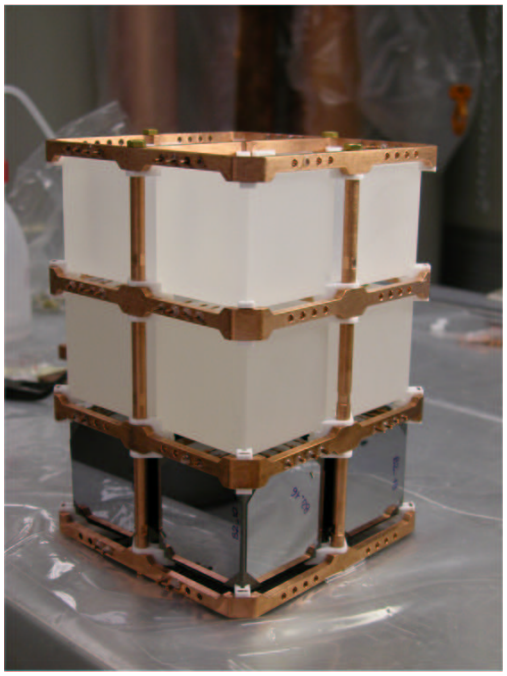

Figure 9.4: The CAW Tower during the assembling. In the lower floor the SSB detector are visible.

uniform in dimension.

Inside the tower an independent test was done. On the lower floor of the tower, the four detectors (see Fig.9.4) were prepared to be a test of Surface Sensitive Bolometers (SSB). These detectors [160] consist in normal bolometers on the surface of which 6 thin slabs are glued. Each of these slabs is a bolometer itself and is used to tag the alpha particles coming from outside the detector. This project is developed as a possible alternative solution to suppress the external background source. These slabs (in this case Si slices) do not affect the behavior of the detectors when used as simple bolometers. For this test 4 old crystals were used,those with big differences in dimensions.

The tower was successfully cooled down and operated between June and September 2005.

9.6 Results

The CAW tower constituted the second biggest TeO_2 mass ever built and operated (equal to a fourth of CUORICINO). The assembly of the detectors was very fast in what regards the mechanical connections. The positioning and fixing of the crystals in the holder was very easy and did not required any particular assembling skill. Unfortunately there were still big problems when gluing the chips (thermistor and heater) on the detector. There were also several irreproducibility and failures in making the electrical connection of the gold wires.

During the cooling down process a thermistor and three heaters were lost due to the breaking of electrical connection at low temperatures. The main measurement consisted in a calibration

Channel	Crystal	FWHM	comments
1	*B3	-	no heater - bad
2	*B33	7.1	
3	B64	5.9	no heater
4	B65	4.8	
5	B67	4.1	
6	B70	6.2	
13	*B21	6.8	tail on the left
15	B63	5.7	no heater
16	B66	6.0	tail on the left
17	B68	4.2	
18	B69	5.7	
Average		5.7±1.0	
Average	no SSB	5.5±0.9	

Table 9.2: Resolution at the 2615 keV ^{208}Tl gamma line.

with the usual CUORICINO ^{232}Th sources, to obtain the resolution at the 2615 keV line (resolution in the 0νDBD region).

The results, reported in Tab. 9.2 show an average resolution of 5.7±1.0 keV comparable with the CUORICINO resolution 7.5±2.8 keV (see sec. 4.2). The very important result is not the average resolution, that is by the way slightly better than CUORICINO one, but the deviation from the average that is significantly better. The average resolution excluding the SSB detectors, that were of different dimensions, 5.5±0.9 keV did not show significant improvements.

Almost no damage on the crystals with new teflon supports was observed. Only on crystal B64 a broken piece of about 0.5 mm^3 was found.

9.6.1 Prospects

The results obtained with the CAW tower were very encouraging, even though not definitive due to the small number of crystals. Nevertheless the test demonstrated that the new design can work being as good as the old CUORICINO providing at the same time improvements on the resolution and on the easiness of the assembly. The CUORE collaboration gave a first positive evaluation and is considering the possibility of accepting the new design as the official CUORE design.

On the other hand there are still open questions and problems that need to be solved. Two important topics will be involved in the next developments: the detector behavior and a new design for the electrical connections.

Detector Behavior

As already pointed out, one of the major failures of the CAW Tower test was the fact that no appreciable improvements appear in the time evolution of the pulses. Nevertheless, important developments are still possible on the standardization of the other thermal conductances that

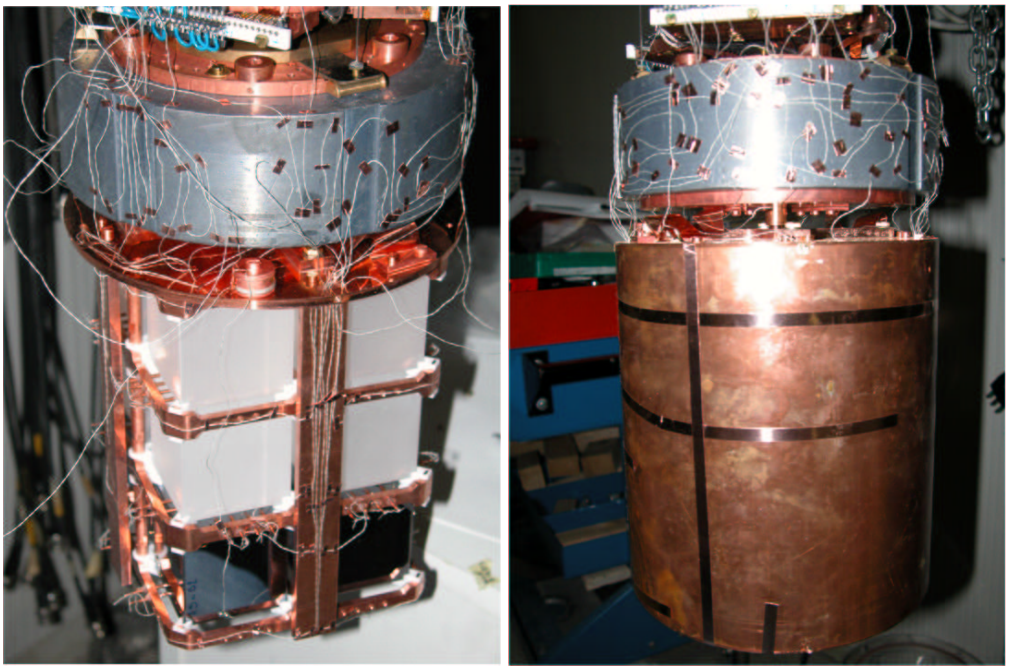

Figure 9.5: The CAW Tower during the assembling on the cryostat (left) and with the external covers (right).

connect different parts of the detector. Major gain is expected from the thermistor–crystal connection (glue) and from the thermistor–heat sink connection (gold wires and copper pins).

Electrical Connections

From the point of view of the design the main developments needed are related to the DAQ acquisition chain. The first problem concerns radioactivity. In fact while in CUORICINO all the wires are outside the copper shields and thus their surface contaminations are suppressed, in CUORE since the towers are faced one to the other the wires cannot be shielded by the copper covers. Several solution have been proposed (mainly based on the idea of having small copper or PTFE tubes shielding the wires) and must be tested.

The second problem concerns the easy assembling of the detector. The connection between the gold wires of the thermistor and the external wires in CUORICINO were performed with a very delicate procedure that must not be adopted in CUORE. The work on this topic is presently in progress.

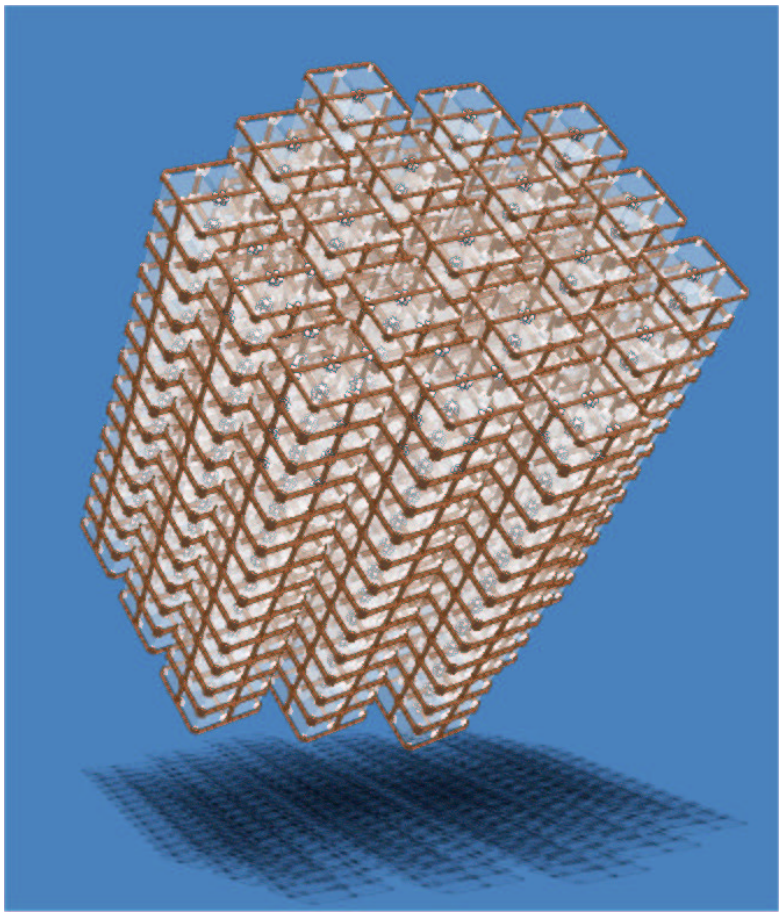

Figure 9.6: Finally the new design of the CUORE setup.

Bibliography

[1] A. Strumia and F. Vissani, hep-ph/0503246.

[2] F. A. Rodin, V. A. and F. Simkovic, (2005), nucl-th/0503063.

[3] C. Borcea *et al.*, Nucl. Phys. **A565**, 158 (1993).

[4] E. Majorana, Nuovo Cimento **14**.

[5] R. Mohapatra and G. Senjanovic, Phys. Rev. **D23**, 165 (1981).

[6] B. Kayser, in *The Physics of Massive Neutrinos*, World Scientific, Singapore, 1989.

[7] K. Fujikawa and R. Shrock, Phys. Rev. Lett. **45**, 963 (1980).

[8] J. Kaulard *et al.*, Phys. Lett. **B442**, 334 (1998).

[9] B. Pontecorvo, Zh. Eksp. Teor. Fiz. **33**, 549 (1957).

[10] Z. Maki, M. Nakagawa, and S. Sakata, Prog. Theor. Phys. **28**, 870 (1962).

[11] B. Pontecorvo, Zh. Eksp. Teor. Fiz. **53**, 1717 (1967).

[12] L.-L. Chau and W.-Y. Keung, Phys. Rev. Lett. **53**, 1802 (1984).

[13] M. Goeppert-Mayer, Physics Rev. Lett. **59**, 512 (1987).

[14] P. Siemens, in *Elements of Nuclei*, Addison-Wesley, 1987.

[15] S. Elliot *et al.*, Phys. Rev. Lett. **59**, 2020 (1987).

[16] G. Zdesenko *et al.*, Phys. Lett. **B546**, 206 (2002).

[17] H. Ejiri, Prog. Part. Nucl. Phys. **B48**, 185 (2002).

[18] W. Furry, Phys. Rev. **56**, 1184 (1939).

[19] J. Suhonen, Nucl. Phys. B (Proc. Suppl.) **143**, 240 (2005).

[20] J. Suhonen, Phys. Lett. **B607**, 87 (2005).

[21] H. Ejiri, Phys. Rep. **338**, 265 (2000).

[22] E. Caurier *et al.*, Nucl. Phys. A **654**, 973 (1999).

[23] J. Engel *et al.*, Phys. Rev. **C53**, 731 (1988).

[24] A. Staudt *et al.*, Europhys. Lett. **13**, 31 (1990).

[25] G. Pantis *et al.*, Phys. Rev. C **53**, 695 (1996).

[26] O. Civitarese and J. Suhonen, Nucl. Phys. A **729**, 867 (2003).

[27] G. Cleveland *et al.*, Astrophys. J. **496**, 505 (1998).

[28] F. N. Cattadori, C. and L. Pandola.

[29] S.-K. collaboration, hep-ex/0205075.

[30] S. collaboration, nucl-ex/0502021.

[31] K. collaboration, hep-ex/0406035.

[32] B. A. Goswami, S. and S. Choubey, Nucl. Phys. B (Proc. Suppl.) **143**, 121 (2005).

[33] A. Lewis and S. Bridle, Phys. Rev. D **66**, 103511 (2002).

[34] M. Tegmark *et al.*, Phys. Rev. D **69**, 103501 (2004).

[35] L. J. Crotty, P. and S. Pastor, Phys. Rev. D **69**, 123007 (2004).

[36] A. Staudt *et al.*, Phys. Rev. C **46**, 871 (1992).

[37] G. Pantis *et al.*, Phys. Rev. C **53**, 695 (1996).

[38] P. Vogel *et al.*, Phs. Rev. Lett. **57**, 3148 (1986).

[39] O. Civitarese *et al.*, Phys. Lett. B **194**, 11 (1987).

[40] T. Tomoda, Rep. Prog. Phys. **54**, 53 (1991).

[41] C. Barbero *et al.*, Nucl. Phys. A **650**, 485 (1999).

[42] F. Simkovic, Phys. Rev. C **60**, 055502 (1999).

[43] J. Suhonen *et al.*, Nucl. Phys. A **543**, 645 (1992).

[44] K. Muto *et al.*, Z. Phys. A **334**, 187 (1989).

[45] S. Stoica *et al.*, Phys. Rev. C **63**, 064304 (2001).

[46] A. Faessler and F. Simkovic, J. Phys. **G24**, 2139 (1998), hep-ph/9901215.

[47] J. Engel *et al.*, Phys. Lett. **B 225**, 5 (1989).

[48] M. Aunola *et al.*, Nucl. Phys. A **643**, 207 (1998).

[49] V. A. Rodin *et al.*, Phys.Rev. **C68**, 44 (2003), nucl-th/0305005.

[50] W. Haxton *et al.*, Prog. Part. Nucl. Phys. **12**, 409 (1984).

[51] E. Caurier *et al.*, Phys. Rev. Lett. **77**, 1954 (1996).

[52] J. Hirsh *et al.*, Nucl. Phys. A **589**, 445 (1995).

[53] R. H. Kirsten, T. and E. Jessberger, Phys. Rev. Lett. **50**, 474 (1983).

[54] A. Turkevich *et al.*, Phys. Rev. Lett. **67**, 3211 (1991).

[55] H. Klapdor-Kleingrothaus *et al.*, Eur. Phys. J. **12**, 147 (2001).

[56] C. Aalseth *et al.*, hep-ex/0202026.

[57] V. KBrudanin *et al.*, Phys. Lett. B **495**, 63 (2000).

[58] C. Aalseth *et al.*, Nucl. Phys. **B48**, 223 (1996).

[59] C. Aalseth *et al.*, Phys. Rev. **C49**, 2108 (1999).

[60] R. rnold *et al.*, hep-ex/0507083.

[61] F. Danevich *et al.*, Phys. Rev. **C68**, 35501 (2003).

[62] C. Arnaboldi *et al.*, Phys. Lett. **B557**, 167 (2003).

[63] C. Arnaboldi *et al.*, Phys. Rev. Lett. **95**, 142501 (2005).

[64] R. Bernabei *et al.*, Phys. Lett. **B546**, 23 (2003).

[65] A. De Silva *et al.*, Phys. Rev. **C56**, 2451 (1997).

[66] E. Fiorini and T. O. Niinikoski, Nucl. Instr. Meth. **A224**, 83 (1984).

[67] A. Alessandrello *et al.*, Nucl. Instrum. Meth. **A440**, 397 (2000).

[68] C. Arnaboldi *et al.*, accepted for pubblication on Nuclear Instr. and Meth. A (2005).

[69] R. Arnold *et al.*, Nucl. Inst. Meth. **A536**, 79 (2005).

[70] H. Klapdor-Kleingrothaus *et al.*, Modern Physics Letters **A16**, 2409 (2001).

[71] C. Aalseth *et al.*, Modern Physics Letters **A17**, 1475 (2002).

[72] H. Klapdor-Kleingrothaus *et al.*, hep-ph/0205228.

[73] H. Klapdor-Kleingrothaus *et al.*, Nucl. Instrum. Meth. **A510**, 281 (2003).

[74] H. Klapdor-Kleingrothaus *et al.*, Nucl. Instrum. Meth. **A511**, 335 (2003).

[75] H. Klapdor-Kleingrothaus *et al.*, Phys. Lett. B **570**, 54 (2004).

[76] Y. Zdesenko *et al.*, Phys. Lett. B **546**, 206 (2002).

[77] F. Feruglio *et al.*, Nucl. Phys. B **637**, 345 (2002).

[78] A. Giuliani *et al.*, Nucl. Phys. B (Proc. Suppl.) **138**, 267 (2005).

[79] G. Heusser, AIP Conference Proceedings **785**, 39 (2005).

[80] S. R. Elliott and P. Vogel, Ann. Rev. Nucl. Part. Sci. **52**, 115 (2002), hep-ph/0202264.

[81] C. Arnaboldi *et al.*, Nucl. Instrum. Methods **A518**, 775 (2004).

[82] M. Danilov *et al.*, Phys. Lett. B **480**, 12 (2000).

[83] G. collaboration, Nucl. Phys. B (Proc. Suppl.) **143**, 567 (2005).

[84] The Majorana White Paper (2003), Nucl-ex/0311013.

[85] H. Ejiri *et al.*, Phys. Rev. Lett. **85**, 2917 (2000).

[86] S. Moriyama *et al.*, Proc. of XENON01 workshop (2001).

[87] Y. Kato *et al.*, Nucl. Instrum. Methods **A498**, 430 (2003).

[88] F. N. C. Piquemal, presented at the IN2P3 scientific committee (2005).

[89] G. Bellini *et al.*, Eur. Phys. J. **c19**, 43 (2001).

[90] T. Kishimoto *et al.*, Osaka University 2001 Annual Report (2001).

[91] F. Avignone III *et al.*, New Journal of Physic **7**, 6 (2005).

[92] S. R. Elliott and J. Engel, J. Phys. **G30**, 183 (2004).

[93] H. Klapdor-Kleingrothaus *et al.*, hep-ph/0103074.

[94] S. Simon, Nature **135**, 763 (1935).

[95] D. H. Andrews *et al.*, Phys. Rev. **76**, 154 (1949).

[96] A. Alessandrello *et al.*, Physics Review Letters **513A**, 82 (1999).

[97] R. Bernabei *et al.*, Physics Letters B **424**, 185 (1998).

[98] Y. B. Levinson, Phonon propagation with frequency down-conversion, in *Nonequilibrium Phonons in Nonmettalic Crystals*, edited by W. Eisenmenger and A. Kaplyanskii, chap. 3, pp. 91–143, Elsevier Science Publisher B.V., Amsterdam, 1986.

[99] B. Taylor, H. Maris, and C. Elbrum, Phys. Rev. Lett. **49**, 416 (1969).

[100] K. Irwin *et al.*, Rev. Sci. Instr. **66**, 5322 (1995).

[101] C. Cozzini *et al.*, LTD9 conference proceedings **605**, 481 (2001).

[102] N. Mott and J. Davis, Phil.Mag. **B42**, 845 (1980).

[103] A. Miller and E. Abrahams, Phys. Rev. **120**, 761 (1961).

[104] S. Moseley, J. Mather, and D. McCammon, J. Appl. Phys. **56**, 1257 (1984).

[105] Atomic nuclear and particle physiscs and dark matter and neutrino physiscs, in *Proceedings of the 10th International Workshop on Low Temperature Detectors*, edited by F. Gatti, chap. 3–4, pp. 60–224, Elsevier Science Publisher B.V., Amsterdam, 2003.

[106] A. Alessandrello *et al.*, Nucl. Instrum. Meth. **B17**, 411 (1986).

[107] A. Alessandrello, D. V. Camin, E. Fiorini, A. Giuliani, and G. Pessina, Nucl. Instrum. Meth. **A264**, 93 (1988).

[108] A. Alessandrello *et al.*, Prepared for 3rd International Workshop on Low Temperature Detectors for Neutrinos and Dark Matter, L'Aquila, Italy, 20-23 Sep 1989.

[109] A. Alessandrello *et al.*, Prepared for 3rd International Workshop on Low Temperature Detectors for Neutrinos and Dark Matter, L'Aquila, Italy, 20-23 Sep 1989.

[110] C. Brofferio *et al.*, Nucl. Phys. Proc. Suppl. **48**, 238 (1996).

[111] A. Alessandrello *et al.*, Phys. Lett. **B433**, 156 (1998).

[112] A. Alessandrello *et al.*, Phys. Lett. **B486**, 13 (2000).

[113] C. Arnaboldi *et al.*, Phys. Lett. **B557**, 167 (2003), hep-ex/0211071.

[114] R. Firestone, John Wiley and Sons (1996).

[115] M. Barucci *et al.*, J. Low Temp. Phys. **123**, 303 (2001).

[116] A. Guiliani *et al.*, Nucl. Instrum. Meth. **A263**, 233 (1988).

[117] A. Alessandrello *et al.*, Ed. Frontieres , 447, Prepared for Low Temp. Det. for Neutr. and Dark Matt. IV 1992.

[118] A. Alessandrello *et al.*, Nucl. Instr. and Meth. in Phys. Res. **A440**, 397 (2000).

[119] F. Pobell, Matter and methods at low temperatures, 2nd edition, Springer - Verlag, Berlin, 2002.

[120] E. Gatti and P. Manfredi, Rivista Nuovo Cimento **9**, 1 (1986).

[121] W. Press *et al.*, (1991).

[122] A. Alessandrello *et al.*, Nucl. Instr. and Meth. **A412**, 454 (1998).

[123] C. Arnaboldi *et al.*, Phys.Lett. **B584**, 260 (2004).

[124] C. Arnaboldi *et al.*, IEEE Transaction on Nuclear Science **50**, 979 (2003).

[125] C. Arnaboldi *et al.*, Submitted to IEEE Transaction on Nuclear Science (2004).

[126] S. Baker and P. Cousins, Nuclear Instr. and Meth. **224**, 437 (1984).

[127] R. Barnett and others (PDG), Phys. Rev. **D54**, 1 (1996).

[128] G. Feldman and P. Cousins, Phys. Rev. **D57**, 3873 (1998).

[129] D. Groom *et al.*, Eur. Phys. J. **C15**, 1 (2000).

[130] Bernatowicz and others (PDG), Phys. Rev. **C47**, 1993 (2003).

[131] J. Suhonen, Phys.Lett. **B**, in the press (2005).

[132] H. V. Klapdor-Kleingrothaus *et al.*, Nucl.Instrum.and Meth. **A522**, 367 (2004).

[133] S. Capelli, Ph.D. Thesis (2004).

[134] R. Ardito *et al.*, hep-ex/0501010.

[135] A. Alessandrello *et al.*, Nucl. Phys. Russ. Academy of Sci. , hep-ex/0201038.

[136] A. Alessandrello *et al.*, Nucl. Phys. **B87**, 78 (2000).

[137] S. Pirro *et al.*, Nucl. Instrum. Meth. **B87**, 78 (2000).

[138] A. Alessandrello *et al.*, Nucl. Phys. **B110**, 64 (2002).

[139] G. Heusser, private communication .

[140] M. Laubenstein, private communication .

[141] J. Admatechs Co. Ltd.

[142] V. Palmieri *et al.*, Proc. of the 7^{th} workshop on RF Superconductivity B. Bonin ed. , 605 (1995).

[143] P. Trincherini, private communication .

[144] R. Silberberg and R. Tsao, Astrophys. J. Suppl. Ser. **220**, 315 (1973).

[145] S. Pirro, presented at the 11^{th} LTD conference, Japan .

[146] C. Arnaboldi *et al.*, Submitted to IEEE Transaction on Nuclear Science (2005).

[147] S. Pirro *et al.*, Nucl. Instrum. Meth. **A444**, 331 (2000).

[148] M. Pedretti, Ph.D. Thesis (2003).

[149] S. Sangiorgio, Degree Thesis (2003).

[150] A. Alessandrello *et al.*, Astrophys. J. Suppl. Ser. **B142**, 163 (1998).

[151] C. Arnaboldi *et al.*, IEEE Tran. Nuc. Sci. **44**, 416 (1997).

[152] C. Arnaboldi *et al.*, Nuclear Instr. and Meth. **A420**, 578 (2004).

[153] C. Arnaboldi *et al.*, IEEE Tran. Nuc. Sci. **49**, 2440 (2002).

[154] E. E. Haller *et al.*, Proc. Fourth Int. Conf. on Neutron Transmutation Doping of Semiconductor Materials , 21 (1984).

[155] L. Risegari *et al.*, Cryogenics **44**.

[156] S. Pirro *et al.*, in*"Sources and Detection of DARK MATTER and DARK ENERGY in the Universe"*, David B. Cline Editor, Springer-Verlag (2001).

[157] CUORE, C. Arnaboldi *et al.*, (2002), hep-ex/0212053.

[158] M. Pavan *et al.*, comunication at the CUORE collaboration meeting .

[159] J. Astrom *et al.*, physics/0504151.

[160] A. Giuliani *et al.*, comunication at the CUORE collaboration meeting .

Acknowledgments

Many people contributed to my Ph.D. activity, supporting and guiding me with precious suggestions and indications.

I must first remember Prof. Angel Morales who supported the beginning of my activity and, during the first year of my Ph.D. work, passed away. It was a great loss for science and a great personal loss.

First of all I want to thanks Dr. Oliviero Cremonesi, who patiently supervised all my work, with constant indications and corrections. His huge knowledge of physics opened my mind to many unexpected discoveries. I will never forget his kind and sweet corrections.

I thank Prof. Ettore Fiorini who started this research activity many years ago and is still the most active supporter of the hole project. I thank him for pushing me into Ph.D. and never giving up when everyone is discouraged.

All this work would not have been possible without the contribution of the two "crazy guys" of the Gran Sasso Laboratory group: Dr. Carlo Bucci and Dr. Stefano Pirro. They contributed, in quite different ways, with revolutionary ideas and illuminating suggestions to my work. I hope I learned from them how to deal with experimental problems always finding an innovative way to solutions.

Finally I must thank all the CUORE collaboration, with special mention for those that I have the luck to work with: they know how precious was their contribution to my professional growth. I must thank specially A. Giuliani, M.Pavan, F.T.Avignone, M.Pedretti, E.Previtali, C.Brofferio, G.Pessina and S.Capelli for important suggestions in different parts of this work.

I thank Dr. Francesco Vissani for illuminating my personal knowledge of the theoretical aspects of the field.

A special thank goes also to Iulian Catalin Bandac who read all this thesis correcting most of the grammar mistakes. His irreplaceable support made this work accessible to the readers.

I thank all the "young people" of the collaboration (Fabio, Samuele, Marisa, Silvia, Claudia, Francesca, Luca, Elena, Michelle, Lidia, etc...) for sharing great fun and great work.

Last but not least I must say a world for the people the really supported this activity: my wife Marta and all my family. Only Marta knows how difficult is supporting (and tolerating) me all the days of a three year Ph.D. work.

I am grateful to the friends that helped me in this Abruzzo-adventure. In a special way I thank Giovanni, Simona, Matteo, Simona, Nicola, Daniele, Alba, Maria Elena, Mirko, Paola, and all the other I met on my way.